AD_____

Award Number: W81XWH-04-1-0916

TITLE: Molecular Imaging with Quantum Dots Probing EMT and Prostate Cancer Metastasis in Live Animals

PRINCIPAL INVESTIGATOR: Leland W. K. Chung, Ph.D.

CONTRACTING ORGANIZATION: Emory University
Atlanta, GA 30322

REPORT DATE: October 2007

TYPE OF REPORT: Final

PREPARED FOR: U.S. Army Medical Research and Materiel Command
Fort Detrick, Maryland 21702-5012

DISTRIBUTION STATEMENT: Approved for Public Release;
Distribution Unlimited

The views, opinions and/or findings contained in this report are those of the author(s) and should not be construed as an official Department of the Army position, policy or decision unless so designated by other documentation.

REPORT DOCUMENTATION PAGE

Public reporting burden for this collection of information is estimated to average 1 hour per response, including the time for reviewing instructions, searching existing data sources, gathering and maintaining the data needed, and completing and reviewing this collection of information. Send comments regarding this burden estimate or any other aspect of this collection of information, including suggestions for reducing this burden to Department of Defense, Washington Headquarters Services, Directorate for Information Operations and Reports (0704-0188), 1215 Jefferson Davis Highway, Suite 1204, Arlington, VA 22202-4302. Respondents should be aware that notwithstanding any other provision of law, no person shall be subject to any penalty for failing to comply with a collection of information if it does not display a currently valid OMB control number. **PLEASE DO NOT RETURN YOUR FORM TO THE ABOVE ADDRESS.**

1. REPORT DATE	2. REPORT TYPE	3. DATES COVERED
01-10-2007	Final	1 Oct 2004 – 30 Sep 2007

4. TITLE AND SUBTITLE	5a. CONTRACT NUMBER
Molecular Imaging with Quantum Dots Probing EMT and Prostate Cancer Metastasis in Live Animals	5b. GRANT NUMBER
	W81XWH-04-1-0916
	5c. PROGRAM ELEMENT NUMBER

6. AUTHOR(S)	5d. PROJECT NUMBER
Leland W. K. Chung, Ph.D.	5e. TASK NUMBER
	5f. WORK UNIT NUMBER

7. PERFORMING ORGANIZATION NAME(S) AND ADDRESS(ES)	8. PERFORMING ORGANIZATION REPORT NUMBER
Emory University Atlanta, GA 30322	

9. SPONSORING / MONITORING AGENCY NAME(S) AND ADDRESS(ES)	10. SPONSOR/MONITOR'S ACRONYM(S)
U.S. Army Medical Research and Materiel Command Fort Detrick, Maryland 21702-5012	
	11. SPONSOR/MONITOR'S REPORT NUMBER(S)

12. DISTRIBUTION / AVAILABILITY STATEMENT
Approved for Public Release; Distribution Unlimited

13. SUPPLEMENTARY NOTES
Original contains colored plates: ALL DTIC reproductions will be in black and white.

14. ABSTRACT – **SEE ATTACHED PAGE**

15. SUBJECT TERMS
Quantum dots

16. SECURITY CLASSIFICATION OF:			18. NUMBER OF PAGES	19a. NAME OF RESPONSIBLE PERSON USAMRMC
a. REPORT	b. ABSTRACT	c. THIS PAGE		19b. TELEPHONE NUMBER *(include area code)*
U	U	U	UU	57

(17. LIMITATION OF ABSTRACT: UU)

Abstract

Despite the development of various animal and tissue culture models for the study of human prostate cancer growth and metastasis, there is no non-invasive model that provides real-time information on the behavior of prostate cancer cells in the prostate or at distant sites. The goal of this application is to devise a highly sensitive and specific nanotechnology- based molecular imaging technique to detect prostate cancer growth locally and at distant sites and observe the interaction between prostate cancer cells and their local microenvironment during their acquisition of migratory, invasive and metastatic capabilities. This technique was made possible by a close collaboration between Chung/Zhau, who have extensive experience in the development of human prostate cancer metastatic models, and Nie, a biomedical engineer who devised an ultrasensitive and specific nanotechnology quantum dot (QD) bioconjugate that can image cancer cells in live animals at a sensitivity close to the single cell level. This collaborative interaction between Chung/Zhau/Nie could significantly improve our ability to diagnose, prognose and treat human prostate cancer, first in experimental models and later in the clinic.   We have proposed three highly interactive aims that allow the PIs and trainees to interact during the development of this highly innovative technology. Aim 1 is to synthesize and test QD conjugates for the molecular imaging of prostate cancer cells in culture, and to improve the quality of the QDs so they will emit light at the near-infrared range for potential detection of cancer cells located in deep tissues. Aim 2 is to develop a highly reproducible and metastatic human prostate cancer model using immunocompromised mice. Aim 3 is to combine Aim 1 and 2 by testing the sensitivity and the specificity of the molecular probe in detecting prostate cancer metastasis and its interaction with tumor microenvironment through the important process of epithelial-to-mesenchymal transition (EMT), which has been closely associated with cancer cell migration and invasion, and appears at the invasion front of many cancers.   Upon completion of this proposed interactive project, we hope to further improve this technology to visualize cancer in live animals and perform real-time studies of the molecular interaction between cancer and its microenvironment.

Table of Contents

Introduction:

Androgen independence and bone metastasis are two lethal phenotypes of human prostate cancer. The current project has three proposed aims. They are: 1) To develop a highly sensitive quantum dot (QD) bioconjugate imaging methodology for the detection of prostate cancer cells in live animals; 2) To develop a highly sensitive and reproducible human prostate cancer bone and visceral metastasis model for studying the molecular steps associated with human prostate cancer progression; and 3) To probe tumor-stroma interaction with special emphasis on interrogating the biological basis of the epithelial-to-mesenchymal transition (EMT) *in vivo* using QD nanotechnology for molecular imaging. In this funding period, we have achieved the following goals:

Body:

Task 1: Develop and characterize nanoparticle QD antibody conjugates capable of binding to prostate cancer cell surface specific antigens (months 1 to 12).

We have completed this task by publishing the epithelial to mesenchymal transition (EMT) model and defined gene expression and behavior changes of the ARCaP cells upon progressing to EMT (The Prostate, 2006, Appendix 1). We have found a number of important cell surface biomarkers, receptor activator of NFκB ligand (RANKL) and IL-13 receptor-α 2 as the potential sites for quantum dot antibody or ligand binding.

Task 2: Evaluate the sensitivity and specificity of the nanoparticle QD antibody conjugates for molecular imaging of human prostate cancer cells and their variants with defined differences in biochemical and behavioral characteristics (months 6 to 12).

This task has been completed. We have evaluated the expression of RANKL expression by ARCaP cells using RT-PCR, western blot, and immunohistochemistry (Figure 1). The expressed RANKL by ARCaP cells is functional as revealed by the ability of ARCaP cells that overexpressed RANKL promoted osteoclastogenesis in an in vitro assay (Figure 2). We conjugated IL-13 receptor-α 2 antibody with visible quantum dots and found the ability of this antibody QD conjugate recognized appropriate cell target (Figure 3). We have completed the comparative aspect of the biochemical and behavior changes of ARCaP cells upon EMT (Please see Appendix 1).

Task 3: Test the ability of selected molecular imaging probes to be used together (multiplexing) for tracking single or aggregated cells in culture (months 6 to 12).

This task is completed where we have successfully multiplexing several QD nanoparticles with emission fluorescence in the visible range for the detection of several molecular markers in prostate cancer cells. The multiplexing technique developed here will be applicable to in vivo imaging of tumors using similar QD approaches.

Task 4: Select quantum dot molecular probes with far-red and near-infrared emitting wave lengths for *in vivo* imaging in animals previously implanted with human prostate tumors (months 12 to 36).

We have described an ultrasensitive method that allows us to visualize human prostate cancer cells in mouse skeleton using bioconjugated near infrared fluorescent QDs. In this study, we have shown a human cancer C4-2 xenografts grown in mouse tibia can be visualized with a PSMA antibody conjugate with QDs emitting light at the near-infrared range of 800nm, or QD800. As few as 5,000 C4-2 cells can be detected when previously tagged with QD800 conjugate and injected directly into mouse tibia (Figure 4). We have successfully applied this imaging technique for the detection of previously formed prostate

tumors in mouse tibia (Figure 5). This technique has been expanded to detect the binding of anti-IL-13 receptor-α 2 on the cell surface of prostate cancer cells in vivo.

Task 5: Develop and characterize an ARCaP human prostate cancer cell model with a predictable pattern of bone and soft tissue metastases (months 1 to 24).

We have isolated ARCaP clones that have differential ability to express EMT markers and the ability to metastasize to the skeleton or soft-tissues (primarily adrenal gland). We also characterized in more detail the ability of maintenance of the gene expression and phenotypes of ARCaP cells in culture permanently. Results of our study show that bone is an efficient environment that can facilitate EMT in human prostate cancer cells transiently upon early interaction. However, if such interaction is allowed to occur for an extended period, permanent phenotypic and behavior changes of the ARCaP cells were observed (Xu et al., *Prostate,* 66(15):1664-73, 2006).

Task 6: Do molecular profiling of ARCaP and ARCaP-derivative cell lines with respect to their gene expression using cDNA microarray and validate such differences using tissue array (months 6 to 18).

We have completed proteomic analysis of ARCaP sublines with respect to their gene expression profiles. This approach was taken using the facility of animals from the microchemical facility, Emory University School of Medicine, for overall proteomics analysis of protein extracts from ARCaP sublines. Differentially expressed genes were confirmed by RT-PCR and western blot in cultured cell lines. Proteomic analysis using the microchemical core facility of Emory University School of Medicine, we have identified 160 proteins with 99% confidence that exhibit differential expression between ARCaP$_E$ and ARCaP$_M$ cells. In particular, we found a gene named epithelial protein lost in neoplasm (EPLIN) that showed differential expression in clinical specimens. We will focus our future attention on further elucidating the molecular mechanisms regulating EPLIN and possible application of this molecular marker for prostate cancer imaging.

Task 7: Assess gene expression profiles in tumors obtained from animals that have been subjected to imaging and characterize gene expression profiling in primary and metastatic tumors using RT-PCR, western blots and IHC (months 18 to 36).

We have developed immunohistochemical analysis of relevant genes that may be expressed by ARCaP cells in animal models. We have completed selected genes that are expressed on the cell surface of prostate cancer cell lines. The expression of these genes will be followed in cancer cells by the use of antibody conjugated nanoparticles on a real time basis.

Task 8: Develop a nanotechnology-based prostate cancer detection technology for both local invasion and distant metastasis with particular focus on EMT in primary and distant metastatic sites (months 1 to 24).

QD800 has been shown to detect prostate cancer growth in mouse tibia. Although we found QD800 can be detected from mouse tibia containing prostate tumors, the sensitivity of this imaging seems to be less than desired. For example, prostate cancer cells colonized in femur have a more difficult time to be detected than similar tumors grown in the tibia. We have developed techniques to visualize tumors using near-infrared organic dyes, which can localize tumors in mice with minimum background activity. Additional studies are being conducted now to confirm if these observations can be validated.

Task 9: Evaluate the sensitivity and specificity of individual nanoparticle QD antibody conjugates as molecular probes for multiplexing numerous cell surface targets simultaneously in mice previously implanted with human ARCaP cells or derivative variants (months 12 to 36).

We have successfully completed the in vitro multiplexing analysis targeting genes related to EMT. We have established tumor growth in mouse skeleton and found that mouse tibia might be the most sensitive site for the detection of prostate cancer bone metastasis. We are exploring the potential use of other QD conjugates that may allow the visualization of human prostate cancer in bone more effectively than the QD800 we are presently testing.

Task 10: Summarize the results, repeat certain studies, and prepare manuscripts for publication (months 12 to 36).

We have completed the publication of one manuscript as seen in Appendix 1-4. Two other manuscripts will be submitted shortly to summarize the biomarkers and the behavior changes of ARCaP cells upon interaction with bone microenvironment, the discovery that RANKL is an important EMT marker and the ability to detect prostate cancer bone metastasis using QD800.

Key Research Accomplishments:

- We have developed an ARCaP model of human prostate cancer progression with focus on EMT.
- We have developed far red and infrared range of quantum dot nanoparticles for *in vivo* imaging of prostate cancer cells in live mice.
- We have developed multiplexing technology to evaluate EMT biomarkers during ARCaP prostate cancer progression and in clinical prostate cancer specimens.
- We have published one manuscript in the Prostate and one review as a book chapter. We have also completed two additional manuscripts and one review.

Reportable Outcomes:

1. During this funding period, four manuscripts have been published (see Appendices 1-4 below).
2. We developed an ultrasensitive detection method for prostate cancer metastasis.

Conclusions:

Quantum dot linked molecules have been shown to be highly effective in the detection of molecular biomarkers associated with EMT in the ARCaP model of human prostatic cancer progression. This technology can be expanded to determine EMT in clinical human prostate cancer tissues. In addition, using near infrared quantum dot probes linked to antibodies designed to target human prostate cancer surface prostate cancer metastases from deep tissues.

References:

None

Appendices:

1. Xu J, Wang R, Xie ZH, Odero-Marah V, Pathak S, Multani A, Chung LWK, Zhau HE. (2006). Prostate cancer metastasis: Role of the host microenvironment in promoting epithelial to mesenchymal transition and increased bone and adrenal gland metastasis. *The Prostate*, 66(15):1664-73.
2. Gao X, Chung LW, Nie S. (2007). Quantum dots for in vivo molecular and cellular imaging. *Methods Mol Biol.* 374:135-46.

3. Chung LW, Huang WC, Sung, SY, Wu D, Odero-Marah V, Nomura T, Shigemura K, Miyagi T, Seo S, Shi C, Molitierno J, Elmore J, Anderson C, Isotani S, Edlund M, Hsieh CL, Wang R, Shehata B, Zhau HE. Stromal-epithelial interaction in prostate cancer progression. *Clinical Genitourinary Cancer*. 5(2):162-70.
4. Xing Y, Chaudry Q, Shen C, Kong KY, Zhau HE, Chung LW, Petros JA, O'Regan RM, Yezhelyev MV, Simons JW, Wang MD, Nie S. (2007). Bioconjugated quantum dots for multiplexed and quantitative immunohistochemistry. *Nat Protoc.* 2(5):1152-65.
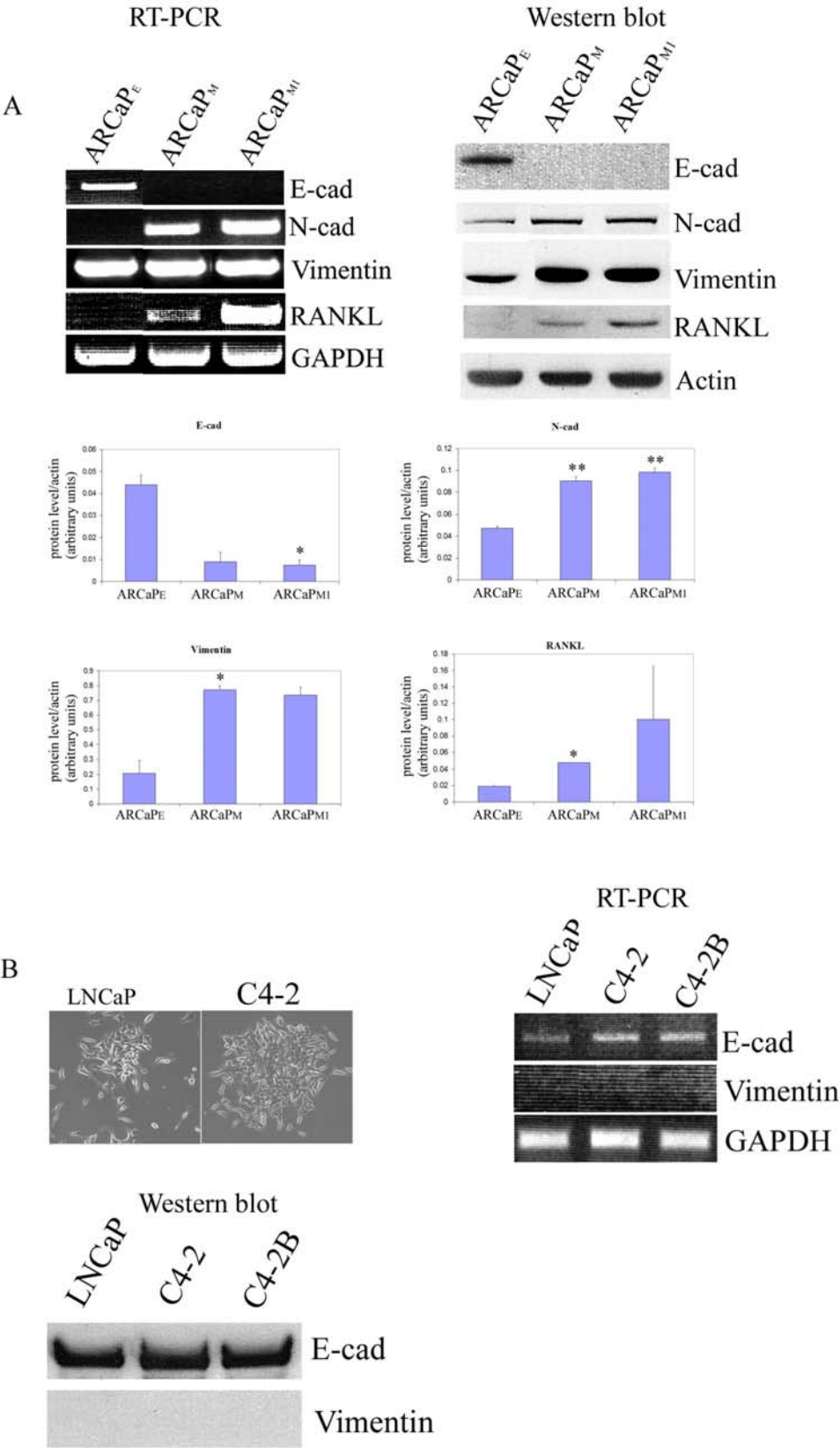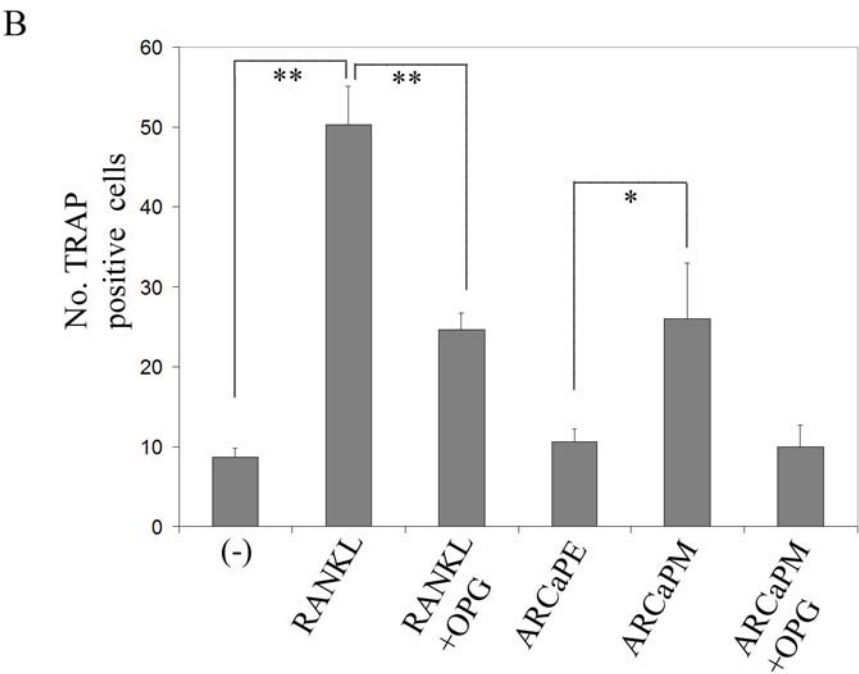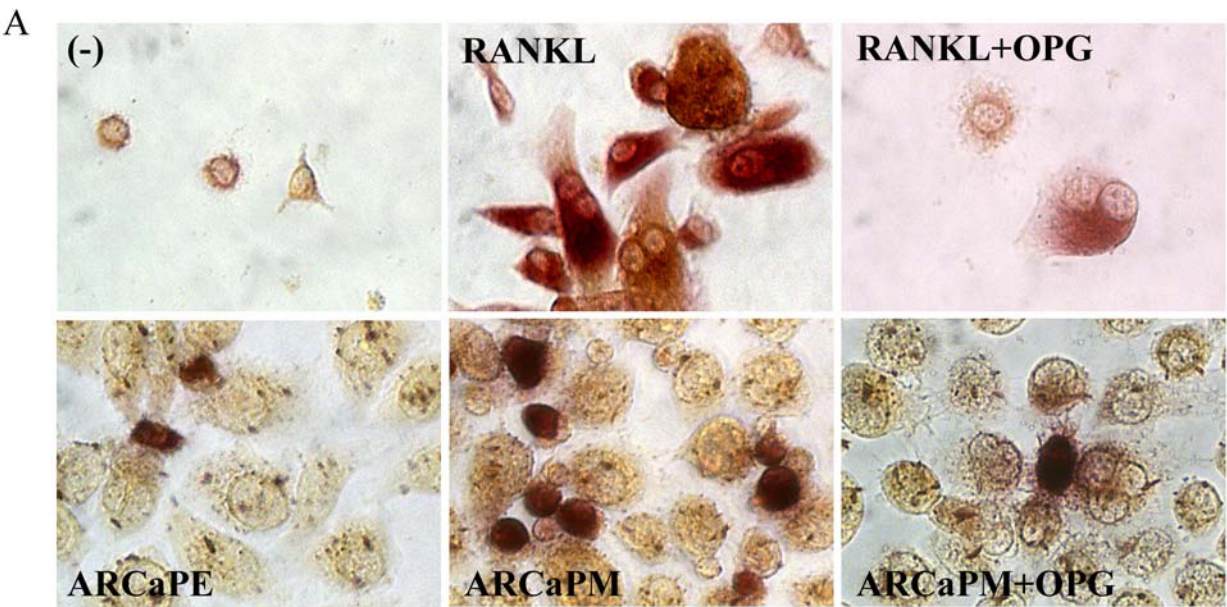
Figures:

Figure 1

Figure 2

A

B

Figure 3

IL-13Rα2 expression in cultured ARCaP cells

	QD	DAPI	Merged

ARCaP_E

ARCaP_M
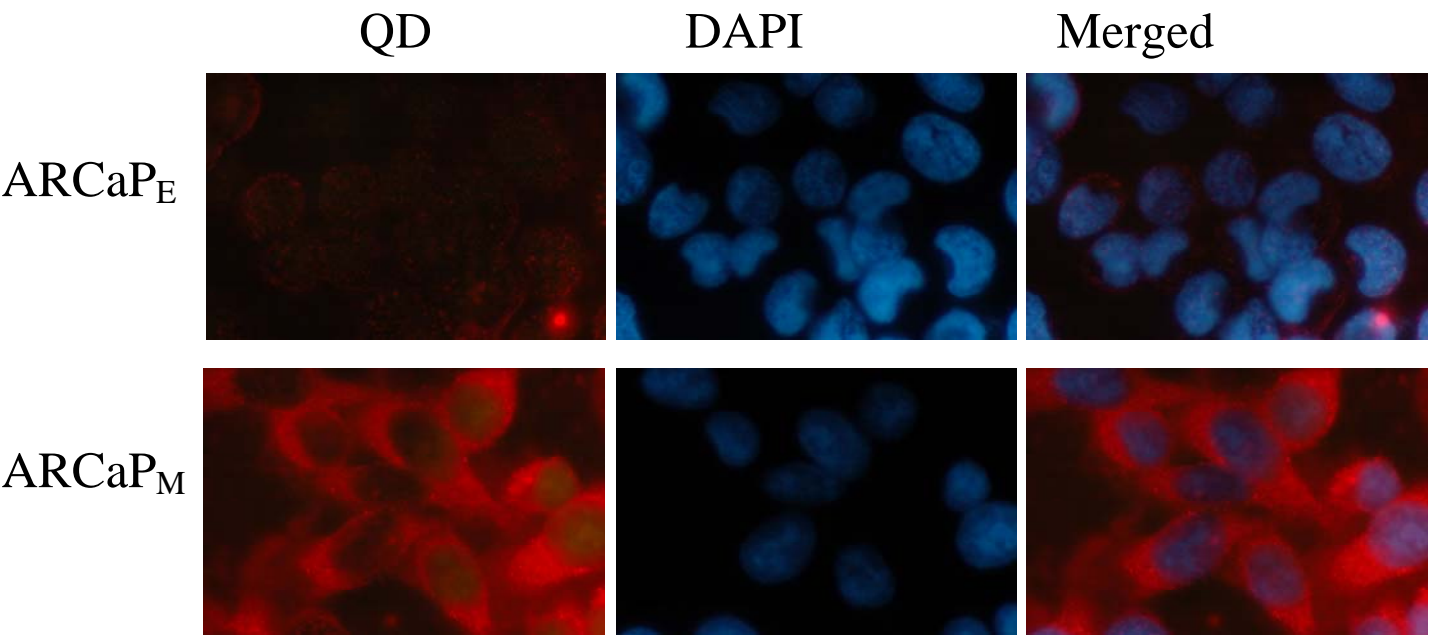
Figure 4
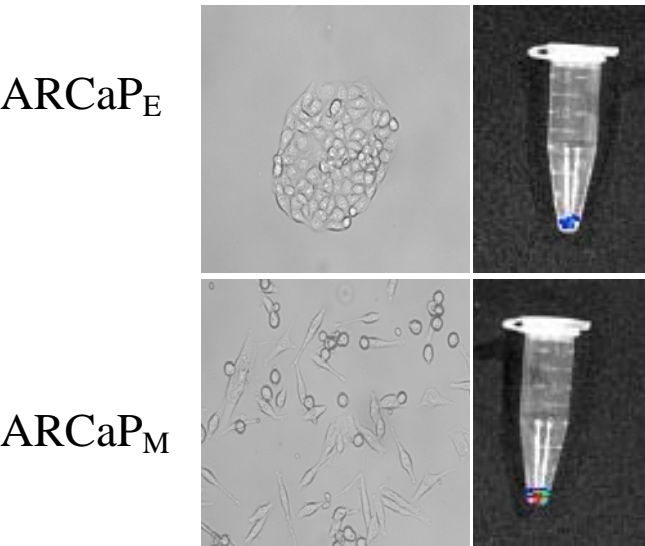
ARCaP_E

ARCaP_M

QD800- IL-13Rα2 Ab tagged ARCaP cells

Figure 5

One mouse with right tibia metastasis from ARCaP$_M$ cells
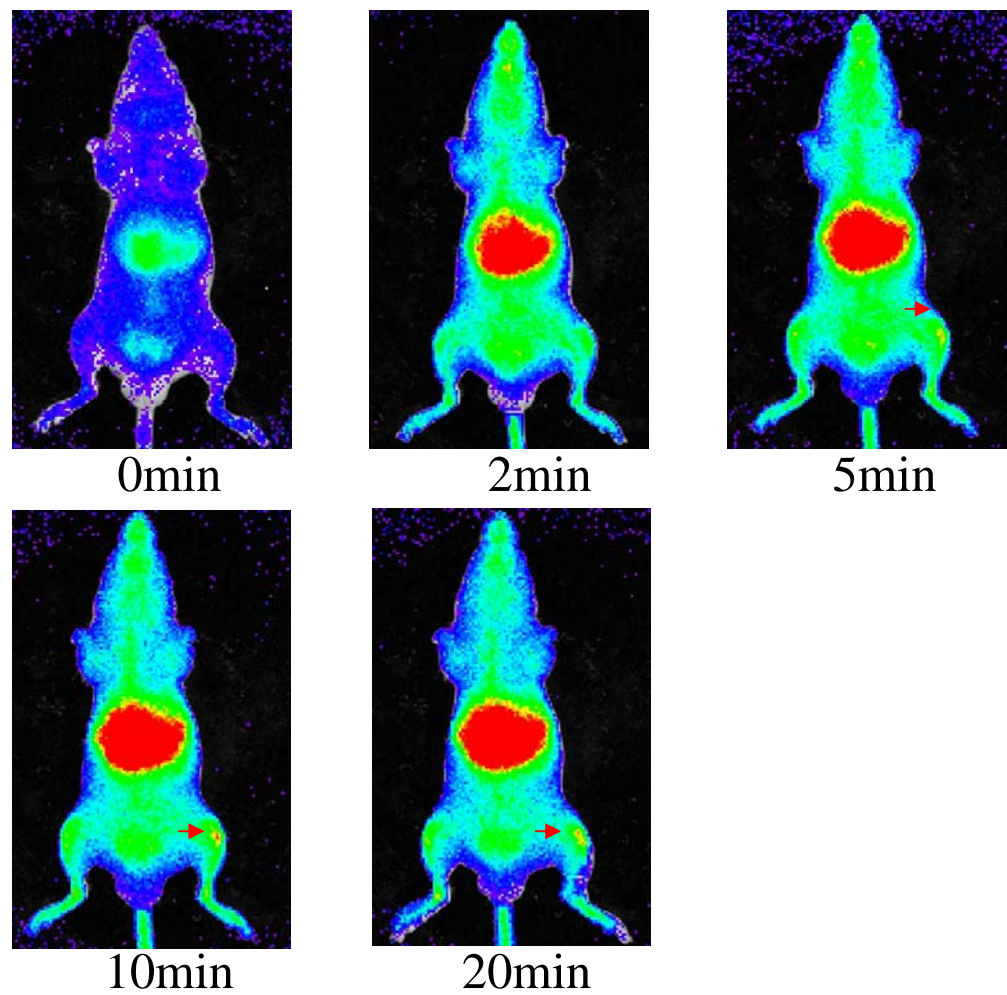
0min   2min   5min

10min   20min

Prostate Cancer Metastasis: Role of the Host Microenvironment in Promoting Epithelial to Mesenchymal Transition and Increased Bone and Adrenal Gland Metastasis

Jianchun Xu,[1] Ruoxiang Wang,[1] Zhi Hui Xie,[1] Valerie Odero-Marah,[1] Sen Pathak,[2] Asha Multani,[2] Leland W.K. Chung,[1] and Haiyen E. Zhau[1]*

[1]*Department of Urology, Molecular Urology and Therapeutics Program, Emory University School of Medicine, Atlanta, Georgia*
[2]*Department of Cancer Biology and Laboratory Medicine, the University of Texas M. D. Anderson Cancer Center, Houston, Texas*

BACKGROUND. The ARCaP cell line was established from the ascites fluid of a patient with metastatic prostate cancer. This study characterized the host microenvironmental role in cancer progression, epithelial to mesenchymal transition (EMT), and bone and adrenal metastasis in parental ARCaP and its derived cell subclones.
METHODS. Cytogenetic profiles, growth, migration, invasion, cellular interaction, drug sensitivities, and gene expression of ARCaP cell subclones were compared. In vivo gene expression, behavior, and metastasis of ARCaP subclones were analyzed by serial intracardiac injections into SCID mice.
RESULTS. ARCaP$_E$ cells, with cobblestone morphology, underwent EMT through cellular interaction with host bone and adrenal gland. Lineage-derived ARCaP$_M$ cells, with spindle-shape fibroblastic morphology, exhibited decreased cell adhesion and increased metastasis to bone and adrenal gland. Cytogenetic analyses of parental and ARCaP subclones confirmed their clonality.
CONCLUSIONS. ARCaP uniquely models the molecular basis of prostate cancer bone and adrenal metastases and epithelial to mesenchymal transition. *Prostate* © 2006 Wiley-Liss, Inc.

KEY WORDS: organ-specific tropism; clonal interaction; cancer cell heterogeneity; animal model; cancer progression

INTRODUCTION

The diversity and heterogeneity of human prostate cancer cells is well appreciated. A broad spectrum of cancer cell behaviors include the ability to grow, invade surrounding normal tissues, and metastasize to distant organs [1–3]. Despite similarities in the histologic presentation of prostate cancers at the time of disease diagnosis, their clinical behaviors, including time to disease progression and metastasis, sensitivity to hormones, chemotherapy and radiation, and propensity to relapse still cannot be predicted with certainty [4–7]. Relevant models that could probe the phenotype, behavior, and progression of cancer cells are lacking, as well as appropriate methods and sensitive biomarkers that can diagnose disease and reliably predict its

WILEY InterScience®
DISCOVER SOMETHING GREAT

clinical behavior early on. However, investigations have revealed a wealth of fresh information on the molecular basis of cancer metastasis through: (1) the development of useful transgenic [8–10] and xenograft [11–18] animal models and human prostate cancer cell lines [3]; (2) characterization of the genetic diversity and heterogeneity of cancer cells and animal models; (3) the identification of specific loci that may harbor genes or clusters of genes contributing to the development of familial or sporadic forms of prostate cancer [19–21]; and (4) elucidation of intracellular cell signaling and the roles of autocrine and paracrine factors in the tumor milieu that control the behavior of prostate cancer cells in interaction with the tumor microenvironment [2,3,22–24]. Because prostate cancer has a predilection to metastasize to bone, resulting in increased patient mortality and morbidity, we sought to develop a highly metastatic prostate cancer model to evaluate the involvement of epithelial to mesenchymal transition (EMT) and the host microenvironment in prostate cancer bone and soft tissue metastases. This communication reports the cytogenetic, phenotypic, and behavioral characterizations and gene expression profiles of parental ARCaP and ARCaP cell subclones subsequent to cellular interaction with mouse host cells in vivo.

MATERIALS AND METHODS

Cell Culture

ARCaP cells were derived by our laboratory from the ascites fluid of a patient with metastatic carcinoma of the prostate [16]. Cells were routinely maintained in a culture medium consisting of T medium (Life Technologies, Gaithersburg, MD) and 5% fetal bovine serum (FBS) at 37°C supplemented with 5% CO_2. Limited dilution was performed by suspending 400 cells in 60 ml of T medium and seeding 100 µl per well in six 96-well plates. The wells containing one cell were expanded. Cell growth was determined by crystal violet assay [25]. In brief, cells (3×10^4 per well) were trypsinized and resuspended in T medium and seeded in 24-well plates under routine culture conditions. One plate of cells was removed at each designated time point and fixed with 0.5 ml of 1% glutaraldehyde for 15 min, stained with 0.5% crystal violet solution for 15 min, rinsed four times with water, air dried then eluted by Sorenson's solution for 30 min at room temperature. The optical density of the eluted solutions was read at 590 nm. The OD_{590} was determined by an APECTRAmax 190 Microplate Reader and directly correlated with the number of cells [25]. Conditioned media (CM) were collected from cells reaching 80% confluence, rinsed with PBS, replaced with serum-free T media and 2% TCM (Celox Laboratories, Inc., St. Paul, MN) and cultured for 24 hr. The effects of CM on cell growth were determined in triplicate assays of three independent experiments with data expressed as average ± SEM.

Invasion and Migration Assays

A total of 35 µl of Matrigel Matrix (BD Biosciences, Bedford, MA; 100 µg/cm^2 surface area; diluted 1:5 in T medium) was placed on the inner upper Boyden chamber (BIOCOAT, 6.4 mm insert with 8 µm pores; Becton Dickinson Labware, Bedford, MA) and incubated for 30 min prior to adding to the cells. Cells (5×10^4) were suspended in 500 µl of 0.1% BSA/T medium and added to the inner upper Boyden chamber. One milliliter of 0.1% BSA/T medium was added to the outer Boyden chamber. The chambers with or without Matrigel were placed in 24-well plates and incubated for 48 hr. MTT solution (2.5 mg/ml; Sigma, St. Louis, MO) was added to both the inner (40 µl) and the outer (80 µl) chambers and incubated for an additional 4 hr. The media were collected separately from each chamber, and cell-associated MTT crystals were scrubbed off with filter paper and dissolved separately in 500 µl dimethyl sulfuroxide (DMSO). The color intensity was measured at 590 nm against the appropriate blank controls (0.1% BSA/T medium with MTT solution and 500 µl DMSO). The % invasion was calculated by MTT eluted from cells invaded through the Boyden chamber/MTT eluted from cells that remained in the upper Boyden chamber plus those that invaded through the Boyden chamber. The % migration was conducted and calculated similarly to cell invasion, except the Boyden chambers were not coated with Matrigel [26,27]. Relative invasion, migration, and growth are presented as average ± SEM of triplicate assays from two independent experiments.

In addition, migration was also determined by scratch wound assay [28] where cells (5×10^5) were cultured in a 24-well plate. Then the 100% confluent cell layers were wounded with two parallel scratches using a sterile 200 µl pipette tip and rinsed with PBS. Images were taken at 0, 12, 24, 36, and 48 hr at the marked site using a ZEISS Axiovert 200 M inverse light microscope (at 4×) and Openlab software (Improvision, Coventry, UK). Five measurements were taken from 0 to 48 hr. Mean widths were determined as a function of time with % migration tabulated as (Width 0 hr − Width at 12 to 48-hr) ÷ Width 0 hr × 100%.

Chemotherapeutic Sensitivity of Parental ARCaP and ARCaP Cell Subclones

Cells (5×10^3 per well) were cultured in 96-well plates for 24 hr and then replaced with fresh cultured

medium to which were added Paclitaxel, Etoposide, or Doxorubicin (Sigma, St. Louis, MO) at four different concentrations, followed by incubation for 96 hr. Cell growth was measured using the MTT assay.

Cytogenetic Analysis

Cells at 75% confluence in fresh media were exposed to Colcemid (20 ng/ml; Sigma) for 30 min at 37°C, rinsed two times with Hanks' balanced salt solution, and exposed to 0.01% trypsin for 5–7 min. The dislodged cells were neutralized with RPMI 1640 containing 10% FBS, and centrifuged at 1,700 rpm for 5 min. The cell pellet was disturbed and exposed to a hypotonic solution (0.06 M KCl) for 20 min at room temperature. After centrifugation, the cells were fixed in acetic acid: methanol (1:3, v/v) for 15 min, rinsed three times with the fixative and stained with Giemsa solution for G-banding following routine procedures [16]. Five to ten G-banded metaphase spreads were photographed for chromosome analyses for each cell clone.

Protein Expression

Immunohistochemical (IHC) and Western blot were used to determine the level of protein expression in cells. Monoclonal antibodies against cytokeratin 18/19 (CK18/19) were obtained from Santa Cruz Biotechnology, Inc. (Santa Cruz, CA); vimentin (VM) antibody from Dako Corp., Ltd. (Carpinteria, CA). Polyclonal antibodies to E-cadherin and N-cadherin were obtained from Santa Cruz. For immunohisto-chemical analysis, acetone (−20°C)-fixed cells or deparaffinized tissue sections (4 μ) were treated with 3% hydrogen peroxide, blocked with Super Block (Scytek Laboratories, Logan, UT), avidin and biotin (Vector Laboratories, Inc., Burlingame, CA) for 15 min each, and incubated with primary antibody overnight at 4°C. The signals were amplified by an avidin–biotin HRP system using multilink and label reagents (BioGenex, San Ramon, CA) and hydrogen peroxide/DAB (3, 3′-diaminobenzidine) as peroxidase substrate and chromogen (Sigma). Background activity was determined by (1) eliminating the primary antibody, (2) using matching mouse immunoglobulin subtypes, or (3) normal goat or rabbit serum at appropriate dilutions. For Western Blot Analysis, cells were harvested at 80% confluence and rinsed twice with cold PBS. Cellular protein was extracted in a homogenization buffer (phosphate buffered saline with 1% Nonidet P-40, 0.5% sodium deoxycholate, 0.1% SDS, 10 mg/ml phenylmethylsulfonyl fluoride (PMSF), 1 mM sodium orthovanadate, 1 μg/ml leupeptin, and 1 μg/ml aprotinin). The total cell lysate (7.5–20 μg) was resolved by 7.5 or 10–20% SDS–polyacrylamide gel electrophoresis and transferred to a nitrocellulose membrane (NitroPure, Osmonics, Westborough, MA). The membrane was blocked for 1 hr at room temperature with 5% nonfat milk in TBST buffer (50 mM Tris-HCl, 150 mM NaCl, 0.05% Tween 20) and incubated with primary antibody in TBST blocking buffer for 1 hr at room temperature. The signal was detected by reacting with secondary antibody conjugated to horseradish peroxidase coupled with enhanced chemiluminescence (ECL) reagents (Amersham-Pharmacia Biotech, Piscataway, NJ), and exposed on Hyperfilm (Amersham).

Tumorigenicity and Metastasis In Vivo

Five to seven-week-old athymic NCr-nu/nu male mice (NCI) were used as hosts. Cells at 80% confluence were changed with fresh T-medium the day before harvest. Cells were resuspended (2×10^7/ml) and injected subcutaneously (1×10^6 cells/100 μl/site, four sites per mouse). For intracardiac injection, cells were injected as 5×10^5 cells/50 μl PBS/mouse using a 28G1/2 needle. Mice were anesthetized and placed in a supine position. The needle was inserted 5 mm above the middle of the left side of sternum. When fresh arterial blood appeared in the syringe, this indicated the successful penetration into the left ventricle. Cells were infused slowly and directly into mouse left ventricle for systemic circulation. Tumor formation was monitored weekly and volume calculated as length × width × height × 0.5236 [25,26]. Metastases to distant organs were confirmed by radiography, necropsy, and histomorphology of the tumor specimens.

Derivation of Cell Subclones From Tumor Tissues

Tumor tissue was freshly harvested, rinsed three times with PBS, replaced with cold PBS with antibiotics (Penicillin/Streptomycin (10,000 U/ml), placed on ice for 5 min, changed to cold T medium with 10% FBS and antibiotics, and kept on ice. Tissue was cut into 0.5–1 mm³ pieces, put in cell culture dishes (separating at 0.5–1.0 cm), and briefly air dried to allow attachment. One to 2 drops of culture media were added on top of and around the tissue pieces to keep them humid and incubated. A few more drops of media were added 6 hr later followed by more media at 24 and 48 hr. Tumor cells and mouse stromal cells started to emerge by 48 hr with spindle-shape cells around the tissue and epithelial-like cells migrating away from the tissue piece, forming a rather "pure" colony by Day 7–10. We used cloning disks (Scienceware, Pequannock, NJ) to isolate pure cell subclones. Additional contaminating stromal cells were removed from epithelial cells by differential trypsinization [26].

RESULTS

ARCaP Subclones Have Similar Cytogenetic Profiles but Distinct Morphology, Growth Rates, Gene Expression Profiles and Behaviors In Vitro

The ARCaP cells were originated from the ascites fluid of a patient with prostate cancer bony metastasis [16]. The ARCaP cells harbor wild type androgen receptor (AR) and secrete low level of prostatic specific antigen (PSA) as compared to LNCaP cells. In contrast to LNCaP cells, parental ARCaP cells are invasive and cell growth is repressed by androgen both in vitro and in vivo. Figure 1 shows five ARCaP cell subclones obtained by dilution cloning with marked differences in their morphology, ranging from cobblestone epithelial (IF11 or ARCaP$_E$) to spindle-shape mesenchymal cells (IA8 or ARCaP$_M$). Clones IID4 and IIC11 gave rise to morphologic features intermediate between ARCaP$_E$ and ARCaP$_M$. One of the subclones, IF3, exhibited giant cell morphology with multinuclear features resembling matured osteoclasts. The growth rates of the five ARCaP cell subclones in vitro showed the mesenchyme-like ARCaP$_M$ as the fastest, followed by IIC11, IID4, and IF3, with the epithelium-like ARCaP$_E$ being the slowest (data not included).

Cytogenetic Analyses

Cytogenetic analyses of parental ARCaP and the five cell subclones (Table I) indicated that these cells are clonal. These subclones exhibited the same major marker chromosomes as ARCaP parental cells [16]. However, each of the ARCaP cell subclones had its unique marker chromosomes. During the course of this study, both the morphology and the cytogenetic profiles of parental ARCaP and its subclones were stable despite repeated subculturing of the respective cells in vitro for more than 20 passages (unpublished results). The ARCaP cytogenetic profile [16] is distinct from the widely studied LNCaP cells [26]. They do not share common marker chromosomes and can easily be identified and distinguished from each other based on their distinctive marker chromosomes. While the ARCaP subclones have distinct cytogenetic profiles, they also differ in their histomorphology, growth rate, migratory, invasive, and metastatic potentials, and drug sensitivity (see Results). These properties are maintained in the mixed parental ARCaP cells by cell–cell interaction.

Growth, Migration, and Invasion of ARCaP$_E$ and ARCaP$_M$ Subclones In Vitro

Since EMT has been associated with increased cancer cell invasion and migration [29–31], we evaluated the possible correlation between two morphologically distinct ARCaP subclones, cobblestone-shaped ARCaP$_E$ and the spindle-shaped ARCaP$_M$ subclones. Cell invasion using a Boyden Chamber coated with a Matrigel barrier (Fig. 2A), and migration as assessed by Scratch Wound Assay (Fig. 2B) correlated with cell growth rates (Fig. 2C), revealed higher migration and invasion by ARCaP$_M$ than ARCaP$_E$ cells ($P < 0.01$). These two clones, after co-culturing (1:1) for more than 20 passages, still retained their original distinct morphology as seen in Figure 1 without one clone being preferentially "selected" over the other (data not included). We hypothesize that clonal interaction
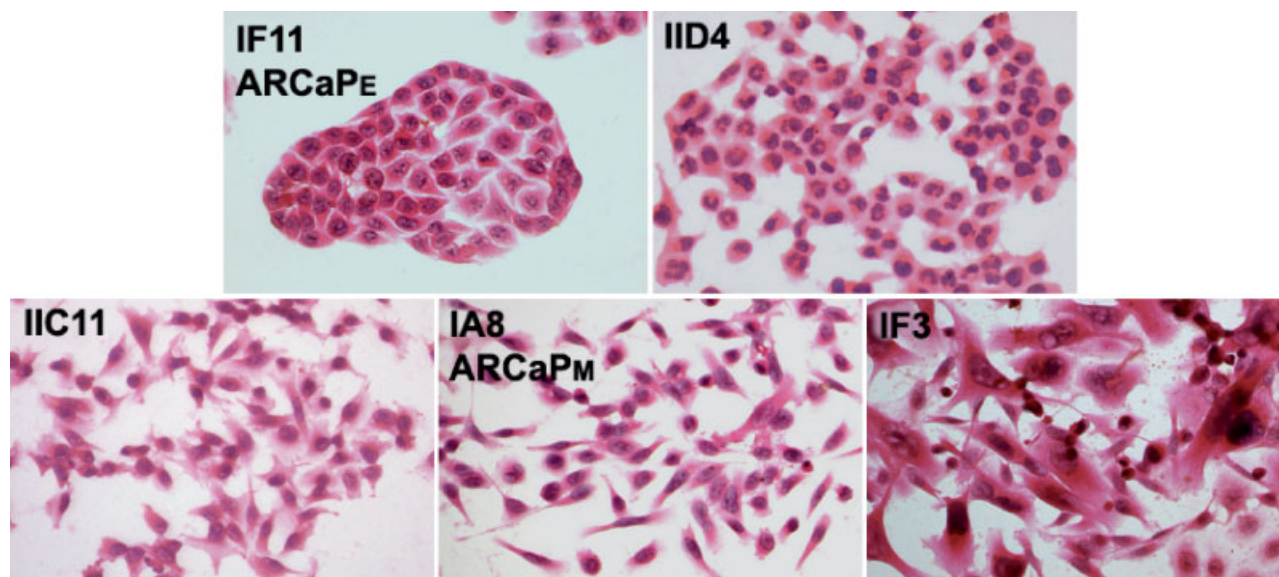

Fig. 1. Histomorphology of ARCaP cell subclones ranged from cobblestone-shaped ARCaP$_E$ to spindle-shaped ARCaP$_M$ cells.

TABLE I. Cytogenetic Profiles of Parental ARCaP and Its Five Cell Subclones

Cells	1p+	1q+	del5q	5p+	6p+	del8p	i(9q)	12q+	15p+	18q+	21p+	delX	t(13:15)	8q+	i(5q)	6q+
IIC11	+	+	+	+	+	+	+	+	+	+	+	+	−	−	−	−
ARCaPM	+	+	+	+	+	+	+	+	+[a]	+	+	+	+[b,a]	−[a]	−	−
ARCaPE	+	+	+	+	+	+	+	+	−[a]	+	+	+	−[a]	+[b,a]	−	−
IID4	+	+	+	+	+	−	+	+	+	+	+	+	−	−	+[b]	−
IF3	+	−	+	+	+	+	+	+	+	+	+	+	−	−	−	+[b]
ARCaP	+	−	+	+	+	+	−	+	−	+	−	+	−	−	−	−

[a]Difference between ARCaP$_M$ and ARCaP$_E$.
[b]Difference among the five subclones.

occurs through factors secreted by one cell type exerting either a growth stimulatory or inhibitory effect on the other. To test this hypothesis, we replaced the cultured media of ARCaP$_E$ with conditioned media (CM) collected from ARCaP$_M$ and vice versa. Figure 3 showed that CM from the fast-growing ARCaP$_M$ cells stimulated the growth of the slow-growing ARCaP$_E$ cells ($P < 0.01$), but there was no growth inhibitory effect when the reverse experiment was conducted. These results suggest that a stimulatory rather than inhibitory factor plays a role in the maintenance of ARCaP$_E$ and ARCaP$_M$ subclones within the ARCaP cell population (see below).

Gene Expression Profiles of ARCaP Subclones Grown in Culture

We conducted gene profile analysis of ARCaP subclones with specific emphasis on ARCaP$_E$, ARCaP$_M$, and ARCaP-Ad (Adrenal). We found that, consistent with their morphologic features, ARCaP$_E$ expressed dominantly epithelial markers while ARCaP$_M$ and ARCaP-Ad expressed mesenchymal markers (Fig. 4), as evaluated by Western blots and

IHC. These results were also confirmed by RT-PCR (data not included). Because of these morphologic and molecular characteristics thus the names ARCaP$_E$, ARCaP$_M$, and ARCaP$_{Ad}$ were given to IF11, IA8, and ARCaP-Adrenal subclones respectively. ARCaP$_E$ expressed higher E-cadherin and cytokeratins 18 and 19 typically associated with epithelial cells, whereas ARCaP$_M$ and ARCaP$_{Ad}$ expressed more genes associated with mesenchymal cells, such as elevated vimentin and N-cadherin expression with concomitantly lower expression of epithelium-associated E-cadherin and cytokeratin genes. In addition to the classic EMT-associated genes, we also detected elevated protein expression of PSA, AR, and PSMA and two new EMT-associated genes in ARCaP$_M$ than that in ARCaP$_E$ (data not included).

Effects of Chemotherapeutic Agents on In Vitro Growth of ARCaP Cell Subclones

Because ARCaP represents a lethal form of human prostate cancer with the ability to invade and metastasize aggressively to bone and soft tissues, we sought to determine the in vitro sensitivities of ARCaP$_E$ and
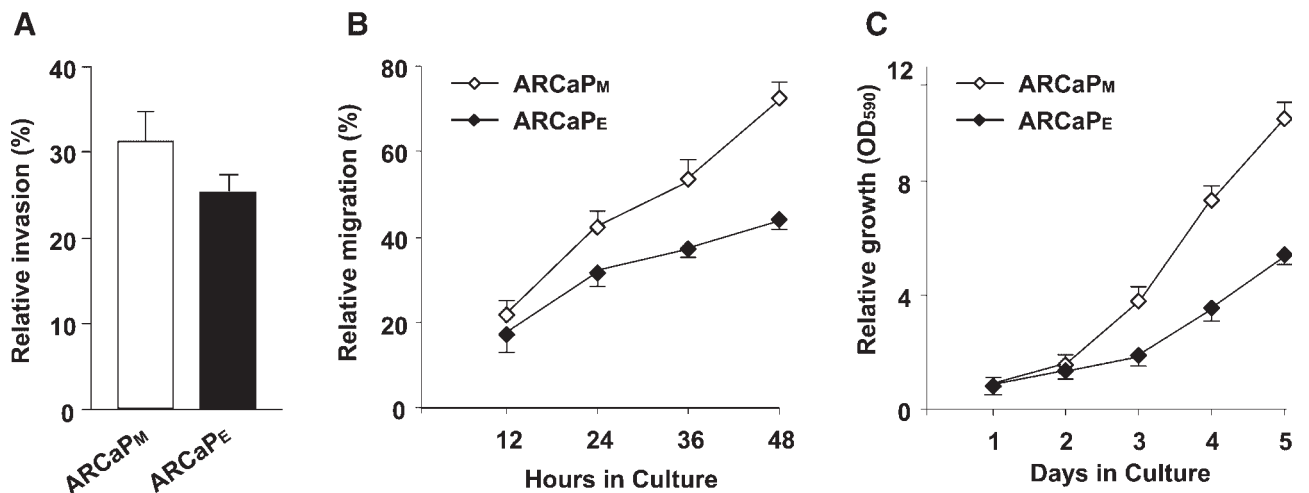
Fig. 2. ARCaP$_M$ cells exhibit higher invasion (**A**), migration (**B**), and growth rate (**C**) than ARCaP$_E$.
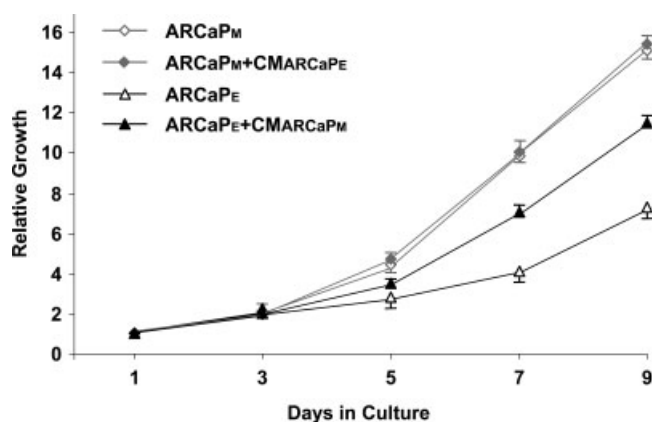
Fig. 3. Conditioned medium derived from fast-growing ARCaP$_M$ subclone stimulated the growth of slow-growing ARCaP$_E$ cells.

ARCaP$_M$ to several clinically used chemotherapeutic drugs and compared the results to invasive LNCaP lineage C4-2 cells treated with the same drugs. We found that ARCaP$_M$ and ARCaP$_E$ are more resistant to a DNA intercalating agent, doxorubicin (IC50s 5.5 and 3.4 uM for ARCaP$_M$ and ARCaP$_E$, respectively) than C4-2 cells (IC50, 2.7 uM). ARCaP$_M$ and ARCaP$_E$ are also more resistant to topoisomerase inhibitor II, etoposide (IC50s 5.8 and 8.1 uM, respectively) than C4-2 cells (IC50, 5.6 uM). The relative resistance of ARCaP$_M$ and ARCaP$_E$, compared to C4-2 cells, to the microtubule/tubulin assembly binding agent, paclitaxel, was also observed with IC50s at 39, 53, and 23.5 nM, respectively.

Comparison of the Tumorigenicity and Metastatic Potentials of ARCaP$_E$ and ARCaP$_M$ in Mice, and the Derivation of ARCaP$_M$-Like Cells From Bone and Adrenal Gland Harvested From Animals Inoculated With ARCaP$_E$ Cells

To confirm that differences in morphology, cell behavior, gene expression profiles, and sensitivity to chemotherapeutic drugs between ARCaP cell subclones in vitro reflect their tumorigenicity and metastatic potential in vivo, we conducted animal studies by inoculating two ARCaP cell subclones, ARCaP$_E$, and ARCaP$_M$, into the left ventricles of immune-compromised SCID mice. The animals were observed closely and bone and soft tissue metastases were confirmed by X-ray, physical palpation, and histomorphology. Figure 5 showed the histopathology (top panels) and vimentin expression (IHC, bottom panels) of primary tumors from ARCaP$_E$, ARCaP$_M$, and metastatic lesions of bone and adrenal gland in mice inoculated intracardiacally with ARCaP cells. Similar to our experience in the orthotopic injection of parental ARCaP cells [16], tumor cells induced mixed osteoblastic and osteolytic responses in mice upon intracardiac injection of ARCaP subclones. Some mice also exhibited apparent cachexia and paraplegia at the later stage of bone metastasis (data not included).

The EMT-associated elevated expression of vimentin was demonstrated in ARCaP bone and adrenal meatastatic tumors as comparing with the primary tumor (Fig. 5). We derived ARCaP cell subclones from bone and adrenal gland metastases and further tested
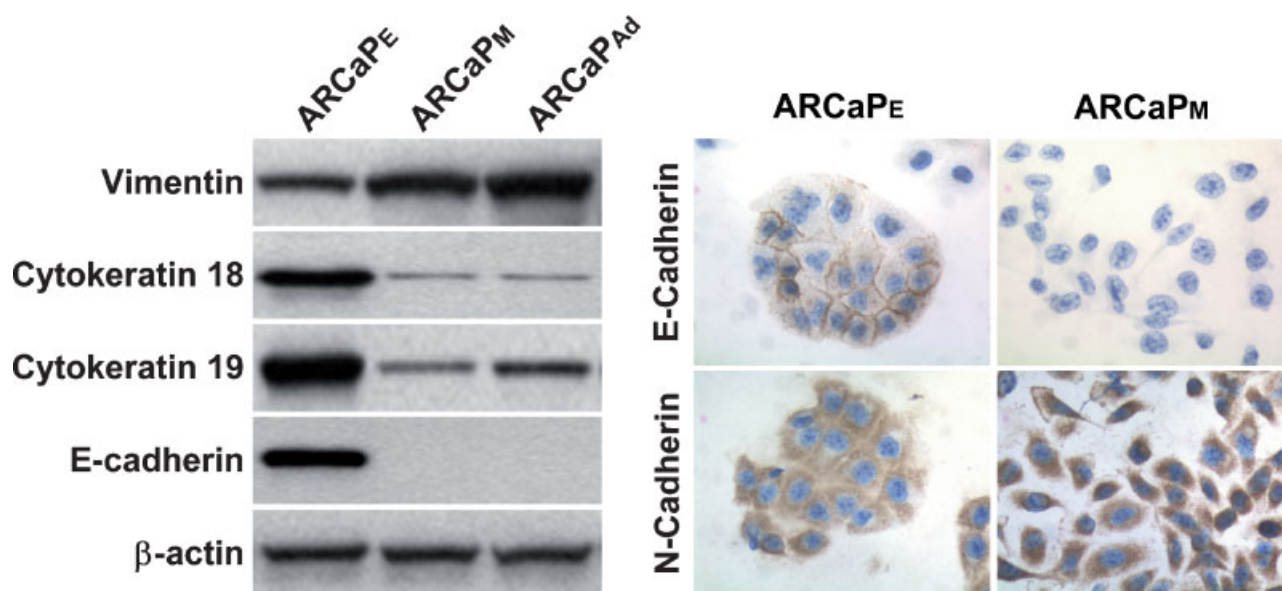

Fig. 4. Protein expression profile changes from ARCaP$_E$ to ARCaP$_M$ and ARCaP$_{Ad}$ are closely associated with epithelial to mesenchymal transition. Western blot (**left panel**), IHC (**right panel**).
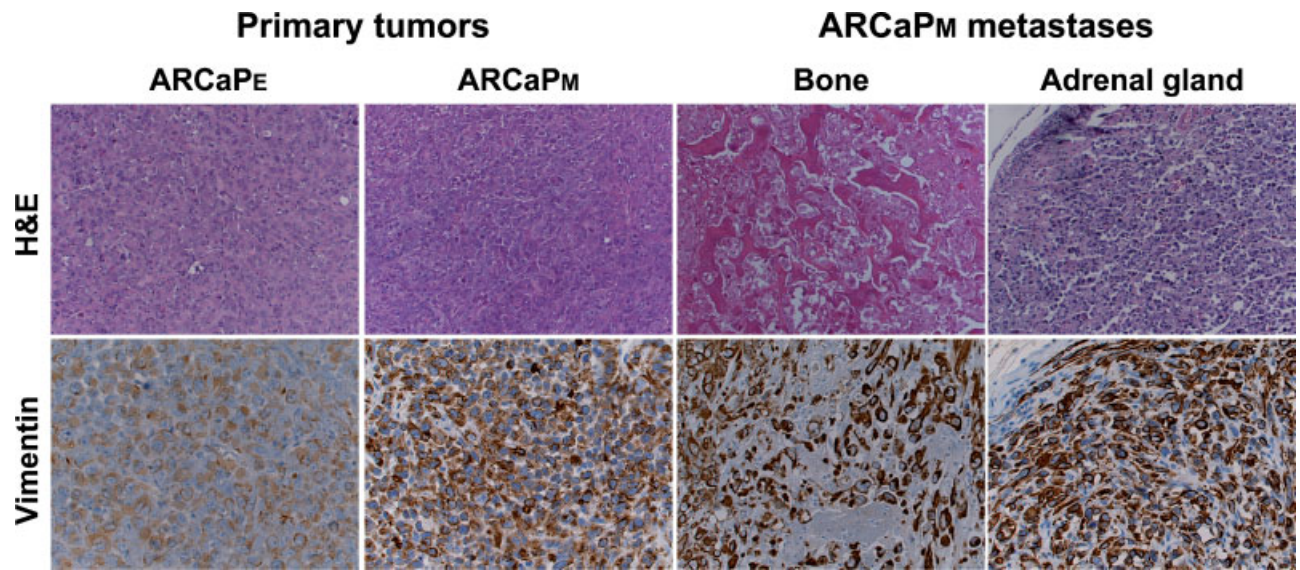
Fig. 5. Histomorphology (**top panel**) and vimentin expression (IHC, **bottom panel**) of primary tumors of ARCaP$_E$, ARCaP$_M$, metastatic bone, and adrenal gland induced by intracardiac injections of ARCaP$_M$ cells in athymic mice.

their metastatic potentials in mice. The incidence of bone metastasis ranged from 12.5% (1/8) for ARCaP$_E$ cells, with a latency of 71 days, to 100% (9/9) for ARCaP$_M$ cells, with a latency of 61 days (range 40–104 days). Interestingly, consistent with these observations, increased bone metastasis resulted from ARCaP cell interaction with mouse bone, through recycling of the injected ARCaP$_E$ or ARCaP$_M$ cells in the mouse hosts. Mice inoculated with ARCaP$_E$ or ARCaP$_M$ cells also developed increased adrenal gland metastasis, from 22% (4/18, latency 132 days, range 70–165 days) to 33% (3/9, latency 96 days, range 77 to 135 days). Remarkably, ARCaP$_{Ad}$ metastasized only to host adrenal gland. We observed that both ARCaP$_{Ad}$ and ARCaP$_M$-like cells derived from ARCaP$_E$ had altered morphology and gene expression profiles (Fig. 4) resembled mesenchymal cells, suggesting that the bone and adrenal gland microenvironments had promoted EMT by facilitating the trans-differentiation of ARCaP$_E$ cells toward ARCaP$_M$ with preferential metastasis to bone or adrenal gland. In addition to adrenal gland, a low frequency of host mice also developed lymph node, liver, and lung metastases (data not included).

DISCUSSION

We established an ARCaP human prostate cancer cell model to study the possible relationship between the host microenvironment, EMT, the critical transition of prostate cancer cells from epithelial to mesenchymal phenotype, [29–31], and the propensity of prostate cancer to metastasize to bone and soft tissue. We also correlated EMT with increased cell growth, migration,

and invasion in vitro. EMT has been reported during embryonic development. The invasion front of the developing organ resembles that of the tumor, exhibiting increased cell motility, invasion, and migration as observed in breast and bladder cancers. In the ARCaP human prostate cancer progression model, EMT can be promoted by cellular interaction between an ARCaP human prostate cancer cell subclone, ARCaP$_E$, and host bone or adrenal gland. The derivative ARCaP$_M$ and ARCaP$_{Ad}$ cells have the propensity to metastasize to bone and adrenal gland, respectively. Through further cellular interaction with host adrenal gland, we derived a secondary generation of ARCaP$_{Ad}$ cells. We observed, remarkably, that second generation ARCaP$_{Ad}$ cells had their ability to metastasize restricted only to the host adrenal gland. Because of the similarities in cell morphology, gene expression profiles, and behavior of ARCaP$_M$ derived from ARCaP$_E$ through in vivo selection as a bone metastasis variant and the ARCaP$_M$ IA8 subclone originally isolated from the ARCaP cells, we suggest that IA8 derived from IF11 through EMT transdifferentiation and the interaction of ARCaP$_E$ with the host bone. Following cellular interaction between human prostate cancer ARCaP$_E$ cells and the mouse host, we observed changes in morphology, gene expression, and behavior in this cell clone to resemble a mesenchymal cell type, express mesenchymal genes, and show increased invasion and migration in vitro and metastasis to bone and adrenal gland in live mice (Fig. 2–5). The changes in gene expression profile, such as increased expression of vimentin and N-cadherin and decreased expression of E-cadherin and cytokeratin18 and 19, are consistent

with the morphologic switch of ARCaP cells by EMT, with increased metastatic potential, as reported in several other tumor types [32–35]. We suggest that the host microenvironment plays an important role in facilitating EMT and subsequent prostate cancer metastasis to the skeleton and soft tissues [3]. We observed that despite the clonal origin of ARCaP cells, they present as distinct morphologic and molecular variants with diverse ability to metastasize to bone and adrenal gland. Our results suggest that soluble stimulatory factor(s) secreted by prostate cancer cells may be responsible for the maintenance of tumor cell heterogeneity in ARCaP cells when cultured in vitro (Fig. 3). These observations are consistent with the published literature, where soluble factors such as TGFβ and/or EGF can confer EMT in cultured cells, resulting in altered cell growth and behaviors such as cell motility, invasion, and metastasis in vitro [29,31,33,35].

The fact that host interaction enhances EMT and promotes ARCaP cells to migrate, invade, and metastasize in this model suggests that clinical bone and adrenal gland metastases of prostate cancer cells may be acquired and facilitated by cellular interaction with host microenvironment. Based on the results of this and our previous studies [3,15,16,26], it is likely that resident fibroblasts in the prostate, bone, or adrenal gland or cells recruited from hosts, such as inflammatory and marrow stem cells [36–38], can instigate prostate cancer cells to gain increased malignant potential through the local production of soluble factors, reactive oxygen species and/or extracellular matrices that prompt the tumor cells for enhanced growth and metastasis [30,35,37,38]. Using marginally tumorigenic LNCaP cells as model, we showed previously that co-inoculating LNCaP cells with either non-tumorigenic human prostate stromal fibroblast or a human osteosarcoma cell line [25,39] formed large chimeric tumors. By cloning LNCaP cells from the chimeric tumors, we established lineage-derived LNCaP sublines C4-2 and C4-2B cells which, like other variants [25,39,40], exhibited increased lymph node and bone metastasis. Similar results, that is, an increased propensity for local tumor formation and distant metastases, were obtained with ARCaP cells as described in the present communication and other human prostate cancer cell lines, whereby a human prostate cancer cell line when injected alone, without the presence of stromal fibroblasts, but with recruited host stromal cells, can promote prostate cancer progression [41–43]. We posit that ARCaP interaction with bone or adrenal gland promotes irreversible EMT with subsequent increased invasive and migratory potential and the ability to metastasize to bone and soft tissues.

The demonstration that ARCaP cells undergo EMT in bone or adrenal gland and gain metastatic potential for various sites has several important clinical implications for controlling cancer growth and metastasis. First, the host microenvironment includes soluble and insoluble factors associated with or secreted by osteoblasts, osteoclasts, marrow stromal, or stem cells that could play key roles promoting EMT, an important molecular transition by which cancer cells gain increased metastatic potential in response to the changing tumor microenvironment. These interactions could result in the promotion of cancer cell metastasis to soft tissues such as the adrenal gland, a documented site for human prostate cancer metastasis [44]. Second, if EMT acquired by prostate cancer cells following cellular interaction with host bone or adrenal gland occurs in patients, this could be a potential target for prevention and treatment strategies. Third, since the host microenvironment was shown to promote EMT and prostate cancer progression, host-stroma-directed targeting of prostate cancer such as by the use of atrasentan [45], bisphosphonates [46], growth factor receptor antagonists [47], antiangiogenics [48], and radiopharmaceuticals [49], should be further explored to improve the treatment of cancer metastases.

CONCLUSIONS

We demonstrated that the host microenvironment is a critical site for the transition of human prostate cancer cells from epithelial to mesenchymal morphology, resulting in increased metastatic potential for bone and adrenal gland. Clonal prostate cancer cells could have different histomorphologies, gene expression profiles, sensitivity toward cancer therapeutic drugs, and variable behaviors in culture and in the host. We found that clonal interaction, possibly mediated by soluble factors secreted by prostate cancer cells, is responsible for maintaining tumor cell heterogeneity. Our study documented that EMT can be facilitated through cellular interaction between human prostate cancer cells and mouse skeleton or adrenal gland and that EMT could be exploited as a potential target for the prevention and treatment of human prostate cancer metastases.

REFERENCES

1. Bavik C, Coleman I, Dean JP, Knudsen B, Plymate S, Nelson PS. The gene expression program of prostate fibroblast senescence modulates neoplastic epithelial cell proliferation through paracrine mechanisms. Cancer Res 2006;66(2):794–802.

2. Barrett JM, Mangold KA, Jilling T, Kaul KL. Bi-directional interactions of prostate cancer cells and bone marrow endothelial cells in three-dimensional culture. Prostate 2005;64(1):75–82.

3. Chung LW, Baseman A, Assikis V, Zhau HE. Molecular insights into prostate cancer progression: The missing link of tumor microenvironment. J Urol 2005;173(1):10–20.

4. Bova GS, Parmigiani G, Epstein JI, Wheeler T, Mucci NR, Rubin MA. Web-based tissue microarray image data analysis: Initial validation testing through prostate cancer Gleason grading. Hum Pathol 2001;32(4):417–427.

5. DeMarzo AM, Nelson WG, Isaacs WB, Epstein JI. Pathological and molecular aspects of prostate cancer. Lancet 2003;361(9361): 955–964.

6. Carter HB, Piantadosi S, Isaacs JT. Clinical evidence for and implications of the multistep development of prostate cancer. J Urol 1990;143(4):742–746.

7. De S, Chen J, Narizhneva NV, Heston W, Brainard J, Sage EH, Byzova TV. Molecular pathway for cancer metastasis to bone. J Biol Chem 2003;278(40):39044–39050.

8. Kasper S, Sheppard PC, Yan Y, Pettigrew N, Borowsky AD, Prins GS, Dodd JG, Duckworth ML, Matusik RJ. Development, progression, and androgen-dependence of prostate tumors in probasin-large T antigen transgenic mice: A model for prostate cancer. Lab Invest 1998;78(6):i–xv.

9. Greenberg NM. Androgens and growth factors in prostate cancer: A transgenic perspective. Prostate Cancer Prostatic Dis 2000;3(4):224–228.

10. Garabedian EM, Humphrey PA, Gordon JI. A transgenic mouse model of metastatic prostate cancer originating from neuroendocrine cells. Proc Natl Acad Sci USA 1998;95(26):15382–15387.

11. Yonou H, Yokose T, Kamijo T, Kanomata N, Hasebe T, Nagai K, Hatano T, Ogawa Y, Ochiai A. Establishment of a novel species- and tissue-specific metastasis model of human prostate cancer in humanized non-obese diabetic/severe combined immunodeficient mice engrafted with human adult lung and bone. Cancer Res 2001;61(5):2177–2182.

12. Wang Y, Xue H, Cutz JC, Bayani J, Mawji NR, Chen WG, Goetz LJ, Hayward SW, Sadar MD, Gilks CB, Gout PW, Squire JA, Cunha GR, Wang YZ. An orthotopic metastatic prostate cancer model in SCID mice via grafting of a transplantable human prostate tumor line. Lab Invest 2005;85(11):1392–1404.

13. Nemeth JA, Harb JF, Barroso U Jr, He Z, Grignon DJ, Cher ML. Severe combined immunodeficient-hu model of human prostate cancer metastasis to human bone. Cancer Res 1999;59(8):1987–1993.

14. Navone NM, Olive M, Ozen M, Davis R, Troncoso P, Tu SM, Johnston D, Pollack A, Pathak S, von Eschenbach AC, Logothetis CJ. Establishment of two human prostate cancer cell lines derived from a single bone metastasis. Clin Cancer Res 1997;3(12 Pt 1):2493–2500.

15. Wu TT, Sikes RA, Cui Q, Thalmann GN, Kao C, Murphy CF, Yang H, Zhau HE, Balian G, Chung LW. Establishing human prostate cancer cell xenografts in bone: Induction of osteoblastic reaction by prostate-specific antigen-producing tumors in athymic and SCID/bg mice using LNCaP and lineage-derived metastatic sublines. Int J Cancer 1998;77(6):887–894.

16. Zhau HY, Chang SM, Chen BQ, Wang Y, Zhang H, Kao C, Sang QA, Pathak SJ, Chung LW. Androgen-repressed phenotype in human prostate cancer. Proc Natl Acad Sci USA 1996;93(26): 15152–15157.

17. Wainstein MA, He F, Robinson D, Kung HJ, Schwartz S, Giaconia JM, Edgehouse NL, Pretlow TP, Bodner DR, Kursh ED. CWR22: Androgen-dependent xenograft model derived from a primary human prostatic carcinoma. Cancer Res 1994;54(23): 6049–6052.

18. Corey E, Quinn JE, Buhler KR, Nelson PS, Macoska JA, True LD, Vessella RL. LuCaP 35: A new model of prostate cancer progression to androgen independence. Prostate 2003;55(4): 239–246.

19. Carter BS, Beaty TH, Steinberg GD, Childs B, Walsh PC. Mendelian inheritance of familial prostate cancer. Proc Natl Acad Sci USA 1992;89(8):3367–3371.

20. Visakorpi T, Kallioniemi AH, Syvanen AC, Hyytinen ER, Karhu R, Tammela T, Isola JJ, Kallioniemi OP. Genetic changes in primary and recurrent prostate cancer by comparative genomic hybridization. Cancer Res 1995;55(2):342–347.

21. Gronberg H, Damber L, Damber JE. Studies of genetic factors in prostate cancer in a twin population. J Urol 1994;152(5 Pt 1): 1484–1487; discussion 1487–1489.

22. Sikes RA, Nicholson BE, Koeneman KS, Edlund NM, Bissonette EA, Bradley MJ, Thalmann GN, Cecchini MG, Pienta KJ, Chung LW. Cellular interactions in the tropism of prostate cancer to bone. Int J Cancer 2004;110(4):497–503.

23. Huang H, Muddiman DC, Tindall DJ. Androgens negatively regulate forkhead transcription factor FKHR (FOXO1) through a proteolytic mechanism in prostate cancer cells. J Biol Chem 2004; 279(14):13866–13877.

24. Wu YM, Robinson DR, Kung HJ. Signal pathways in up-regulation of chemokines by tyrosine kinase MER/NYK in prostate cancer cells. Cancer Res 2004;64(20):7311–7320.

25. Gleave M, Hsieh JT, Gao CA, von Eschenbach AC, Chung LW. Acceleration of human prostate cancer growth in vivo by factors produced by prostate and bone fibroblasts. Cancer Res 1991; 51(14):3753–3761.

26. Thalmann GN, Sikes RA, Wu TT, Degeorges A, Chang SM, Ozen M, Pathak S, Chung LW. LNCaP progression model of human prostate cancer: Androgen-independence and osseous metastasis. Prostate 2000;44(2):91–103 Jul 101;144(102).

27. Hoosein NM, Logothetis CJ, Chung LW. Differential effects of peptide hormones bombesin, vasoactive intestinal polypeptide and somatostatin analog RC-160 on the invasive capacity of human prostatic carcinoma cells. J Urol 1993;149(5):1209–1213.

28. Kariya Y, Miyazaki K. The basement membrane protein laminin-5 acts as a soluble cell motility factor. Exp Cell Res 2004;297(2): 508–520.

29. Huber MA, Kraut N, Beug H. Molecular requirements for epithelial-mesenchymal transition during tumor progression. Curr Opin Cell Biol 2005;17(5):548–558.

30. Thiery JP. Epithelial-mesenchymal transitions in development and pathologies. Curr Opin Cell Biol 2003;15(6):740–746.

31. Larue L, Bellacosa A. Epithelial-mesenchymal transition in development and cancer: Role of phosphatidylinositol 3′ kinase/AKT pathways. Oncogene 2005;24(50):7443–7454.

32. Cattan N, Rochet N, Mazeau C, Zanghellini E, Mari B, Chauzy C, Stora de Novion H, Amiel J, Lagrange JL, Rossi B, Gioanni J. Establishment of two new human bladder carcinoma cell lines, CAL 29 and CAL 185. Comparative study of cell scattering and

epithelial to mesenchyme transition induced by growth factors. Br J Cancer 2001;85(9):1412–1417.

33. Nawshad A, Lagamba D, Polad A, Hay ED. Transforming growth factor-beta signaling during epithelial-mesenchymal transformation: Implications for embryogenesis and tumor metastasis. Cells Tissues Organs 2005;179(1-2):11–23.

34. Han G, Lu SL, Li AG, He W, Corless CL, Kulesz-Martin M, Wang XJ. Distinct mechanisms of TGF-beta1-mediated epithelial-to-mesenchymal transition and metastasis during skin carcinogenesis. J Clin Invest 2005;115(7):1714–1723.

35. Kang Y, Massague J. Epithelial-mesenchymal transitions: Twist in development and metastasis. Cell 2004;118(3):277–279.

36. Aggarwal BB. Nuclear factor-kappaB: The enemy within. Cancer Cell 2004;6(3):203–208.

37. Kaplan RN, Riba RD, Zacharoulis S, Bramley AH, Vincent L, Costa C, MacDonald DD, Jin DK, Shido K, Kerns SA, Zhu Z, Hicklin D, Wu Y, Port JL, Altorki N, Port ER, Ruggero D, Shmelkov SV, Jensen KK, Rafii S, Lyden D. VEGFR1-positive haematopoietic bone marrow progenitors initiate the pre-metastatic niche. Nature 2005;438(7069):820–827.

38. Reya T, Clevers H. Wnt signalling in stem cells and cancer. Nature 2005;434(7035):843–850.

39. Thalmann GN, Anezinis PE, Chang SM, Zhau HE, Kim EE, Hopwood VL, Pathak S, von Eschenbach AC, Chung LW. Androgen-independent cancer progression and bone metastasis in the LNCaP model of human prostate cancer. Cancer Res 1994; 54(10):2577–2581.

40. Rhee HW, Zhau HE, Pathak S, Multani AS, Pennanen S, Visakorpi T, Chung LW. Permanent phenotypic and genotypic changes of prostate cancer cells cultured in a three-dimensional rotating-wall vessel. In Vitro Cell Dev Biol Anim 2001;37(3):127–140.

41. Sramkoski RM, Pretlow TG 2nd, Giaconia JM, Pretlow TP, Schwartz S, Sy MS, Marengo SR, Rhim JS, Zhang D, Jacobberger JW. A new human prostate carcinoma cell line, 22Rv1. In Vitro Cell Dev Biol Anim 1999;35(7):403–409.

42. Pettaway CA, Pathak S, Greene G, Ramirez E, Wilson MR, Killion JJ, Fidler IJ. Selection of highly metastatic variants of different human prostatic carcinomas using orthotopic implantation in nude mice. Clin Cancer Res 1996;2(9):1627–1636.

43. Klein KA, Reiter RE, Redula J, Moradi H, Zhu XL, Brothman AR, Lamb DJ, Marcelli M, Belldegrun A, Witte ON, Sawyers CL. Progression of metastatic human prostate cancer to androgen independence in immunodeficient SCID mice. Nat Med 1997; 3(4):402–408.

44. Bates AW, Baithun SI. Secondary solid neoplasms of the prostate: A clinico-pathological series of 51 cases. Virchows Arch 2002;440(4):392–396.

45. Nelson JB, Nabulsi AA, Vogelzang NJ, Breul J, Zonnenberg BA, Daliani DD, Schulman CC, Carducci MA. Suppression of prostate cancer induced bone remodeling by the endothelin receptor A antagonist atrasentan. J Urol 2003;169(3):1143–1149.

46. Smith MR. Zoledronic acid to prevent skeletal complications in cancer: Corroborating the evidence. Cancer Treat Rev 2005; 31(Suppl 3):19–25.

47. Wu JD, Odman A, Higgins LM, Haugk K, Vessella R, Ludwig DL, Plymate SR. In vivo effects of the human type I insulin-like growth factor receptor antibody A12 on androgen-dependent and androgen-independent xenograft human prostate tumors. Clin Cancer Res 2005;11(8):3065–3074.

48. Longoria RL, Cox MC, Figg WD. Antiangiogenesis: A possible treatment option for prostate cancer? Clin Genitourin Cancer 2005;4(3):197–202.

49. Tu SM, Millikan RE, Mengistu B, Delpassand ES, Amato RJ, Pagliaro LC, Daliani D, Papandreou CN, Smith TL, Kim J, Podoloff DA, Logothetis CJ. Bone-targeted therapy for advanced androgen-independent carcinoma of the prostate: A randomised phase II trial. Lancet 2001;357(9253):336–341.

12

Quantum Dots for In Vivo Molecular and Cellular Imaging

Xiaohu Gao, Leland W. K. Chung, and Shuming Nie

Summary

Multifunctional nanoparticle probes based on semiconductor quantum dots (QDs) are developed for simultaneous targeting and imaging of cancer cells in living animals. The structural design involves encapsulating luminescent QDs with an ABC triblock copolymer, and linking this polymer to tumor-targeting ligands, such as antibodies and drug-delivery functionalities. In vivo targeting studies of human prostate cancer growing in nude mouse show that the QD probes can be delivered to tumor sites by both enhanced permeation and retention (passive targeting) and by antibody binding to cancer-specific cell surface biomarkers such as prostate-specific membrane antigen (active targeting). Using both subcutaneous injection of QD-tagged cancer cells and the systemic injection of multifunctional QD probes, multicolor fluorescence imaging of as few as 10–100 cancer cells can be achieved under in vivo conditions. The use of spectrally resolved imaging can efficiently remove autofluorescence background and precisely delineate weak spectral signatures in vivo. These results suggest that QD probes and spectral imaging can be combined for multiplexed imaging and detection of genes, proteins, and small-molecule drugs in single living cells, and that this imaging modality can be adopted for real-time visualization of cancer cell metastasis in live animals.

Key Words: Quantum dots; nanoparticles; in vivo; molecular; cellular; imaging; targeting; diagnosis; spectral; multiplexed; multifunctional; block copolymer.

1. Introduction

The development of high-sensitivity and high-specificity probes beyond the intrinsic limitations of organic dyes and fluorescent proteins is of considerable interest to many areas of research, ranging from molecular and cellular biology to molecular imaging and medical diagnostics. Recent advances have shown that nanometer-sized semiconductor particles can be covalently linked with

biorecognition molecules such as peptides, antibodies, nucleic acids, and small-molecule inhibitors for applications as fluorescent probes *(1–13)*. In comparison with organic fluorophores, these quantum-confined particles or quantum dots (QDs) exhibit unique optical and electronic properties, such as size- and composition-tunable fluorescence emission from visible-to-infrared wavelengths, extremely large absorption coefficients across a wide spectral range, and very high levels of brightness and photostability *(14,15)*. Despite their relatively large sizes (2–8 nm), recent research has shown that bioconjugated QD probes behave like genetically encoded fluorescent proteins (4–6 nm), and do not suffer from serious kinetic binding or steric-hindrance problems *(6–13)*. In this "mesoscopic" size range, QDs also have more surface areas and functionalities that can be used for linking to multiple diagnostic (e.g., radioisotopic or magnetic) and therapeutic (e.g., anticancer) agents. These properties have opened new possibilities for ultrasensitive bioassays and diagnostics, as well as for advanced molecular and cellular imaging.

Here, we report detailed protocols of preparing bioconjugated QD probes for simultaneous targeting and imaging of human prostate cancer cells in a murine model. Key steps involves high-quality QD preparation, surface coating with amphiphilic triblock copolymer for in vivo protection, bioconjugation of multiple polyethylene glycols (PEGs) and targeting ligands for tumor antigen recognition, and in vivo fluorescence imaging. To enhance the detection sensitivity, we further discuss the use of hyperspectral imaging configuration to separate QD fluorescence from strong background (mouse skin autofluorescence).

2. Materials

1. 90% Technical grade trioctylphosphine oxide (TOPO) (Aldrich).
2. 99% Pure trioctylphosphine (Aldrich).
3. Cadmium oxide (CdO 99.99%) (Aldrich).
4. Selenium (>99%) (Riedel-de Haën).
5. 99% Stearic acid (Sigma).
6. Hexamethlydisilathiane (Fluka).
7. Dimethylzinc (10% wt in hexane, store and use in inert atmosphere) (Strem).
8. 98% Hexadecylamine (Aldrich).
9. Poly(t-butyl acrylate-co-ethyl acrylate-co-methacrylic acid) (PBEM, mw. 100K) (Aldrich).
10. 99% Octylamine (Fluka).
11. *N*-(3-dimethylaminopropyl)-*N*′-ethylcarbodiimide hydrochloride (EDAC) (Fluka).
12. PEG (mw. 2-5K) (Nektar and Sunbio).
13. 98% 2,2′-(Ethylenedioxy)diethylamine (Aldrich).
14. Antibody J591 against prostate-specific membrane antigen (PSMA) (Millennium Pharmaceuticals).
15. Separation media, Sephadex G-25, Superdex 75, and Superdex 200 (Amersham).

16. Ketamine and Xylazine (Prescription drugs from local hospital).
17. Ultracentrifuge, Optima TLX (Beckman Coulter).
18. 1-cc Insulin syringe (29X1/2 gauge) for intravenous injection (VWR).
19. 6–8-wk nude mice (Charles River).
20. Specialized imaging equipment is discussed in the main text.

3. Methods

3.1. Preparation of Highly Fluorescent QDs

High-quality red-color QDs are prepared according to literature procedures with modifications *(16–20)*. The 0.128 g CdO (1 mmol) precursor is first dissolved in 1 g stearic acid with heating in a three-neck round-bottom flask. After formation of a clear solution, TOPO (5 g) and hexadecylamine (5 g) are added as reaction solvents, which are then heated to 250°C under argon for 10 min. The temperature is briefly raised to 360°C, and equal molar selenium dissolved in trioctylphosphine is quickly injected into the hot solvents. The mixture immediately changes color to orange-red, indicating QD formation. The dots are kept in the reaction solvents at 200°C for 30 min, and capping solution of dimethylzinc (0.5 mmol) and hexamethyldisilathiane (0.5 mmol) is slowly added over a period of 15 min to protect the CdSe core. These ZnS-capped CdSe dots have excellent chemical- and photostability. The dots are cooled to room temperature, and are rinsed repeatedly with methanol/hexane to remove free ligands. Ultraviolet adsorption, fluorescence emission spectra, and transmission electron microscopy are used for characterization. This procedure typically produces QDs with emission peak centered at 630–640 nm, close to the upper wavelength limit of high-quality CdSe dots. However, the deep-red color is not optimized for tissue penetration and imaging sensitivity in animals. Deep tissue imaging (millimeters to centimeters) requires the use of near-infrared light in the spectral range of 700 to 900 nm *(21)*, (*see* **Note 1**). Nevertheless, the imaging concept and probe preparation techniques are essentially the same.

3.2. Nanoparticle Surface Modification and Bioconjugation

3.2.1. Polymer Modification

For encapsulating QDs, about 25% of the free carboxylic acid groups in PBEM triblock copolymer are derivatized with octylamine, a hydrophobic side chain (*see* **Note 2**). Thus, the original polymer (0.1 g) dissolved in 4 mL dimethylformamide is reacted with *n*-octylamine (5.2 mg) using ethyl-3-dimethyl amino propyl carbodiimide (EDAC, 23 mg, threefold excess of *n*-octylamine), as a crosslinking reagent. The product yields are generally greater than 90% because of the high EDAC-coupling efficiency in dimethylformamide (determined by a change of the free octylamine band in thin-layer chromatography). The reaction mixture is

dried with a rotary evaporator (Rotavapor R-3000, Buchi Analytical Inc., DE). The resulting oily liquid is precipitated and rinsed five times with water to remove excess EDAC and other water-soluble byproducts. After vacuum-drying, the octylamine-grafted polymer is stored or resuspended in an ethanol/chloroform mixture for use.

Au: Please specify where "below" with a sub-heading number.

3.2.2. Particle Encapsulation

TOPO-capped purified QDs (0.1 nmol) are mixed with the polymer (*see* below) in a chloroform/ethanol solvent mixture (3:1 [v/v]). The nanoparticle suspension is then placed in vacuum and slowly dried over a time course of 2–6 h for particle–polymer self-assembly. The polymer-to-QD molar ratio is set at 5–20 depending on the particle sizes (for the red QDs used here, the ratio is set at 20), and the polymers in excess are removed later. After vacuum-drying, the encapsulated dots are soluble in many polar solvents, such as aqueous buffer (pH >9.0) and alcohols. The nanoparticle–polymer hybrids are kept in aqueous solution for 3 d and then purified from unbound polymers by gel filtration (Superdex 200) (sample loading volume <5% of the column volume). Alternatively, ultracentrifuge and ultrafiltration work equally well. Dynamic light scattering measurements show a particle size around 10 nm (number weighted), which is much smaller than nanoparticles coated with the original unmodified PBEM polymer (40 nm). This comparison indicates the formation of a tight polymer wrapping layer on QD surface.

3.2.3. Long-Circulating PEG-Modified QD

Polymer-coated QDs are activated with 50 m*M* EDAC in phosphate-buffered saline (PBS) and reacted with amino-mPEG (mw 5000) at a QD/PEG molar ratio of 1:50 overnight at pH 8.5 (pH adjusted by NaOH). The QDs saturated with PEG chains can be purified by three methods, column filtration (Superdex 75), dialysis (mwco >3X of the mw of PEG), or ultracentrifugation at 75,000*g* for 60 min. After resuspension in PBS buffer (pH 7.4), trace amount of aggregated particles were removed by centrifugation at 6000*g* for 10 min. The resulted QDs not only have a long plasma circulation time but are also highly stable in a broad range of aqueous conditions (e.g., pH 1.0 to 14.0 and salt concentration 0.01 to 1 *M*).

Au: Please spell out mwco

3.2.4. QD–Antibody Probe

We have developed two coupling procedures based on carbodiimide-mediated amide formation and amine-sulfhydryl crosslinking *(22)*. For carbodiimide reactions, the polymer-coated dots (COOH functional groups) are activated with 1 m*M* EDAC for 10 min and then mixed with amino-mPEG at a QD/PEG ratio of 1:6. After a quick purification with polyacrylamide-desalting

columns (Pierce), the activated dots are reacted with an IgG antibody at a QD/antibody molar ratio of 1:15 for 2 h. The final QD bioconjugates are purified by filtration column chromatography (Amersham). After dilution in PBS buffer, aggregated particles are removed by centrifugation at 6000g for 10 min, and the QD–antibody bioconjugates are kept at 4°C. This procedure is easy to perform and broadly applicable for many native proteins, such as IgG, streptavidin, lectins, peptides, and so on because the availability of amine groups (**Note 3**). On the other hand, however, the abundant reactive groups could cause aggregation and render biomolecules randomly oriented on the QD surface, which is detrimental to antibody activities. The second procedure using active ester–maleimide crosslinker solves the probe-orientation problem but involves pretreatments of nanoparticles and antibodies. In this approach, polymer-coated nanoparticles are first reacted with 2,2′-(ethylenedioxy) diethylamine to add a small number of amino groups and is purified with a G25 desalting column. In the mean time, purified IgG molecules are reduced by dithiothreitol to cleave the disulfide bonds in the hinge region. Similar and very detailed procedures are available at Quantum Dot Corporation's website. It has been our experiences that this antibody fragment conjugation leads to less aggregation and bioactivity retardation. Although the binding affinity of each antibody fragment to its target molecules decreases, it could be compensated by a multivalence effect (multiple fragments per QD because of its large surface area), and this matter deserves careful examination. For some applications where the whole antibody is critical for specific molecular recognition, we are developing a new conjugation chemistry based on hydrazide coupling, which not only allows the use of whole IgG, but also controls the IgG orientation. Preliminary studies have shown improved results in multicolor molecular mapping of formalin-fixed, paraffin-embedded tissue specimens.

Au: DTT correctly defined as dithiothreitol?

3.3. In Vitro Cellular Imaging and Spectroscopy

PSMA-positive C4-2 cells and PSMA-negative PC-3 cells are cultured 2–3 d on chamber slides. For live cell staining, no blocking step is needed. QD–PSMA or QD–PEG bioconjugates are diluted to 50 nM in PBS or Hank's balanced buffers, and incubated (100 μL) with the cultured cells for 1 h at 4°C. The stained cells are then gently washed with PBS for three times and photographed on an inverted fluorescence microscope (Olympus, IX-70) equipped with a digital color camera (Nikon D1), a broad-band blue light source (480/40 nm, 100-W mercury lamp), and a long-pass interference filter (DM 510, Chroma Tech, Brattleboro, VT). Single cell fluorescence intensity is quantified with flow cytometer (FACS) or wavelength-resolved, single-stage spectrometer (SpectraPro 150, Roper Scientific, Trenton, NJ; detailed instrument setup is described in an early volume of this book series) *(23)*.

140   *Gao, Chung, and Nie*

3.4. In Vivo Animal Imaging

3.4.1. Animal Preparation and Processing

All the protocols described next have been examined and approved by the Institutional Animal Care and Use Committee of Emory University. C4-2 prostate tumor cells are cultured 2–3 d and injected into 6–8 wk nude mice subcutaneously (10^6 cells/injection site). Tumor growth should be monitored daily until it reaches the desired sizes using caliper measurements. (For C4-2 cell line, spontaneous tumor growth varies among different animals. Therefore, each mouse is implanted with tumor cells at multiple sites.) The mice are divided into three groups for passive, active targeting, and control studies. They are then placed under anesthesia by injection of a ketamine and xylazine mixture intraperitioneally at a dosage of 95 mg/kg and 5 mg/kg, respectively. QD bioconjugates are injected through the tail vein at 0.4 nmol per mouse for active targeting, or 6.0 nmol for passive targeting and control experiment using 29X1/2-gage insulin syringes. After imaging studies, the mice are sacrificed by CO_2 overdose. Tumor and major organs (brain, heart, kidney, liver, lung, muscle, and spleen) were removed and frozen for histology examination. Tissue collections were cryosectioned into 5- to 10-µm thickness sections, fixed with acetone at 0°C, and imaged on the inverted fluorescence microscope.

3.4.2. Tumor Imaging Strategies

Bioconjugated QDs are delivered to the tumor sites by both passive and active tumor-targeting mechanisms (**Fig. 1**) *(24)*. In the passive mode, PEG-coated long-circulating QDs are accumulated preferentially at tumor sites through an enhanced permeability and retention effect; whereas in the active mode, QDs linked with targeting molecules such as antibody, peptide, antagonist, and so on quickly mark tumors through molecular recognition (in this report, QD-PSMA bioconjugate specifically bind to prostate tumors). It is worth mentioning that dextran is another attractive cloaking molecular for enhancement of nanoparticle biocompatibility and plasma circulation time.

3.4.3. Fluorescence Imaging

In vivo fluorescence imaging is performed by using a macro-illumination system (Lightools Research, Encinitas, CA), designed specifically for small animal studies. As shown in **Fig. 2**, in a dark box illumination is provided by fiberoptic lighting (lamp house outside the dark box). For true-color fluorescence imaging, a long-pass dielectric filter (Chroma Technology) is used to reject scattered excitation light and to pass Stokes-shifted QD fluorescence. The fluorescence image is captured by a color charge-coupled device (Optronics, Magnafire SP, Olympus, America) and can be monitored on a computer screen
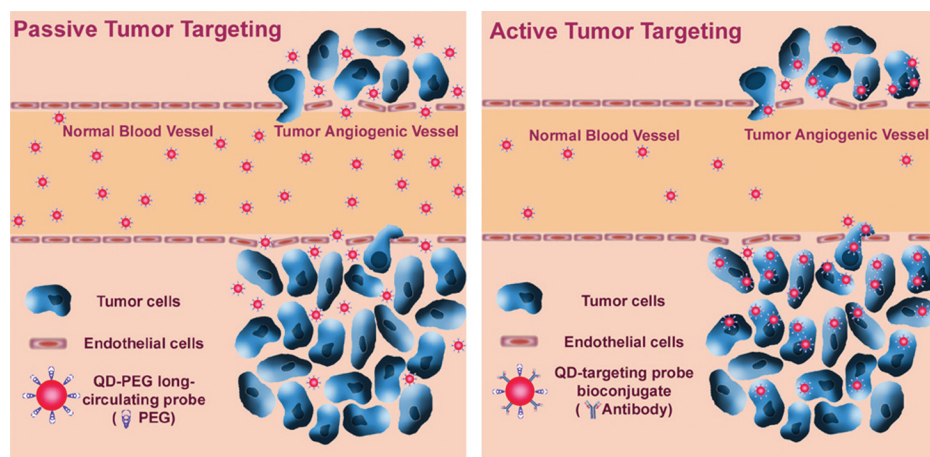
Fig. 1. In vivo tumor-targeting strategies. Passive tumor targeting based on permeation and retention of long-circulating quantum dot (QD) probes via leaky tumor vasculatures (left panel), and active tumor targeting based on high binding affinity of QD–antibody conjugates to tumor antigens (right panel).
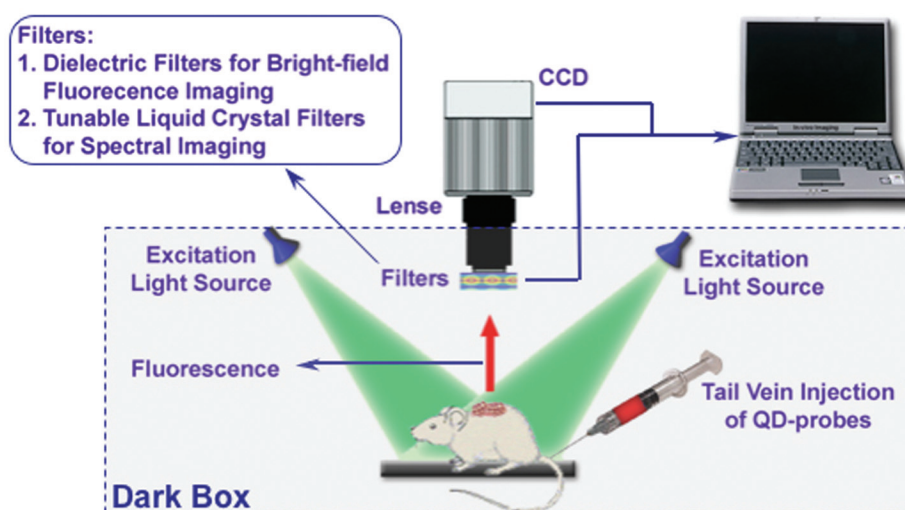

Fig. 2. Schematic illustration of in vivo optical imaging instrumentation. Tumor-bearing mice are administered with quantum dot bioconjugates intravenously and placed under anesthesia. In a dark box, illumination is provided by fiber-optic lighting. A long- pass filter is used to block the scattered lights, and a computer-controlled liquid crystal tunable filter is exploited for multispectral imaging.

in real time. For wavelength-resolved hyper spectral imaging, a cooled, scientific-grade monochrome charge-coupled device camera is used together with a spectral imaging optical head (with a built-in liquid crystal tunable filter scanning from 400 to 720 nm, CRI, Inc., Woburn, MA). Because the red QDs used in this work has an emission wavelength centered at 640 nm, the tunable filter is set to automatically step in 10-nm increments from 580 to 700 nm (*see* **Note 4**). The camera capture images at each wavelength with constant exposure, resulting in 13 TIFF images loaded into a single data structure. Based on the fluorescence spectra of pure QDs and autofluorescence, the spectral-imaging software can quickly analyze the spectral components for each pixel via a process known as "principle component analysis" *(25)*. The whole process takes less than 1 s and can be output into separate fluorescence channels or overlaid images, as shown in **Fig. 3**. It should be pointed out that the autofluorescence and QD spectra need only be recorded initially, as they can be saved in spectral libraries and reused on additional spectral unmixing.

Fig. 3

4. Notes

1. This wavelength range provides a "clear" window for in vivo optical imaging because it is separated from the major absorption peaks of blood and water. Toward this goal, recent research has prepared alloyed semiconductor QD consisting of cadmium selenium telluride, with tunable fluorescence emission up to 850 nm *(26)*. Technical optimization of this new material together with core-shell CdTe/CdSe type-II QDs *(27)* are still needed to improve the stability and quantum efficiency. A number of promising approaches have been recently discovered. For example, Peng et al. have reported the use of successive ion layer adsorption and reaction method (originally developed for thin film deposition on solid substrates) to precisely control nanoparticle growth one layer at a time *(28)*; while Han and coworkers improved the ternary QD (three-component) synthesis by alloying the third component into preformed binary QDs *(29)*. Together with other possibilities, high-quality NIR QDs should be available very soon and bring major improvements in tissue penetration depth and cell detection sensitivity. It is worth mentioning that in vivo detection sensitivity can be further enhanced by fluorescence tomography imaging based on multiple light sources and detectors *(30)*.

2. Unmodified block copolymer can also solubilize QDs into aqueous solution, but can result in a relatively thick surface-coating layer, similar to PEG–lipid micelles *(6)*. This is because the hydrophilic methacrylic acid block doesn't have enough affinity to the particle surface and dangles in solution, which is supported by dynamic light-scattering measurements.

3. For in vivo targeting and imaging, it is advantageous to use short peptides with high binding affinity and specificity than antibodies, because of their smaller size, less immune response, lower cost, and easiness in bioconjugation. Furthermore, automated peptide synthesis and recent advance in phage display *(31)* technique enable researchers to screen and engineer peptide sequences at a relatively high throughput.

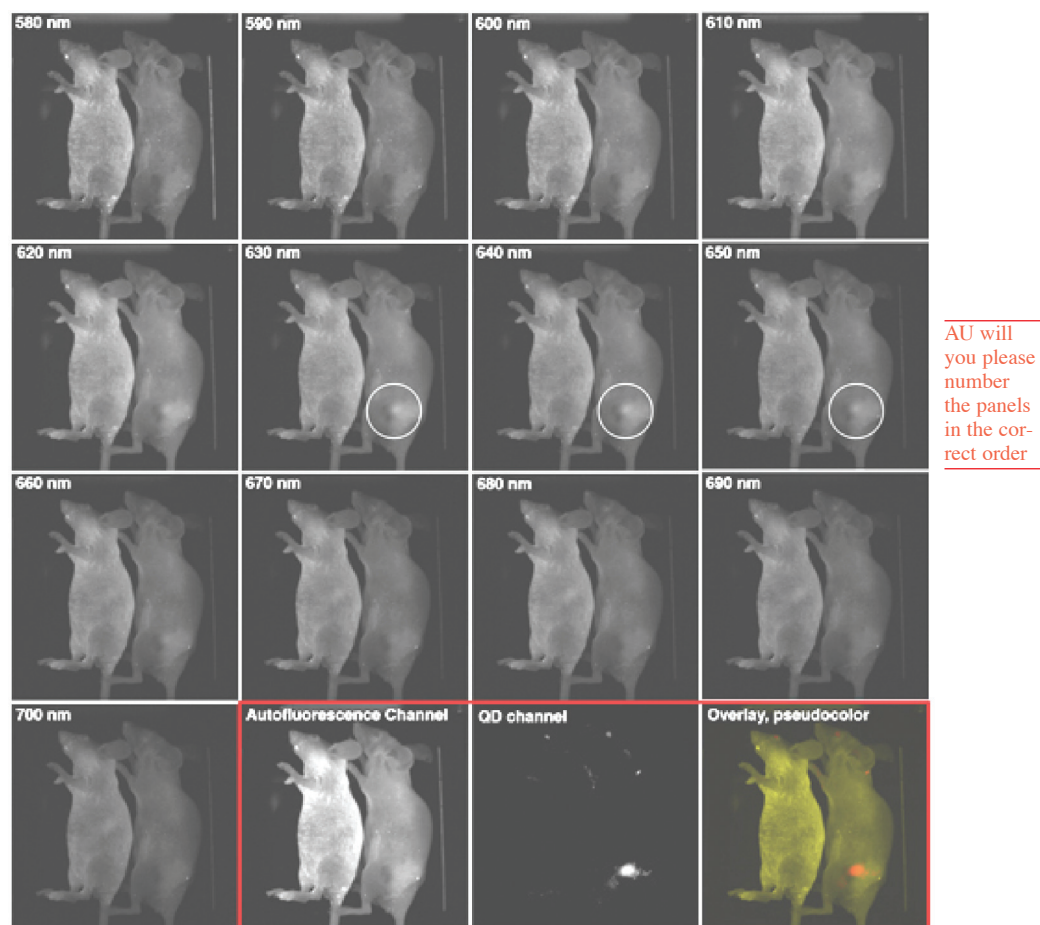*In Vivo Molecular and Cellular Imaging*   143

Fig. 3. Spectral imaging of quantum dot (QD)–prostate-specific membrane antigen antibody conjugates in live mice harboring C4-2 tumor xenografts. Panels 1–13, experimental raw data of an image stack from 580 to 700 nm. Please note the fluorescence intensity increase at the tumor site (white circle) from wavelength 630–650 nm, because of accumulation of red-color QDs (emission peak at 640 nm). Panels 14–16, spectrally deconvoluted images (in red square). Based on spectral distinction between mouse skin and QD emissions, fluorescent images can be output into autofluorescence and QD channels separately, or as an overlaid picture.

4. For complicated spectral deconvolution (e.g., more spectral components, similar spectra among different components, irregular spectra such as spikes, and so on), the tunable liquid crystal filter should be set to step in smaller wavelength increments, such as 1 or 5 nm. As a tradeoff of the high unmixing resolution, the imaging and computing time also increase.

Acknowledgments

References

1. Chan, W. C. W., Maxwell, D. J., Gao, X. H., Bailey, R. E., Han, M. Y., and Nie, S. M. (2002) Luminescent QDs for multiplexed biological detection and imaging. *Curr. Opin. Biotechnol*. **13,** 40–46.
2. Bruchez, M., Jr., Moronne, M., Gin, P., Weiss, S., and Alivisatos, A. P. (1998) Semiconductor nanocrystals as fluorescent biological labels. *Science* **281,** 2013–2015.
3. Chan, W. C. W. and Nie, S. M. (1998) Quantum dot bioconjugates for ultrasensitive nonisotopic detection. *Science* **281,** 2016–2018.
4. Mattoussi, H., Mauro, J. M., Goldman, E. R., et al. (2000) Self-assembly of CdSe–ZnS QDs bioconjugates using an engineered recombinant protein. *J. Am. Chem. Soc*. **122,** 12,142–12,150.
5. Akerman, M. E., Chan, W. C. W., Laakkonen, P., Bhatia, S. N., and Ruoslahti, E. (2002) Nanocrystal targeting in vivo. *Proc. Natl. Acad. Sci. USA* **99,** 12,617–12,621.
6. Dubertret, B., Skourides, P., Norris, D. J., Noireaux, V., Brivanlou, A. H., and Libchaber, A. (2002) In vivo imaging of QDs encapsulated in phospholipid micelles. *Science* **298,** 1759–1762.
7. Wu, X., Liu, H., Liu, J., et al. (2003) Immunofluorescent labeling of cancer marker Her2 and other cellular targets with semiconductor QDs. *Nat. Biotechnol*. **21,** 41–46.
8. Jaiswal, J. K., Mattoussi, H., Mauro, J. M., and Simon, S. M. (2003) Long-term multiple color imaging of live cells using quantum dot bioconjugates. *Nat. Biotechnol*. **21,** 47–51.
9. Larson, D. R., Zipfel, W. R., Williams, R. M., et al. (2003) Water-soluble quantum dots for multiphoton fluorescence imaging in vivo. *Science* **300,** 1434–1436.
10. Ishii, D., Kinbara, K., Ishida, Y., et al. (2003) Chaperonin-mediated stabilization and ATP-triggered release of semiconductor nanoparticles. *Nature* **423,** 628–632.
11. Medintz, I. L., Clapp, A. R., Mattoussi, H., Goldman, E. R, Fisher, B., and Mauro, J. M. (2003) Self-assembled nanoscale biosensors based on quantum dot FRET donors. *Nat. Mater.* **2,** 630–639.
12. Dahan, M., Levi, S., Luccardini, C., Rostaing, P., Riveau, B., and Triller, A. (2003) Diffusion dynamics of glycine receptors revealed by single–quantum dot tracking. *Science* **302,** 441–445.
13. Rosenthal, S. J., Tomlinson, I., Adkins, E. M., et al. (2002)Targeting cell surface receptors with ligand-conjugated nanocrystals. *J. Am. Chem. Soc*. **124,** 4586–4594.
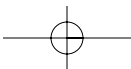
Uncorrected Proof Copy

14. Niemeyer, C. M. (2001) Nanoparticles, proteins, and nucleic acids: biotechnology meets materials science. *Angew. Chem. Int. Ed*. **40,** 4128–4158.

15. Alivisatos, A. P. (1996) Semiconductor clusters, nanocrystals, and quantum dots. *Science* **271,** 933–937.

16. Murray, C. B., Norris, D. J., and Bawendi, M. G. (1993) Synthesis and characterization of nearly monodisperse CdE (E = S, Se, Te) semiconductor nanocrystallites. *J. Am. Chem. Soc*. **115,** 8706–8715.

17. Hines, M. A. and Guyot-Sionnest, P. (1996) Synthesis of strongly luminescing ZnS-capped CdSe nanocrystals. *J. Phys. Chem. B* **100,** 468–471.

18. Peng, X. G., Schlamp, M. C., Kadavanich, A. V., and Alivisatos, A. P. (1997) Epitaxial growth of highly luminescent CdSe/CdS core/shell nanocrystals with photostability and electronic accessibility. *J. Am. Chem. Soc*. **119,** 7019–7029.

19. Peng, Z. A. and Peng, X. G. (2001) Formation of high-quality CdTe, CdSe, and CdS nanocrystals using CdO as precursor. *J. Am. Chem. Soc*. **123,** 183–184.

20. Qu, L., Peng, Z. A., and Peng, X. (2001) Alternative routes toward high quality CdSe nanocrystals. *Nano Lett*. **1,** 333–337.

21. Weissleder, R. (2001) A clearer vision for in vivo imaging. *Nat. Biotechnol*. **19,** 316–317.

22. Gao, X. H., Yang, L., Petros, J. A., Marshall, F. F., Simons J. W., and Nie, S. M. (2005) In vivo molecular and cellular imaging with quantum dots. *Curr. Opin. Biotech*. **16,** 63–72.

23. Gao, X. H. and Nie, S. M. (2004) Quantum dot-encoded beads. In: *NanoBiotechnology Protocols*, (Rosenthal, S. J. and Wright, D. W., eds.), Humana, Totowa, NJ.

24. Gao, X. H., Cui, Y. Y., Levenson, R. M., Chung, L. W. K., and Nie, S. M. (2004) In vivo cancer targeting and imaging with semiconductor quantum dots. *Nat. Biotechnol*. **22,** 969–976.

25. Levenson, R. M. and Hoyt, C. C. (2002) Spectral imaging in microscopy. *American Laboratory*, 26–33.

26. Bailey, R. E. and Nie, S. M. (2003) Alloyed semiconductor quantum dots: tuning the optical properties without changing the particle size. *J. Am. Chem. Soc*. **125,** 7100–7106.

27. Kim, S., Fisher, B., Eisler, H. J., and Bawendi, M. (2003) Type-II quantum dots: CdTe/CdSe(core/shell) and CdSe/ZinTe(core/shell) heterostructures. *J. Am. Chem. Soc*. **125,** 11,466–11,467.

28. Li, J. J., Wang Y. A., Guo, W. Z., et al. (2003) Large-scale synthesis of nearly monodisperse CdSe/CdS core/shell nanocrystals using air-stable reagents via successive ion layer adsorption and reaction. *J. Am. Chem. Soc*. **125,** 12,567–12,575.

29. Zhong, X. H., Han, M. Y., Dong, Z. L., White, T. J., and Knoll, W. (2003) Composition-tunable ZnxCd1-xSe nanocrystals with high luminescence and stability. *J. Am. Chem. Soc*. **125,** 8589–8594.

30. Ntziachristos, V., Tung, C. H., Bremer, C., and Weissleder, R. (2002) Fluorescence molecular tomography resolves protease activity in vivo. *Nat. Med*. **8,** 757–761.

31. Arap, W., Pasqualini, R., and Ruoslahti, E. (1998) Cancer treatment by targeted drug delivery to tumor vasculature. *Science* **279,** 377–380.

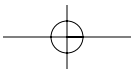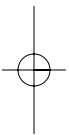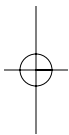Au: Please provide page range for chapter in ref. 23

Au: Please provide volume number for ref. 25

Stromal-Epithelial Interaction in Prostate Cancer Progression

Leland W. K. Chung, Wen-Chin Huang, Shian-Ying Sung, Daqing Wu, Valerie Odero-Marah, Takeo Nomura, Katsumi Shigemura, Tohru Miyagi, Seogil Seo, Chumeng Shi, Joe Molitierno, James Elmore, Cynthia Anderson, Shuji Isotani, Magnus Edlund, Chia-Ling Hsieh, Ruoxiang Wang, Bahig Shehata, Haiyen E. Zhau

Molecular Urology and Therapeutics Program, Department of Urology and Winship Cancer Institute, Emory University School of Medicine, Atlanta, GA

Address for correspondence:
Leland W. K. Chung, MD
Department of Urology, Winship Cancer Institute
Emory University School of Medicine
1365 Clifton Rd NE, Suite B 4100, Atlanta, GA 30322
Fax: 404-778-3675
E-mail: lwchung@emory.edu

Abstract

Cancer is not a single-cell disease, and its existence and behavior are constantly modulated by the host. Cancer gene expression and genetics are also highly dynamic and are regulated epigenetically by the host through gene-environment interaction. In this article, we describe the molecular pathways leading to an unusual property of cancer cells: the ability to mimic the host microenvironment and, in particular, the characteristics of osteomimicry and vasculogenic mimicry, which are likely to be regulated by soluble and insoluble factors in the tumor-adjacent microenvironment. We also discuss the importance of host inflammatory and stem cells that contribute to the growth and survival of cancer cells. By understanding the salient features of cancer-host interaction, novel therapeutics might be developed to target the cancer and its host in the treatment of lethal prostate cancer metastases.

Introduction

It is now well accepted that cancer progression depends not only on the genetic constituents and modifications of the cancer cells but also on the genetics and epigenetic factors contributed by the host.[1-5] Although genetic changes in cancer cells are required for cancer to occur, these changes are insufficient to induce the entire spectrum of a progressive cancer.[6,7] It has been amply demonstrated that intimate interaction between cancer cells and their host microenvironment greatly influences the growth and subsequent dissemination of cancer cells.[8-11] The work of Paget more than 100 years ago epitomizes the tumor ("seed") and host ("soil") relationship that determines the patterns of cancer dissemination in patients.[12] Recent work, however, showed that this interaction is far more dynamic than previously thought, including the ability of the host to alter the genetics and the behaviors of cancer cells and the ability of cancer cells to reciprocally modify the genetics and the inductive potential of the host.[5,13-16] Host cells are not static but can be recruited to or modified at the site of cancer cell growth and metastasis and greatly influence the behaviors of cancer cells.[5,13,17] The homeostasis between cancer cells and their immediate microenvironment, including inflammatory cells and bone marrow–derived stem cells recruited to sites of cancer growth and metastasis, the levels of hypoxia and circulating hormones surrounding the cancer cells and the stress conditions, reactive oxygen species (ROS) induced by cell crowding and changing pH, and the osmolarity of the tumor-adjacent microenvironment, are all known to contribute to changing cancer behaviors.[18-21] Through constant contact and interaction with the rich milieu of the microenvironment, including soluble growth factors, extracellular matrices, and ROS, cancer cells gain additional genetic modifications and behavioral changes that drive them to migrate and invade. Ultimately, the host factors determine the patterns of cancer cell dissemination.[10,12,22-24]

This review focuses on the contribution of host stromal fibroblasts and osteoblasts to local cancer growth, progression, and final metastasis to the skeleton and visceral organs. The converging signaling pathways that

respond to factors that confer growth and lead to the survival and metastasis of cancer cells and the therapeutic opportunities arising from this paradigm shift will be emphasized. Specifically, the following topics and molecular events will be reviewed and discussed: the plasticity of cancer and stromal fibroblasts that together contribute to cancer growth and progression; the molecular basis of mimicry by cancer cells, with gene expression and cellular functions guided by the host/cancer microenvironment and vascular endothelial and osteoblastic cells that support the growth and survival of cancer cells; how cancer cells orchestrate gene expression profile changes of the host cells that together participate in the genesis and progression of cancer; and the opportunity for therapeutic co-targeting of the cancer and the tumor microenvironment, disrupting the evolutionary continuum of the cancer and stromal cells that leads to the uncontrolled growth of cancer cells and their resistance to therapy.

Plasticity of Cancer and Stromal Fibroblasts

The developmental fate of a normal cell is regulated temporally and spatially by precise inductive cues from the cell microenvironment.[25] In response to the signaling molecules, the gene expression profiles and the behaviors of a normal differentiating cell are subjected to changes allowing the execution of normal differentiation program of a developing organ to result. The genomic stability of the normal cell in this case is desired, expected, and essential for the preservation of the genetic makeup and survival of the normal cells.[26] However, in the case of cancer, many of the physiologic processes are "hijacked" by cancer cells, and mechanisms controlling growth and survival in the normal physiologic context are lost.[27-29] The plasticity of cancer cells and stromal fibroblasts could fuel tumor growth through the production of excessive amounts of angiogenic substances leading to the ingrowth of new blood vessels, mimicking the normal physiologic processes of wound repair.[30,31] Cancer cells have been described as a wound that fails to heal. This refers to the persistent stromal response to the invading cancer epithelium and the secreted local factors, such as plasminogen activator, that prevented the blood clotting and wound-healing processes.[32,33] Cancer cells can be immune-evasive "outlaws" that have lost the major histocompatibility class 1 antigen and are no longer recognized by the host cytotoxic T cells.[34] Cancer cells overcome and resist the physiologically programmed apoptotic response to the developmental signals, tissue injuries, and stress responses induced by hypoxia, hormone withdrawal, chemotherapy, and radiation therapy through a variety of mechanisms related to imbalanced proliferative and apoptotic programs.[35,36]

The prostate gland is derived from the embryonic urogenital sinus, with the growth and differentiation of the glandular epithelium specified and maintained by its adjacent mesenchyma under tight control of the male steroid hormone, testosterone.[37-39] When prostate epithelial cells are undergoing neoplastic transformation, initially the growth of glandular epithelium is still stimulated and maintained by testicular androgen with its action mediated by the androgen receptor (AR) in the glandular epithelium and stromal fibroblasts.[39-41] After androgen-deprivation therapy for the treatment of prostate cancer, prostate epithelial growth becomes androgen refractory and is no longer controlled by androgenic hormones but rather by yet-to-be-defined factors secreted by cancer cells, as well as cells in the cancer microenvironment.[42-45] This altered control mechanism coincides with inherited and epigenetically driven intrinsic genomic instability, DNA repair defects, and acquisition of multiple survival mechanisms by the cancer cells, and allows cancer cells to escape from normal developmental constraints and undergo a de-differentiation process with possible nonrandom genetic changes.[15,16,46,47] Remarkably, despite genetic alterations in cancer cells, they often remain nontumorigenic in mice and, even when tumorigenic, seldom acquire metastatic potential.[48,49] We believe certain undefined host factors could contribute to an increased malignant potential of cancer cells. For example, host inflammatory cytokines could play a positive and directive role in prostate cancer growth, progression, and tropism toward bone by indirectly affecting cells in the host microenvironment. Tumor- and host stroma–derived factors, such as transforming growth factor–β1, are known to induce tumor angiogenesis and elicit stromal reactions characterized by the transformation of resident fibroblasts to inductive myofibroblast and deposition of excess extracellular matrices.[50] The altered stromal microenvironment could help drive local tumorigenesis and subsequently enhance tumor cell distant dissemination through a positive feedback mechanism as depicted in Figure 1. The progression of cancer cells, therefore, can occur in 3 steps: genetic instability of transformed precancerous epithelial cells contributes to altered cell behaviors, including increased cell proliferation, decreased apoptosis, and increased cell motility and survival; the behaviorally altered precancerous or cancerous epithelial cells could trigger a stromal response or desmoplastic reaction, with morphologic and gene expression changes that particularly increase the deposition of extracellular matrices and also the secretion of growth and angiogenic factors that collectively induce genetic changes and program the inductivity of the stromal fibroblasts. In consequence, the changing stromal microenvironment could induce additional genetic modifications of the cancer epithelial cells. The resulting cancer cells could become highly unstable with increased motility, invasive and metastatic potential. This interaction between stroma and epithelium is a "vicious cycle" maintained by permanent genetic changes within the tumor and stromal cell compartments, ultimately contributing to the progression of an invasive cancer.[5,51]

How Cancer Cells Respond to a Changing Tumor Microenvironment

Osteomimicry

Cancer cells are capable of mimicking the characteristics of cells in the tumor microenvironment. Dramatic examples include osteomimicry, the ability of cancer cells to express genes normally highly restricted to bone cells before, during, or after metastasis through the synthesis, secretion, and accumulation of bone-like proteins such as osteocalcin (OC), osteopontin, bone sialoprotein (BSP), and osteonectin, even forming mineralizing bone under certain culture conditions.[29,52,53] Cancer cells are also capable of expressing receptor activator of nuclear factor–κB

Figure 1 | Vicious Cycle of Altered Stromal Cell Microenvironment, Tumorigenesis, and Metastasis
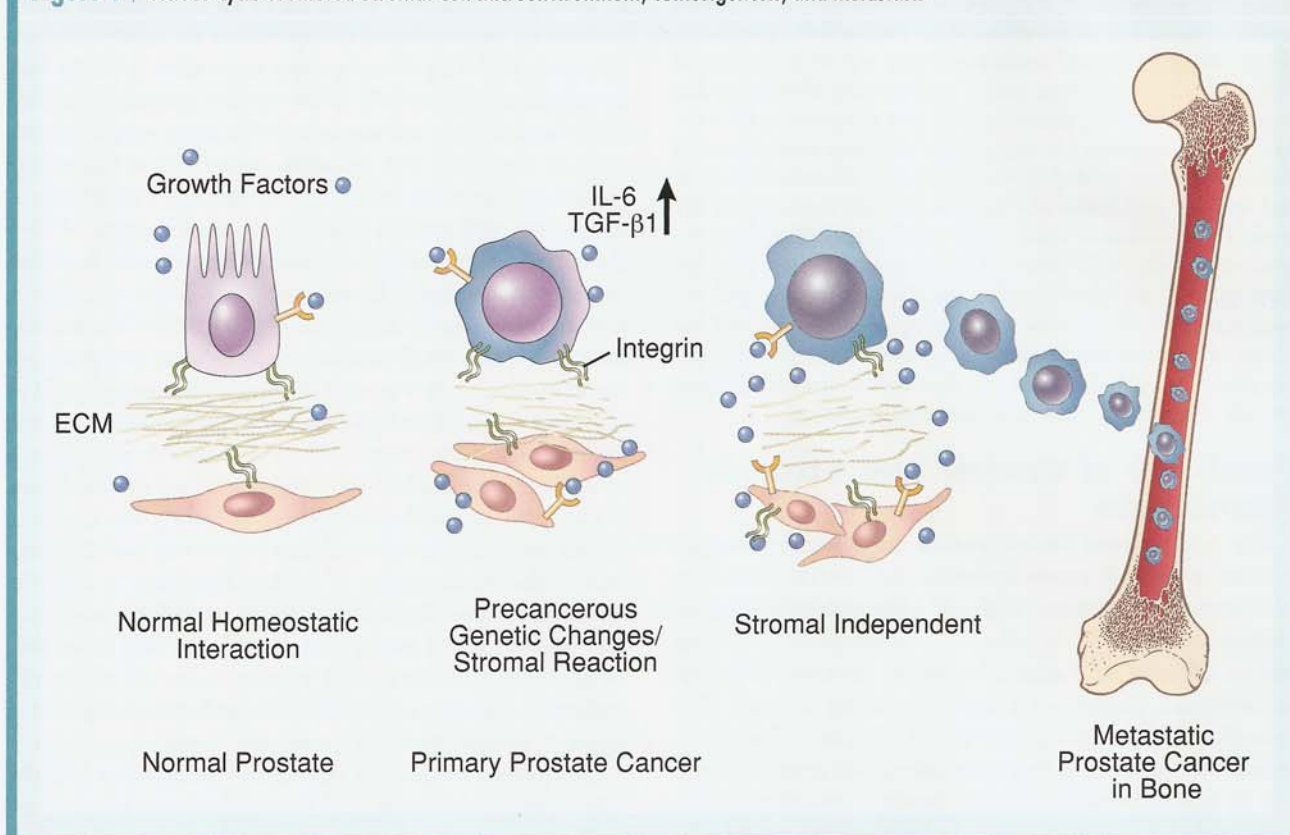
Dynamic and reciprocal interaction between prostate cancer and prostate stromal cells that results in genetic changes in prostate cancer and prostate or bone stromal cells through a cellular interaction mechanism defined here in a "vicious cycle" manner. This reciprocal cellular interaction could contribute to the invasiveness and metastasis of human prostate cancer cells to bone and visceral organs. The normal prostate epithelial cell homeostatic interaction with its adjacent stroma through growth factors and extracellular matrices via growth factor receptors or integrins is deranged because of genetic modifications occurring in the epithelium. The genetically altered prostate epithelial cell provokes a stromal desmoplastic reaction, which sets off a chain reaction, such as increased TGF-β1 and IL-6, in reciprocally modulating the cancer epithelium, which becomes prostate stroma independent and eventually invades and migrates to bone and visceral organs and exerts strong reciprocal interaction with the resident host cells that facilitate the growth and survival of cancer cells at metastatic sites.
Abbreviations: ECM = extracellular matrices; IL-6 = interleukin-6; TGF-β1 = transforming growth factor–β1.

(RANK) ligand (RANKL) and parathyroid hormone-related peptide, which are known to directly or indirectly increase bone turnover through increased RANKL (associated with cancer cells)-RANK (associated with osteoclasts) interaction and activation of osteoclastogenesis.[54,55] These unusual characteristics are because of the ability of cancer cells to respond to factors secreted by cancer cells or by host cells in the immediate microenvironment. Using human prostate cancer and bone cells as models to define the molecular basis of osteomimicry, we identified a unique key switch controlling OC and BSP gene expression that is operative in prostate cancer but not in bone cells.[56,57] This switch resides at the 8-base nucleotide sequences called the cyclic adenosine monophosphate (cAMP) responsive element (CRE), within OC and BSP promoters, and is responsible for the regulation of endogenous OC and BSP as well as their promoter activities.[58] We further showed that CRE activation is under the control of a soluble factor secreted by prostate cancer and host cells, with its action mediated by cAMP-dependent protein kinase A (cAMP-PKA) activation. The activation of CRE binding protein (CREB) was demonstrated by the observation of CREB phosphorylation upon activation of cAMP-dependent PKA, phosphorylated CREB translocation into the cell nucleus, and its

subsequent binding to CRE as shown by gel shift and supershift assays. Based on these data, Figure 2 depicts a number of possible molecular pathways mediating osteomimicry in human prostate cancer cells.[42,45,58,59] The binding of a soluble factor to a putative cell surface receptor links with the activation of intracellular cAMP-PKA signaling pathway. The putative receptor can be a G protein–coupled receptor that mediates downstream signaling via PKA or, alternatively, can be linked to a yet-to-be-identified receptor that binds to the soluble factor and transmits intracellular signaling through the cAMP-PKA system. The participation by a soluble factor, β_2-microglobulin (β2M) was shown to activate the cAMP-PKA system. β_2-microglobulin is known to form a complex with a classical major histocompatibility class 1 antigen, which could implicate the role of this complex in the downstream intracellular signaling of osteomimicry in human prostate cancer cells. β_2-microglobulin could participate directly in activating cAMP-PKA system or participate in CREB and its downstream activation of target genes. The biologic consequences of osteomimicry could be numerous. For example, the activation of OC and BSP expression could result in the recruitment of bone cells such as osteoclasts and osteoblasts that participate in enhanced osteoclastogenesis, ie, increased bone turnover or

bone "pitting" to create new sites in support of cancer cell attachment, growth, and colonization in bone.[60,61] Osteocalcin and BSP activation could contribute to new bone formation and mineralization.[62] Prostate cancer cells derived from LNCaP cells with increased bone metastatic potential, such as C4-2 and C4-2B, have activated OC and BSP gene expression and are also capable of forming bone nodules when subjected to mineralizing cell culture conditions in vitro.[63] The activation of CREB could result in marked gene expression changes in cancer cells and cells in the cancer microenvironment that could facilitate cancer cell growth, survival, and colonization in bone. It is interesting to note that of ~4000 potential CREB target genes, only a fraction are expressed in a cell context–dependent manner.[64,65] This again supports the notion that the host microenvironment might contribute to cancer cell growth, resistance to apoptosis, and conventional hormone, radiation, and chemotherapy. A large number of other downstream genes unrelated to osteomimicry were also found to be regulated by cAMP-PKA activation. For example, upon cAMP-PKA/CREB activation in cancer cells, the phosphorylated CREB is responsible for the recruitment of CBP/p300 to activate downstream genes, such as vascular endothelial growth factor, cyclins, and survival factors aiding the growth and survival of cancer cells.[66,67] It has been shown that removing androgen from cultured prostate cancer cells elicits a neuroendocrine phenotype in cancer cells because of CREB activation.[42,59,67] As expected, neuroendocrine differentiation, which has been associated with increased invasion, migration, and metastasis of prostate cancer cells was also activated by cAMP mimetics such as dibutyl cAMP or forskolin.[42,59]

Activation of the G protein, via the cAMP–activated β2 adrenergic receptor, has been shown to compensate for the requirement of androgen to activate AR-downstream genes.[59] This phenomenon could have clinical importance, because it has been proposed that the activation of AR by suboptimal concentrations of androgen could be responsible for the survival of prostate cancer cells in patients subjected to androgen-withdrawal treatment regimens.[45]

Vasculogenic Mimicry

Cancer cells often grow under stress conditions because of the lack of oxygen, increased cell crowding, and the lack of sufficient nutrients. In response to these conditions, adaptive changes by cancer cells have been observed creating their own blood vessels, such as ischemia-induced vasculogenic mimicry in melanoma, breast, and prostate cancer.[62,68,69] Hendrix et al demonstrated the plasticity of melanoma cells, which formed tubular structures with patterned matrix deposition including laminin, heparan sulfate proteoglycans, and collagens IV and VI, expressing genes normally expressed by vascular endothelial cells and interconnecting with the preexisting blood vessels.[31] This adaptive capability of cancer cells toward changes in microenvironmental cues could sustain their growth and survival at metastatic sites and allow them to gain further invasive and migratory potentials. A direct link between vasculogenic mimicry, the activation of focal adhesion kinase (FAK) through the phosphorylation of tyrosine-397 and -576, and decreased plasminogen activation through decreased urokinase activity has been reported.[70] Because FAK

**Figure 2** | Molecular Mechanisms of Osteomimicry in Prostate Cancer Cells[42,45,58,59]
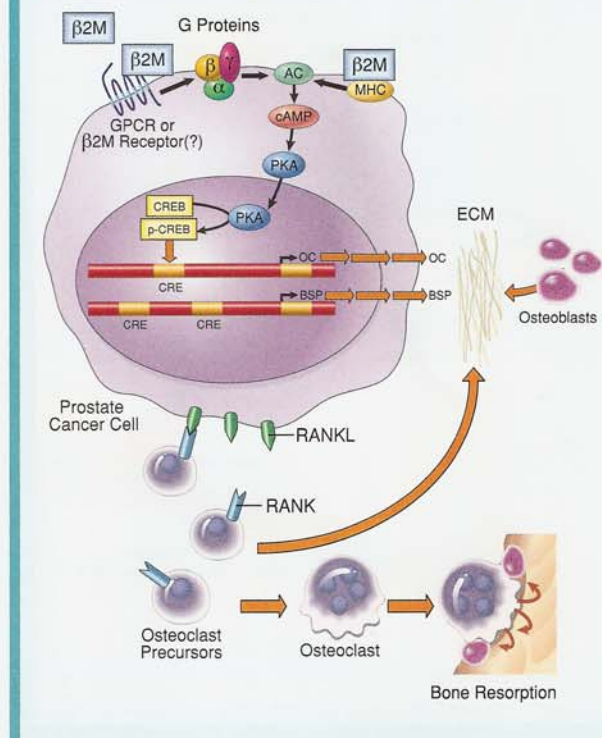
Prostate cancer cells have the ability to mimic gene expression and behaviors of bone cells by synthesizing and depositing bone-like proteins, such as OC and BSP.[58] Among factors that could regulate the expression of these proteins, we found β2M induces the expression of OC and BSP through an activation of the cAMP-PKA–signaling pathway with its downstream activation of cAMP and CREB. β2-microglobulin is considered a housekeeping gene with a uniformed expression of its messenger RNA in many cells. Interestingly, β2M protein expression varied widely between cells, with higher expression in more aggressive human prostate cancer cell lines. β2-microglobulin could exert its action via a number of membrane receptors, such as G protein–coupled receptor, major histocompatibility antigen complex, or a yet-to-be-identified β2M receptor. Alternatively, β2M could also exert its action intracellularly by directly modulating CREB downstream target gene expression. The resulting increased expression and deposition of OC and BSP in the bone matrix could recruit osteoblasts and osteoclasts and initiate increased bone turnover (ie, increased bone resorption and formation) through osteoclastogenesis, which facilitates prostate cancer bone homing and colonization. Under androgen-deprived conditions, prostate cancer cells could survive by activating the cAMP-PKA–signaling pathway, which contributes to the neuroendocrine differentiation and increased efficiency of AR transactivation of target genes in prostate cancer cells.[42,45,59] Abbreviations: ? = yet-to-be-identified; GPCR = G protein–coupled receptor; MHC = major histocompatibility

activation has been associated with increased cell invasion and migration, and plasminogen activation is crucial for blood clotting, the ability of cancer cells to alter FAK and plasminogen activation is consistent with observations of an increased ability of cancer cells to metastasize and its association with aberrant wound-healing properties.[30,71,72]

Epithelial to Mesenchymal Transition

Epithelial to mesenchymal transition (EMT) is a fundamental cellular process whereby an epithelial cell undergoes a structural and functional transition to assume the phenotype and behavior of a mesenchymal cell, characterized by increased migratory and invasive properties in embryonic development and also upon neoplastic progression.[73] It is now well accepted that EMT occurs in a number of human cancers, including prostate cancer, and EMT is associated with increased cancer invasion and metastasis. Epithelial to mesenchymal transition is a highly dynamic process that signals the plasticity of cancer cells (Figure 3). Cancer metas-

Figure 3 Epithelial to Mesenchymal Transition and its Reversal of Mesenchymal to Epithelial Transition During the Progression of Prostate Cancer
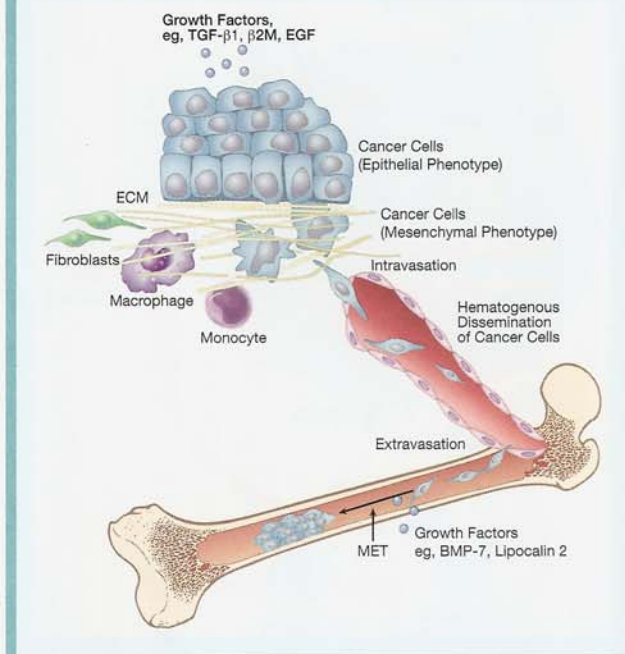
Increased migration and invasion of prostate cancer cells before bone metastasis can be initiated through EMT under the influence of increased growth factor signaling (eg, transforming growth factor–β1, epidermal growth factor, or β2M). The sources of growth factors and cytokines can be originated from resident fibroblasts or inflammatory cells within cancer-associated stroma, and these factors can form a complex with extracellular matrices before delivery to cancer cells. Cancer cells can metastasize to bone or visceral organs through hematogenous spread, and when arriving at the metastatic sites such as bone, cancer cells could undergo MET under the influence of BMP-7 and lipocalin 2, by re-expressing epithelial cell–associated markers, such as increased E-cadherin and decreased expression of vimentin and N-cadherin. This MET reversal could increase prostate cancer cell adhesion among themselves, with increased growth and survival potential in bone and visceral organs.

Abbreviations: ECM = extracellular matrices; EGF = epidermal growth factor; TGF = transforming growth factor

tasis is often preceded by EMT, but upon the completion of the metastatic process, cancer cells can revert their phenotype and behavior by undergoing mesenchymal to epithelial transition (MET) to increase their adhesion and growth at metastatic sites. This suggests the importance of the host microenvironment that could trigger EMT and its reversal, MET, epigenetically.[74]

There are numerous well-characterized molecular pathways that describe the underlying key regulatory processes of EMT in human cancer cells. Activation of transforming growth factor–β signaling enhances receptor tyrosine kinases and Ras activities that together can drive the translocation of Smad and Snail transcription factors from the cytoplasmic to the nuclear compartment, and the activation or suppression of downstream target genes associated with EMT have been widely proposed as the key regulatory mechanisms underlying EMT in human cancer cells.[75,76] Other molecular mechanisms include the activation of Wnt and β-catenin signaling, which suppresses E-cadherin and initiates the early step of EMT[77,78]; activation of the Hedgehog pathway, which contributes to increased EMT and stem cell differentiation,[73,79] both important features shared by invasive cancer cells; and activation of nuclear factor–κB transcription factor, which translocates into the cell nucleus, improves the survival of cancer cells, and allows them to resist apoptotic death after therapeutic intervention.[80,81] Figure 3 depicts selective growth control–signaling pathways of EMT and MET as a continuum of prostate cancer progression.

How Host Cells Contributed to the Genesis of Cancer

Host Infiltrating Inflammatory Cells

Cancer development often coincides with active chronic and recurrent inflammatory responses caused by innate immune responses to the presence of altered cancer epithelial cells and bacterial or viral infections at the site of the cancer origin. The infiltrating inflammatory cells have been shown to release reactive oxygen and nitrogen species such as hydrogen peroxide, superoxide, and nitric oxide as a part of the host defense mechanism to eradicate the "foreign" cells and invading organisms.[82,83] Responses to the presence of these highly reactive oxygen and nitrogen radicals released by the inflammatory cells and cancer cells could induce DNA damage to cancer cells and host stroma, activating DNA repair and cell proliferation programs to compensate for the cell loss resulting from failure to repair and subsequent cell death.[84,85] An extensive literature review suggests the possible functional and signaling roles of oxygen and nitrogen radicals in eliciting cell responses to stress and escape mechanisms for survival.[86] These observations collectively support the important role of the inflammatory cascade in carcinogenesis. De Marzo et al proposed a role for inflammation in prostate cancer development when they found foci of proliferative inflammatory atrophy as precursor lesions before the detection of prostate intraepithelial neoplasia, a known early pathologic lesion associated with human prostate cancer development.[87,88] They reported compelling epidemiologic evidence to suggest a link between prostate inflammation and prostate cancer in men.[87] For example, a positive correlation was found between prostatitis and sexually transmitted infections and increased prostate cancer risk.[88-90] Intake of antiinflammatory drugs and antioxidants has been shown to decrease prostate cancer risk.[91-94] Genetic studies revealed further supportive evidence that ribonuclease L, encoding an interferon-inducible ribonuclease,[95,96] and macrophage scavenger receptor 1, encoding subunits of the macrophage scavenger receptor,[96-98] are candidates as inherited susceptibility genes for familial prostate cancer. Conversely, the loss of glutathione S-transferase π, encoding a glutathione S-transferase capable of inactivating ROS and thus decreasing genome damage, has been found to occur frequently in prostate cancer.[87,98-100] Figure 4 emphasizes the potential roles of inflammatory processes and prostate cancer development.

Host Stem Cells

Stem cells are characterized by their abilities of self-renewal, slow cycling, and less well-differentiated properties. There are potentially 2 pools of stem cells that broadly could contribute to local cancer growth and its distant metastasis. One of the classical stem cell populations resides in the basal layer of prostate gland. With their unlimited growth potential and self-renewal property, they become a constant source of cancer cells and pop-

Figure 4 | Contribution of Inflammatory Cells on Progression of Prostate Cancer
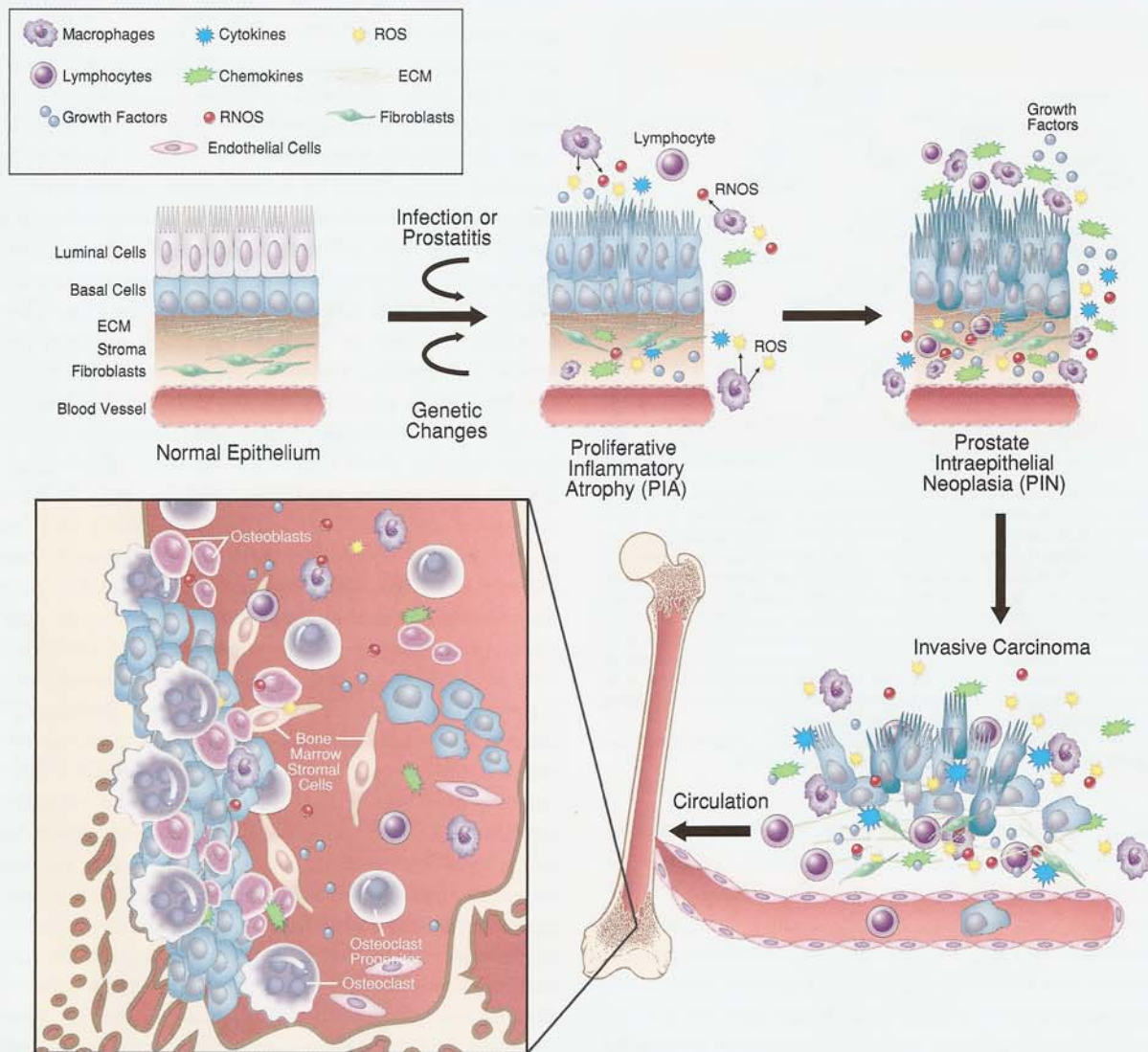
Recruitment of inflammatory cells to the prostate gland can occur under a variety of physiologic and pathophysiologic conditions, such as wound, infection, prostatitis, and cancer. Genetically altered prostate epithelial cells under the influence of resident fibroblast inflammatory (such as macrophage and lymphocytes) and endothelial cells progress further through additional genetic changes triggered by ROS or RNOS. The genetic unstable prostate cancer cell clusters can form proliferative inflammatory atrophy and then proceed to prostate intraepithelial neoplasia before becoming invasive prostate cancer. Upon metastasizing to bone, prostate cancer cells interact with bone cells, such as osteoblasts, osteoclasts, and marrow stromal cells, to increase their growth and survival in bone. Through cellular interaction with osteoclasts, prostate cancer cells also promote osteoclastogenesis and bone turnover by increased osteoclast maturation via RANKL (localized on prostate cancer or osteoblast cell surface) and RANK (localized on the cell surface of osteoclast) interaction. Further prostate growth and cancer survival in bone are promoted by increased bone turnover, ie, increased release of soluble growth factors, cytokines, and extracellular matrices. Abbreviations: ECM = extracellular matrices; RNOS = reactive nitrogen species

ulate the entire tumor mass.[101-103] For example, the basal cells in the prostate gland shared gene expression profiles with cancer cells and could be considered as the prostate cancer progenitors.[102,104] Another postulated pool of stem cells could originate from the host.[22,105] Bone marrow–derived progenitor stem cells have migratory, invasive, and self-renewal potential.[106,107] Upon recruitment into a tumor, these cells could exist in a specific physical location or "niche" and could actually fuse with adult stem cells and participate in cancer cell growth and metastasis. This pool of cells, which has great proliferative and pluripotent potentiality and has been shown to migrate into primary or metastatic cancers, creates a rich source of growth factor and a

cytokine niche supporting the growth and expansion of cancer cells.[25] Although there is no concrete example of this kind of mechanism in prostate cancer, a recent work by Kaplan et al showed that the ability of tumor cells to metastasize to a predetermined location can be explained by the previous "marking" of the metastatic site by bone marrow hematopoietic progenitor cells that express vascular endothelial growth factor receptor 1 (Flt-1) and VLA-4 (integrin $\alpha 4\beta 1$).[108-110] The expression of $\alpha 4\beta 1$, a known receptor of fibronectin produced by resident fibroblasts, in response to tumor-specific factors, creates a permissive niche for the incoming migrating tumor cells.[109,110] If this mechanism has general applicability, it can be proposed that a previously

Figure 5 | Co-Targeting Cancer and Its Host for the Treatment of Prostate Cancer Metastasis
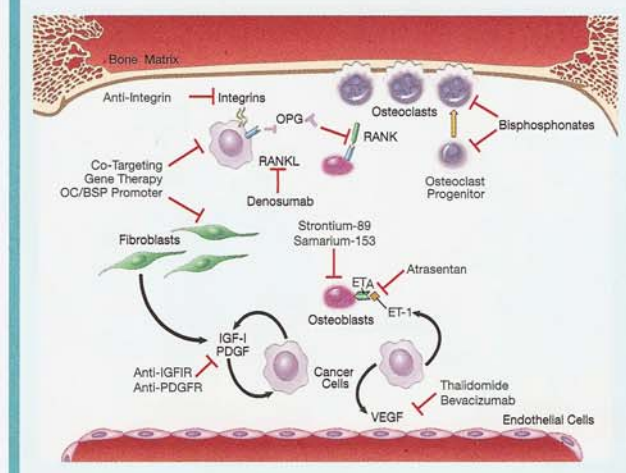
The strategies of co-targeting tumor and tumor microenvironment have been used in the clinic for the treatment of prostate cancer metastasis. As illustrated herein, cancer epithelium can be targeted effectively by the use of chemotherapy. As a rational combination, (1) tumor-associated endothelium can be targeted with antiangiogenic drugs (eg, thalidomide or bevacizumab); (2) the growth of osteoblasts can be targeted with a radionuclide (strontium-89 or samarium-153) or with an endothelin-1A receptor antagonist, atrasentan; (3) growth factors/growth factor receptors signaling (eg, insulin-like growth factor/insulin-like growth factor–1R, platelet-derived growth factor/platelet-derived growth factor receptor) or extracellular matrix/integrin interactions are also popular therapeutic targets by the use of small molecules or isotype-specific antibodies; (4) interphase between prostate cancer and bone cell interaction can be targeted by bisphosphonates to slow down bone turnover, and osteoclast/prostate cancer/osteoblast interaction can be effectively targeted with osteoprotegerin or denosumab; (5) prostate cancer and bone stroma and their interactions can be co-targeted using an adenoviral-based gene therapy with therapeutic cytotoxic HSV-thymidine kinase or viral replication controlled by tissue-specific and tumor-restrictive promoter, human OC or human BSP.

Abbreviations: IGF-1 = insulin-like growth factor–1; OPG = osteoprotegerin; PDGF = platelet-derived growth factor; PDGFR = platelet-derived growth factor receptor; VEGF = vascular endothelial growth factor

established bone marrow stem cell niche, in response to tumor-derived factors by resident marrow stromal cells, could also be responsible for attracting prostate cancer bone metastasis.[108-111] It has already been proposed that the homing mechanism of prostate cancer cells might involve chemokine (stromal cell–derived factor 1 or CXCR12) derived from marrow stromal cells and chemokine receptor (CXCR4) on the cell surface of prostate cancer cells[112]; cell adhesion molecules on marrow endothelial cells and integrins ($\alpha v\beta 3$ and $\alpha 4\beta 1$) on the cell surface of prostate cancer cells[113,114]; hedgehog produced by cancer cells, which triggers a host prostate or bone stromal response mediated by paracrine interaction with cell surface receptors, patched1[115-117]; complementary growth factors/growth factor receptors and/or extracellular matrices/integrins produced by prostate cancer cells and bone cells, such as marrow stromal cells, osteoblasts, osteoclasts, or bone marrow progenitor stem cells. Understanding the molecular mechanisms at the interface of prostate cancer and host cells could help in the future development of novel therapies for the treatment of prostate cancer bone metastasis.[5,45,61]

Strategies to Co-Target Cancer and Its Host for the Treatment of Lethal Prostate Cancer Metastasis

Increasing evidence suggests that an intimate interaction between cancer and its host contributes to local prostate cancer growth and distant metastasis. Cancer and host interaction has also been shown to support the survival of prostate cancer cells when subjected to hormone therapy, chemotherapy, and radiation therapy.[5,118,119] Through epigenetic cancer and host interaction, additional genetic changes can be introduced into both of the interactive cell types and further evolve the tumor phenotypes and genotypes.[5,10,13,15] This could be the molecular basis for cancer's status as a constantly moving target for which therapy must be tailored on an individual basis. For these reasons, the most effective means of controlling prostate cancer local growth and distant metastasis might be co-targeting strategies that eliminate cancer cell growth and also deprive cancer cells of their support systems from the host. This will hopefully eliminate or minimize the ability of cancer cells to survive and undergo continuous genetic and behavioral evolution by escaping previously effective therapies. The best known example is the androgen-independent progression of prostate cancer cells, by which they escape hormonal dependency and become unresponsive to androgen withdrawal.[45,120] The concept of co-targeting cancer and host has already been backed up by a number of examples. As depicted in Figure 5, these are the uses of an antiangiogenic drug (eg, thalidomide) to target the endothelium in combination with chemotherapy targeting prostate cancer cells[121,122]; the combined use of a radionuclide, Sr89 or Sm153 to target the osteoblasts with chemotherapy targeting prostate cancer cells[123]; the use of an endothelin (ET)–1 receptor antagonist, atrasentan, to block the paracrine interaction between prostate cancer cells, which produce ET-1, with its action mediated by the ET_A receptor on the cell surface of osteoblasts[124]; interrupting paracrine/autocrine growth factors and growth factor receptors or extracellular matrix and integrin interactions by the use of antibodies such as neutralizing antibody against insulin-like growth factor–1R, platelet-derived growth factor receptor, integrin isotype-specific antibodies and the stem cell hedgehog signaling pathway "hijacked" by cancer cells[5,125,126]; targeting the interphase between prostate cancer and bone cell interaction by slowing down bone turnover with bisphosphonates, and osteoclast/prostate cancer interaction with a decoy RANK receptor, osteoprotegerin[54,127] or RANKL antibody, denosumab (AMG162); and co-targeting prostate cancer and bone stroma using an adenoviral-based gene therapy with therapeutic cytotoxic HSV-thymidine kinase or viral replication controlled by tissue-specific and tumor-restrictive promoter, human OC or human BSP.[119,128,129] The rationales of these strategies are to interrupt cancer-host interaction and communication and make the host microenvironment hostile to cancer growth and survival. A broad range of experimental approaches holds promise and could someday change how cancer metastasis is evaluated and lead to its treatment on an individual basis.

References

1. Hunter K. Host genetics influence tumour metastasis. *Nat Rev Cancer* 2006; 6:141-146.
2. Bissell MJ, Labarge MA. Context, tissue plasticity, and cancer: are tumor stem cells also regulated by the microenvironment? *Cancer Cell* 2005; 7:17-23.
3. Haslam SZ, Woodward TL. Host microenvironment in breast cancer development: epithelial-cell-stromal-cell interactions and steroid hormone action in normal and cancerous mammary gland. *Breast Cancer Res* 2003; 5:208-215.

4. Lynch CC, Matrisian LM. Matrix metalloproteinases in tumor-host cell communication. *Differentiation* 2002; 70:561-573.

5. Chung LW, Baseman A, Assikis V, et al. Molecular insights into prostate cancer progression: the missing link of tumor microenvironment. *J Urol* 2005; 173:10-20.

6. Baker SG, Lichtenstein P, Kaprio J, et al. Genetic susceptibility to prostate, breast, and colorectal cancer among Nordic twins. *Biometrics* 2005; 61:55-63.

7. Heavey PM, McKenna D, Rowland IR. Colorectal cancer and the relationship between genes and the environment. *Nutr Cancer* 2004; 48:124-141.

8. Gallagher PG, Bao Y, Prorock A, et al. Gene expression profiling reveals cross-talk between melanoma and fibroblasts: implications for host-tumor interactions in metastasis. *Cancer Res* 2005; 65:4134-4146.

9. Gleave M, Hsieh JT, Gao CA, et al. Acceleration of human prostate cancer growth in vivo by factors produced by prostate and bone fibroblasts. *Cancer Res* 1991; 51:3753-3761.

10. Thalmann GN, Anezinis PE, Chang SM, et al. Androgen-independent cancer progression and bone metastasis in the LNCaP model of human prostate cancer. *Cancer Res* 1994; 54:2577-2581.

11. Yoneda T, Hiraga T. Crosstalk between cancer cells and bone microenvironment in bone metastasis. *Biochem Biophys Res Commun* 2005; 328:679-687.

12. Paget S. The distribution of secondary growths in cancer of the breast. 1889. *Cancer Metastasis Rev* 1989; 8:98-101.

13. Hill R, Song Y, Cardiff RD, et al. Selective evolution of stromal mesenchyme with p53 loss in response to epithelial tumorigenesis. *Cell* 2005; 123:1001-1011.

14. Pathak S, Nemeth MA, Multani AS, et al. Can cancer cells transform normal host cells into malignant cells? *Br J Cancer* 1997; 76:1134-1138.

15. Rhee HW, Zhau HE, Pathak S, et al. Permanent phenotypic and genotypic changes of prostate cancer cells cultured in a three-dimensional rotating-wall vessel. *In Vitro Cell Dev Biol Anim* 2001; 37:127-140.

16. Thalmann GN, Sikes RA, Wu TT, et al. LNCaP progression model of human prostate cancer: androgen-independence and osseous metastasis. *Prostate* 2000; 44:91-103.

17. Tuxhorn JA, Ayala GE, Rowley DR. Reactive stroma in prostate cancer progression. *J Urol* 2001; 166:2472-2483.

18. Bedogni B, Welford SM, Cassarino DS, et al. The hypoxic microenvironment of the skin contributes to Akt-mediated melanocyte transformation. *Cancer Cell* 2005; 8:443-454.

19. Lewis CE, Pollard JW. Distinct role of macrophages in different tumor microenvironments. *Cancer Res* 2006; 66:605-612.

20. Radisky DC, Levy DD, Littlepage LE, et al. Rac1b and reactive oxygen species mediate MMP-3-induced EMT and genomic instability. *Nature* 2005; 436:123-127.

21. Zou W. Immunosuppressive networks in the tumour environment and their therapeutic relevance. *Nat Rev Cancer* 2005; 5:263-274.

22. Fidler IJ. The organ microenvironment and cancer metastasis. *Differentiation* 2002; 70:498-505.

23. Horak CE, Steeg PS. Metastasis gets site specific. *Cancer Cell* 2005; 8:93-95.

24. Minn AJ, Kang Y, Serganova I, et al. Distinct organ-specific metastatic potential of individual breast cancer cells and primary tumors. *J Clin Invest* 2005; 115:44-55.

25. Constantinescu SN. Stem cell generation and choice of fate: role of cytokines and cellular microenvironment. *J Cell Mol Med* 2000; 4:233-248.

26. Nojima H. Cell cycle checkpoints, chromosome stability and the progression of cancer. *Hum Cell* 1997; 10:221-230.

27. Blackburn EH. Telomeres and telomerase: their mechanisms of action and the effects of altering their functions. *FEBS Lett* 2005; 579:859-862.

28. Blasco MA. Telomeres and human disease: ageing, cancer and beyond. *Nat Rev Genet* 2005; 6:611-622.

29. Koeneman KS, Yeung F, Chung LW. Osteomimetic properties of prostate cancer cells: a hypothesis supporting the predilection of prostate cancer metastasis and growth in the bone environment. *Prostate* 1999; 39:246-261.

30. Dvorak HF. Tumors: wounds that do not heal. Similarities between tumor stroma generation and wound healing. *N Engl J Med* 1986; 315:1650-1659.

31. Hendrix MJ, Seftor EA, Hess AR, et al. Vasculogenic mimicry and tumour-cell plasticity: lessons from melanoma. *Nat Rev Cancer* 2003; 3:411-421.

32. Bajou K, Noel A, Gerard RD, et al. Absence of host plasminogen activator inhibitor 1 prevents cancer invasion and vascularization. *Nat Med* 1998; 4:923-928.

33. Boccaccio C, Comoglio PM. A functional role for hemostasis in early cancer development. *Cancer Res* 2005; 65:8579-8582.

34. Lassam N, Jay G. Suppression of MHC class I RNA in highly oncogenic cells occurs at the level of transcription initiation. *J Immunol* 1989; 143:3792-3797.

35. Gatti L, Zunino F. Overview of tumor cell chemoresistance mechanisms. *Methods Mol Med* 2005; 111:127-148.

36. Moreno J, Krishnan AV, Feldman D. Molecular mechanisms mediating the antiproliferative effects of vitamin D in prostate cancer. *J Steroid Biochem Mol Biol* 2005; 97:31-36.

37. Chung LW. The role of stromal-epithelial interaction in normal and malignant growth. *Cancer Surv* 1995; 23:33-42.

38. Cunha GR. Role of mesenchymal-epithelial interactions in normal and abnormal development of the mammary gland and prostate. *Cancer* 1994; 74:S1030-S1044.

39. Cunha GR, Donjacour AA, Cooke PS, et al. The endocrinology and developmental biology of the prostate. *Endocr Rev* 1987; 8:338-362.

40. Chung LW, Anderson NG, Neubauer BL, et al. Tissue interactions in prostate development: roles of sex steroids. *Prog Clin Biol Res* 1981; 75A:177-203.

41. Thompson TC, Cunha GR, Shannon JM, et al. Androgen-induced biochemical responses in epithelium lacking androgen receptors: characterization of androgen receptors in the mesenchymal derivative of urogenital sinus. *J Steroid Biochem* 1986; 25:627-634.

42. Amorino GP, Parsons SJ. Neuroendocrine cells in prostate cancer. *Crit Rev Eukaryot Gene Expr* 2004; 14:287-300.

43. Culig Z. Androgen receptor cross-talk with cell signalling pathways. *Growth Factors* 2004; 22:179-184.

44. Sanchez P, Clement V, Ruiz i Altaba A. Therapeutic targeting of the Hedgehog-GLI pathway in prostate cancer. *Cancer Res* 2005; 65:2990-2992.

45. Scher HI, Sawyers CL. Biology of progressive, castration-resistant prostate cancer: directed therapies targeting the androgen-receptor signaling axis. *J Clin Oncol* 2005; 23:8253-8261.

46. Charames GS, Bapat B. Genomic instability and cancer. *Curr Mol Med* 2003; 3:589-596.

47. Mendez O, Fernandez Y, Peinado MA, et al. Anti-apoptotic proteins induce non-random genetic alterations that result in selecting breast cancer metastatic cells. *Clin Exp Metastasis* 2005; 22:297-307.

48. Hunter KW. Host genetics and tumour metastasis. *Br J Cancer* 2004; 90:752-755.

49. Koop S, MacDonald IC, Luzzi K, et al. Fate of melanoma cells entering the microcirculation: over 80% survive and extravasate. *Cancer Res* 1995; 55:2520-2523.

50. Bhowmick NA, Chytil A, Plieth D, et al. TGF-beta signaling in fibroblasts modulates the oncogenic potential of adjacent epithelia. *Science* 2004; 303:848-851.

51. Mundy GR. Mechanisms of bone metastasis. *Cancer* 1997; 80:S1546-S1556.

52. Lecrone V, Li W, Devoll RE, et al. Calcium signals in prostate cancer cells: specific activation by bone-matrix proteins. *Cell Calcium* 2000; 27:35-42.

53. Thomas R, True LD, Bassuk JA, et al. Differential expression of osteonectin/SPARC during human prostate cancer progression. *Clin Cancer Res* 2000; 6:1140-1149.

54. Keller ET. The role of osteoclastic activity in prostate cancer skeletal metastases. *Drugs Today (Barc)* 2002; 38:91-102.

55. Zhang J, Dai J, Qi Y, et al. Osteoprotegerin inhibits prostate cancer-induced osteoclastogenesis and prevents prostate tumor growth in the bone. *J Clin Invest* 2001; 107:1235-1244.

56. Huang WC, Zhau HE, Chung LW. Invasive prostate cancer cells secrete soluble protein factors that upregulate osteocalcin (OC) promoter activity: implication to stroma desmoplastic response and cancer metastasis. *J Urol* 2003; 169:154 (Abstract #597).

57. Yeung F, Law WK, Yeh CH, et al. Regulation of human osteocalcin promoter in hormone-independent human prostate cancer cells. *J Biol Chem* 2002; 277:2468-2476.

58. Huang WC, Xie Z, Konaka H, et al. Identification and characterization of CRE Cis-elements within human osteocalcin and bone sialoprotein promoters mediating osteomimicry of prostate cancer cells: role of cAMP-dependent PKA signaling pathway. *Cancer Res* 2006. In press.

59. Kasbohm EA, Guo R, Yowell CW, et al. Androgen receptor activation by G(s) signaling in prostate cancer cells. *J Biol Chem* 2005; 280:11583-11589.

60. Keller ET, Brown J. Prostate cancer bone metastases promote both osteolytic and osteoblastic activity. *J Cell Biochem* 2004; 91:718-729.

61. Logothetis CJ, Lin SH. Osteoblasts in prostate cancer metastasis to bone. *Nat Rev Cancer* 2005; 5:21-28.

62. Xiao Y, Haase H, Young WG, et al. Development and transplantation of a mineralized matrix formed by osteoblasts in vitro for bone regeneration. *Cell Transplant* 2004; 13:15-25.

63. Lin DL, Tarnowski CP, Zhang J, et al. Bone metastatic LNCaP-derivative C4-2B prostate cancer cell line mineralizes in vitro. *Prostate* 2001; 47:212-221.

64. Louie MC, Yang HQ, Ma AH, et al. Androgen-induced recruitment of RNA polymerase II to a nuclear receptor-p160 coactivator complex. *Proc Natl Acad Sci U S A* 2003; 100:2226-2230.

65. Zhang X, Odom DT, Koo SH, et al. Genome-wide analysis of cAMP-response element binding protein occupancy, phosphorylation, and target gene activation in human tissues. *Proc Natl Acad Sci U S A* 2005; 102:4459-4464.

66. Harris AL. Hypoxia--a key regulatory factor in tumour growth. *Nat Rev Cancer* 2002; 2:38-47.

67. Mayo LD, Kessler KM, Pincheira R, et al. Vascular endothelial cell growth factor activates CRE-binding protein by signaling through the KDR receptor tyrosine kinase. *J Biol Chem* 2001; 276:25184-25189.

68. Carmeliet P, Dor Y, Herbert JM, et al. Role of HIF-1alpha in hypoxia-mediated apoptosis, cell proliferation and tumour angiogenesis. *Nature* 1998; 394:485-490.

69. Lee M, Hwang JT, Lee HJ, et al. AMP-activated protein kinase activity is critical for hypoxia-inducible factor-1 transcriptional activity and its target gene expression under hypoxic conditions in DU145 cells. *J Biol Chem* 2003; 278:39653-39661.

70. Hess AR, Postovit LM, Margaryan NV, et al. Focal adhesion kinase promotes the aggressive melanoma phenotype. *Cancer Res* 2005; 65:9851-9860.

71. Hauck CR, Hsia DA, Schlaepfer DD. The focal adhesion kinase--a regulator of cell migration and invasion. *IUBMB Life* 2002; 53:115-119.

72. Kornberg LJ. Focal adhesion kinase and its potential involvement in tumor invasion and metastasis. *Head Neck* 1998; 20:745-752.

73. Hay ED. An overview of epithelio-mesenchymal transformation. *Acta Anat (Basel)* 1995; 154:8-20.

74. Thiery JP. Epithelial-mesenchymal transitions in development and pathologies. *Curr Opin Cell Biol* 2003; 15:740-746.

75. Davies M, Robinson M, Smith E, et al. Induction of an epithelial to mesenchymal transition in human immortal and malignant keratinocytes by TGF-beta1 involves MAPK, Smad and AP-1 signalling pathways. *J Cell Biochem* 2005; 95:918-931.

76. Janda E, Lehmann K, Killisch I, et al. Ras and TGF[beta] cooperatively regulate epithelial cell plasticity and metastasis: dissection of Ras signaling pathways. *J Cell Biol* 2002; 156:299-313.

77. Brabletz T, Hlubek F, Spaderna S, et al. Invasion and metastasis in colorectal cancer: epithelial-mesenchymal transition, mesenchymal-epithelial transition, stem cells and beta-catenin. *Cells Tissues Organs* 2005; 179:56-65.

78. Liebner S, Cattelino A, Gallini R, et al. Beta-catenin is required for endothelial-mesenchymal transformation during heart cushion development in the mouse. *J Cell Biol* 2004; 166:359-367.

79. Huber MA, Kraut N, Beug H. Molecular requirements for epithelial-mesenchymal transition during tumor progression. *Curr Opin Cell Biol* 2005; 17:548-558.

80. Bharti AC, Aggarwal BB. Nuclear factor-kappa B and cancer: its role in prevention and therapy. *Biochem Pharmacol* 2002; 64:883-888.

81. Kucharczak J, Simmons MJ, Fan Y, et al. To be, or not to be: NF-kappaB is the answer--role of Rel/NF-kappaB in the regulation of apoptosis. *Oncogene* 2003; 22:8961-8982.

82. Bauer G. Reactive oxygen and nitrogen species: efficient, selective, and interactive signals during intercellular induction of apoptosis. *Anticancer Res* 2000; 20:4115-4139.

83. Ernst P. Review article: the role of inflammation in the pathogenesis of gastric cancer. *Aliment Pharmacol Ther* 1999; 13:S13-S18.

84. Boonstra J, Post JA. Molecular events associated with reactive oxygen species and cell cycle progression in mammalian cells. *Gene* 2004; 337:1-13.

85. Slupphaug G, Kavli B, Krokan HE. The interacting pathways for prevention and repair of oxidative DNA damage. *Mutat Res* 2003; 531:231-251.

86. Fehrenbach E, Northoff H. Free radicals, exercise, apoptosis, and heat shock proteins. *Exerc Immunol Rev* 2001; 7:66-89.

87. De Marzo AM, Meeker AK, Zha S, et al. Human prostate cancer precursors and pathobiology. *Urology* 2003; 62:S55-S62.

88. Platz EA, De Marzo AM. Epidemiology of inflammation and prostate cancer. *J Urol* 2004; 171:S36-S40.

89. Mehik A, Hellstrom P, Sarpola A, et al. Fears, sexual disturbances and personality features in men with prostatitis: a population-based cross-sectional study in Finland. *BJU Int* 2001; 88:35-38.

90. Peyromaure M, Ravery V, Messas A, et al. Pain and morbidity of an extensive prostate 10-biopsy protocol: a prospective study in 289 patients. *J Urol* 2002; 167:218-221.

91. Fleshner NE, Klotz LH. Diet, androgens, oxidative stress and prostate cancer susceptibility. *Cancer Metastasis Rev* 1998; 17:325-330.

92. Hussain T, Gupta S, Adhami VM, et al. Green tea constituent epigallocatechin-3-gallate selectively inhibits COX-1 expression in human prostate carcinoma cells. *Int J Cancer* 2005; 113:660-669.

93. Lin DW, Nelson PS. The role of cyclooxygenase-2 inhibition for the prevention and treatment of prostate carcinoma. *Clin Prostate Cancer* 2003; 2:119-126.

94. Nelson WG, De Marzo AM, Deweese TL, et al. Preneoplastic prostate lesions: an opportunity for prostate cancer prevention. *Ann N Y Acad Sci* 2001; 952:135-144.

95. Maier C, Haeusler J, Herkommer K, et al. Mutation screening and association study of RNASEL as a prostate cancer susceptibility gene. *Br J Cancer* 2005; 92:1159-1164.

96. Nelson WG, De Marzo AM, DeWeese TL, et al. The role of inflammation in the pathogenesis of prostate cancer. *J Urol* 2004; 172:S6-S11; discussion S11-S12. Review.

97. Seppala EH, Ikonen T, Autio V, et al. Germ-line alterations in MSR1 gene and prostate cancer risk. *Clin Cancer Res* 2003; 9:5252-5256.

98. Xu J, Zheng SL, Komiya A, et al. Germline mutations and sequence variants of the macrophage scavenger receptor 1 gene are associated with prostate cancer risk. *Nat Genet* 2002; 32:321-325.

99. Bastian PJ, Palapattu GS, Lin X, et al. Preoperative serum DNA GSTP1 CpG island hypermethylation and the risk of early prostate-specific antigen recurrence following radical prostatectomy. *Clin Cancer Res* 2005; 11:4037-4043.

100. Henrique R, Jeronimo C. Molecular detection of prostate cancer: a role for GSTP1 hypermethylation. *Eur Urol* 2004; 46:660-669; discussion 669.

101. Rizzo S, Attard G, Hudson DL. Prostate epithelial stem cells. *Cell Prolif* 2005; 38:363-374.

102. Wang S, Garcia AJ, Wu M, et al. Pten deletion leads to the expansion of a prostatic stem/progenitor cell subpopulation and tumor initiation. *Proc Natl Acad Sci U S A* 2006; 103:1480-1485.

103. Xin L, Lawson DA, Witte ON. The Sca-1 cell surface marker enriches for a prostate-regenerating cell subpopulation that can initiate prostate tumorigenesis. *Proc Natl Acad Sci U S A* 2005; 102:6942-6947.

104. Garraway LA, Lin D, Signoretti S, et al. Intermediate basal cells of the prostate: in vitro and in vivo characterization. *Prostate* 2003; 55:206-218.

105. Religa P, Cao R, Bjorndahl M, et al. Presence of bone marrow-derived circulating progenitor endothelial cells in the newly formed lymphatic vessels. *Blood* 2005; 106:4184-4190.

106. Tabatabai G, Bahr O, Mohle R, et al. Lessons from the bone marrow: how malignant glioma cells attract adult haematopoietic progenitor cells. *Brain* 2005; 128:2200-2211.

107. Voermans C, van Heese WP, de Jong I, et al. Migratory behavior of leukemic cells from acute myeloid leukemia patients. *Leukemia* 2002; 16:650-657.

108. Kaplan RN, Riba RD, Zacharoulis S, et al. VEGFR1-positive haematopoietic bone marrow progenitors initiate the pre-metastatic niche. *Nature* 2005; 438:820-827.

109. Burger JA, Spoo A, Dwenger A, et al. CXCR4 chemokine receptors (CD184) and alpha4beta1 integrins mediate spontaneous migration of human CD34+ progenitors and acute myeloid leukaemia cells beneath marrow stromal cells (pseudoemperipolesis). *Br J Haematol* 2003; 122:579-589.

110. Gazitt Y. Homing and mobilization of hematopoietic stem cells and hematopoietic cancer cells are mirror image processes, utilizing similar signaling pathways and occurring concurrently: circulating cancer cells constitute an ideal target for concurrent treatment with chemotherapy and antilineage-specific antibodies. *Leukemia* 2004; 18:1-10.

111. Uchiyama H, Barut BA, Chauhan D, et al. Characterization of adhesion molecules on human myeloma cell lines. *Blood* 1992; 80:2306-2314.

112. Taichman RS, Cooper C, Keller ET, et al. Use of the stromal cell-derived factor-1/CXCR4 pathway in prostate cancer metastasis to bone. *Cancer Res* 2002; 62:1832-1837.

113. Cooper CR, Chay CH, Pienta KJ. The role of alpha(v)beta(3) in prostate cancer progression. *Neoplasia* 2002; 4:191-194.

114. Edlund M, Miyamoto T, Sikes RA, et al. Integrin expression and usage by prostate cancer cell lines on laminin substrata. *Cell Growth Differ* 2001; 12:99-107.

115. Karhadkar SS, Bova GS, Abdallah N, et al. Hedgehog signalling in prostate regeneration, neoplasia and metastasis. *Nature* 2004; 431:707-712.

116. Sanchez P, Hernandez AM, Stecca B, et al. Inhibition of prostate cancer proliferation by interference with SONIC HEDGEHOG-GLI1 signaling. *Proc Natl Acad Sci U S A* 2004; 101:12561-12566.

117. Sheng T, Li C, Zhang X, et al. Activation of the hedgehog pathway in advanced prostate cancer. *Mol Cancer* 2004; 3:29.

118. Edlund M, Sung SY, Chung LW. Modulation of prostate cancer growth in bone microenvironments. *J Cell Biochem* 2004; 91:686-705.

119. Hsieh CL, Gardner TA, Miao L, et al. Cotargeting tumor and stroma in a novel chimeric tumor model involving the growth of both human prostate cancer and bone stromal cells. *Cancer Gene Ther* 2004; 11:148-155.

120. Feldman BJ, Feldman D. The development of androgen-independent prostate cancer. *Nat Rev Cancer* 2001; 1:34-45.

121. Bamias A, Dimopoulos MA. Thalidomide and immunomodulatory drugs in the treatment of cancer. *Expert Opin Investig Drugs* 2005; 14:45-55.

122. Capitosti SM, Hansen TP, Brown ML. Thalidomide analogues demonstrate dual inhibition of both angiogenesis and prostate cancer. *Bioorg Med Chem* 2004; 12:327-336.

123. Tu SM, Kim J, Pagliaro LC, et al. Therapy tolerance in selected patients with androgen-independent prostate cancer following strontium-89 combined with chemotherapy. *J Clin Oncol* 2005; 23:7904-7910.

124. Kopetz ES, Nelson JB, Carducci MA. Endothelin-1 as a target for therapeutic intervention in prostate cancer. *Invest New Drugs* 2002; 20:173-182.

125. Uehara H, Kim SJ, Karashima T, et al. Effects of blocking platelet-derived growth factor-receptor signaling in a mouse model of experimental prostate cancer bone metastases. *J Natl Cancer Inst* 2003; 95:458-470.

126. Wu JD, Odman A, Higgins LM, et al. In vivo effects of the human type I insulin-like growth factor receptor antibody A12 on androgen-dependent and androgen-independent xenograft human prostate tumors. *Clin Cancer Res* 2005; 11:3065-3074.

127. Mantzoros CS, Tzonou A, Signorello LB, et al. Insulin-like growth factor 1 in relation to prostate cancer and benign prostatic hyperplasia. *Br J Cancer* 1997; 76:1115-1118.

128. Hsieh CL, Chung LW. New prospectives of prostate cancer gene therapy: molecular targets and animal models. *Crit Rev Eukaryot Gene Expr* 2001; 11:77-120.

129. Hsieh CL, Yang L, Miao L, et al. A novel targeting modality to enhance adenoviral replication by vitamin D(3) in androgen-independent human prostate cancer cells and tumors. *Cancer Res* 2002; 62:3084-3092.

Bioconjugated quantum dots for multiplexed and quantitative immunohistochemistry

Yun Xing[1], Qaiser Chaudry[2], Christopher Shen[1], Koon Yin Kong[2], Haiyen E Zhau[3], Leland W Chung[3], John A Petros[3,4], Ruth M O'Regan[5], Maksym V Yezhelyev[5], Jonathan W Simons[1,5], May D Wang[1,2,5] & Shuming Nie[1,5]

[1]Department of Biomedical Engineering, Emory University and Georgia Institute of Technology, 101 Woodruff Circle Suite 1001, Atlanta, Georgia 30322, USA. [2]Department of Electrical and Computer Engineering, Georgia Institute of Technology, Atlanta, Georgia 30332, USA. [3]Department of Urology, Emory University School of Medicine, Atlanta, Georgia 30322, USA. [4]Veteran Affairs Medical Center, Atlanta, Georgia, 30333, USA. [5]Department of Hematology and Oncology and the Winship Cancer Institute, Emory University School of Medicine, Atlanta, Georgia 30322, USA. Correspondence should be addressed to M.D.W. (maywang@bme.gatech.edu) or S.N. (snie@emory.edu).

Bioconjugated quantum dots (QDs) provide a new class of biological labels for evaluating biomolecular signatures (biomarkers) on intact cells and tissue specimens. In particular, the use of multicolor QD probes in immunohistochemistry is considered one of the most important and clinically relevant applications. At present, however, clinical applications of QD-based immunohistochemistry have achieved only limited success. A major bottleneck is the lack of robust protocols to define the key parameters and steps. Here, we describe our recent experience, preliminary results and detailed protocols for QD–antibody conjugation, tissue specimen preparation, multicolor QD staining, image processing and biomarker quantification. The results demonstrate that bioconjugated QDs can be used for multiplexed profiling of molecular biomarkers, and ultimately for correlation with disease progression and response to therapy. In general, QD bioconjugation is completed within 1 day, and multiplexed molecular profiling takes 1–3 days depending on the number of biomarkers and QD probes used.

INTRODUCTION

QDs are tiny light-emitting particles on the nanometer scale, and are emerging as a new class of fluorescent labels for biology and medicine[1–11]. In comparison with organic dyes and fluorescent proteins, QDs have unique optical and electronic properties such as size-tunable light emission, superior signal brightness, resistance to photobleaching and simultaneous excitation of multiple fluorescence colors. These properties are most promising for improving the sensitivity and multiplexing capabilities of molecular histopathology and disease diagnosis. Recent advances have led to highly bright and stable QD probes that are well suited for profiling genetic and protein biomarkers in intact cells and clinical tissue specimens[12–14]. In contrast to *in vivo* imaging applications where the potential toxicity of cadmium-containing QDs is a major concern, immunohistological staining is performed on *in vitro* or *ex vivo* clinical patient samples. As a result, the use of multicolor QD probes in immunohistochemistry (IHC) is likely one of the most important and clinically relevant applications in the near term.

In recent years, several groups have used QD probes for fluorescence immunostaining of fixed cells and tissue specimens[15–21]. However, medical applications of QD-based immunohistochemistry have not achieved widespread adaptation or significant clinical success. A major problem is the lack of robust protocols and experimental procedures to define the key factors and steps involved in QD immunohistochemical staining and data analysis. In particular, there are no consensuses on methods for QD–antibody (QD–Ab) bioconjugation, tissue specimen preparation, multicolor QD staining, image processing and data quantification. Faced with these needs, we have developed antibody-conjugated QDs for multiplexed and quantitative (or semi-quantitative) IHC, and have achieved five-color molecular profiling on formalin-fixed and paraffin-embedded (FFPE) clinical tissue

specimens. We have also optimized the experimental procedures for QD bioconjugation, tissue specimen preparation, multicolor staining, image processing and analysis, and biomarker quantification[6,12–14].

In this paper, we describe our recent experience, preliminary results and detailed experimental procedures. We also discuss the development of QD–Ab conjugates for quantitative and multiplexed IHC, an important but challenging goal that has not been achieved for diagnostic pathology. In contrast to standard hematoxylin and eosin tissue staining, multicolor QD staining allows the use of one antibody-QD conjugate to target a housekeeping gene product, thus providing an internal standard for signal calibration and quantification. This "ratiometric" staining approach to IHC can overcome many problems encountered with traditional methods[22]. In addition to clinical pathology, we envision that sensitive QD-based immunoassays represent a new direction for multiplexed detection of category A bioterrorism agents such as anthrax, plaque, botulism and viral hemorrhagic fevers[23].

The procedure

A flowchart of the procedure with timing information is shown in **Figure 1**. Detailed protocols for QD–Ab conjugation (part 1) and for QD staining of cellular or tissue specimens (part 2) are given in the PROCEDURE section, followed by a discussion of imaging data acquisition, processing and analysis (part 3). A software tool for quantitative IHC (called Q-IHC) is given in **Box 1** and **Figure 2**. In addition, excellent protocols have been published for QD conjugation to luciferase (self-illuminating QDs)[24], QD–protein conjugation via dihydrolipoic acid and non-covalent self-assembly[25], and using bioconjugated QDs for tracking the motion of membrane molecules[26].

QD bioconjugation

As schematically illustrated in **Figure 3**, QD conjugation to biomolecules can be carried out by electrostatic binding, noncovalent biotin–avidin binding, direct covalent crosslinking and nickel-based histidine tagging. Mattoussi and co-workers[25,27] were the first to use an adaptor or fusion protein for IgG antibody coupling based on electrostatic interactions. The adaptor protein has a positively charged leucine zipper domain for electrostatic binding to QDs and a protein G domain for binding to the antibody Fc region. Using such a "bifunctional" adaptor, the Fc end of the antibody is connected to the QD surface, with the target-specific $F(ab')_2$ domains facing outward. For histidine-tagged peptides or antibodies, it is also possible to use the nickelnitrilotriacetic acid complex (Ni-NTA) as a bifunctional adaptor for QD bioconjugation. In this case, the nitriloacetic acid group is covalently linked to the QD encapsulation polymer whereas histidine-tagged antibodies bind to nickel ions (Ni^{2+}) by chelation. In comparison with biotin–avidin binding, this "his-tag" method has several advantages such as a controlled orientation of the binding ligand (a histidine tag can be conveniently fused to proteins and peptides at a particular site), compact overall probe sizes and low production costs. Although the stability of the histidine–nickel attachment could be a problem under the harsh conditions of immunohistochemical staining, previous research has shown that the interaction of $6\times$ His with Ni-NTA is virtually unaffected by high salt (up to 1 M), nonionic detergents (Triton X-100 or Tween 20 up to 1%, w/w), organic solvents, ethanol or glycerol to 30%, reducing agents (β-mercaptoethanol up to 10 mM) (see ref. 28) or highly denaturing conditions such as 8 M urea or 6 M guanidine hydrochloride[29]. Based on the 6-histidine epitope, we have not encountered major stability problems for the bioconjugated QDs in PBS buffer at room temperature (RT) for a period of 2–3 weeks at 4 °C.

Covalent QD conjugation is most commonly based on crosslinking reactions between amine and carboxylic acid groups (catalyzed by carbodiimide) (Step 1C), between amine and sulfhydryl groups (catalyzed by maleimide) (Step 1A) or between aldehyde and hydrazide functions. An advantage of the amine–carboxylic acid crosslinking method is that most proteins contain primary amine and carboxylic acid groups, and do not need chemical modifications before QD conjugation. In contrast, free and accessible sulfhydryl groups are rare in native biomolecules and are often unstable in the presence of oxygen. Another method for covalent conjugation involves oxidizing carbohydrate groups on the antibody's Fc portion to reactive aldehyde groups, which are then covalently linked to QDs (Step 1B). Because the carbohydrate's position is known on the antibody, this approach allows site-specific QD conjugation at relatively simple QD–Ab ratios. The properties and performance of these various QD–Ab conjugates are summarized in **Table 1**. In this contribution, we present four different, detailed methods for preparing QD–Ab conjugates for cell and tissue staining.

Preparation of cell and tissue specimens

To optimize the procedures for specimen preparation, we have studied and compared fresh cells, frozen cells (stored at −80 °C), fixed cell pellets, as well as archived patient specimens (FFPE samples). Cells collected fresh from subculture are relatively easy to be stained and often show the best morphologies. For optimal
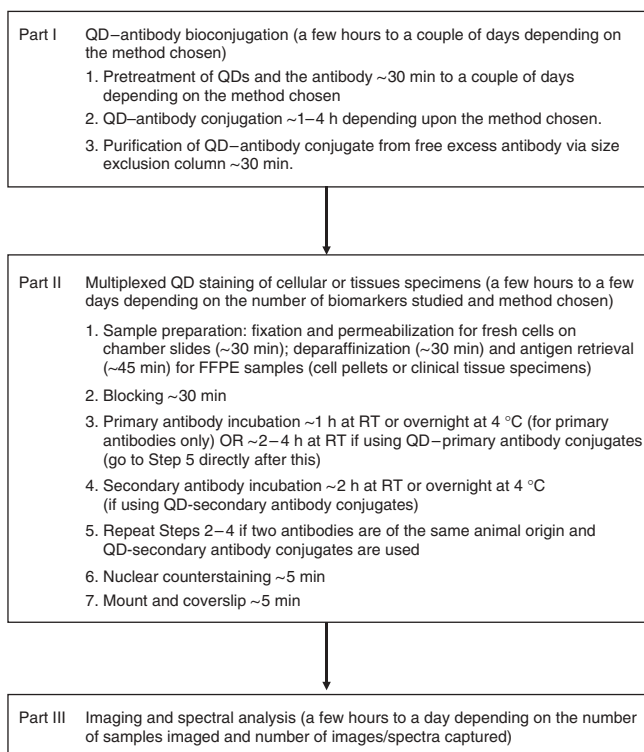
Part I   QD–antibody bioconjugation (a few hours to a couple of days depending on the method chosen)
1. Pretreatment of QDs and the antibody ~30 min to a couple of days depending on the method chosen
2. QD–antibody conjugation ~1–4 h depending upon the method chosen.
3. Purification of QD–antibody conjugate from free excess antibody via size exclusion column ~30 min.

Part II   Multiplexed QD staining of cellular or tissues specimens (a few hours to a few days depending on the number of biomarkers studied and method chosen)
1. Sample preparation: fixation and permeabilization for fresh cells on chamber slides (~30 min); deparaffinization (~30 min) and antigen retrieval (~45 min) for FFPE samples (cell pellets or clinical tissue specimens)
2. Blocking ~30 min
3. Primary antibody incubation ~1 h at RT or overnight at 4 °C (for primary antibodies only) OR ~2–4 h at RT if using QD–primary antibody conjugates (go to Step 5 directly after this)
4. Secondary antibody incubation ~2 h at RT or overnight at 4 °C (if using QD-secondary antibody conjugates)
5. Repeat Steps 2–4 if two antibodies are of the same animal origin and QD-secondary antibody conjugates are used
6. Nuclear counterstaining ~5 min
7. Mount and coverslip ~5 min

Part III   Imaging and spectral analysis (a few hours to a day depending on the number of samples imaged and number of images/spectra captured)

Figure 1 | Flowchart and timing for QD conjugation and immunohisto-chemical staining of cells and tissue specimens.

cell membrane and cytoplasmic staining, however, the fresh cells often need to be fixed and permeabilized. Nuclear staining requires an additional proteinase K treatment step. For frozen cell specimens that are fixed with acetone/methanol before cryo-storage, no permeabilization is needed. For paraffin-embedded tissue specimens, we recommend an antigen retrieval step, as is commonly used in IHC[30]. This step is not always necessary, but antigen retrieval permits stronger staining signals. Typical antigen retrieval methods include heating, protease digestion and treatment under strong acidic conditions[30]. Selection of an antigen retrieval method depends much on the specific primary antibody to be used. We recommend the use of a pressurized cooker for heating (5 min at 120 °C) in citrate (pH 6.0) or EDTA (pH 8.0) buffer. Heating in EDTA buffer often leads to brighter staining signals, and is more suitable for low-abundance antigens or antigens with inaccessible epitopes. However, the pH of the buffers and the heating conditions could be too harsh for some tissue slides and could cause tissues to peel off. For best results, paraffin-mounted tissue specimens should be placed on coated slides (superfrost, positively charged) and baked to adhere firmly to the specimens, before subjecting to further steps of the described protocols. We present detailed procedures for QD staining of three types of samples: cells fresh from subculture (Step 2A), frozen cells samples (Step 2B) and FFPE cell/tissue specimens (Step 2C). Each sample type requires a different pretreatment method before QD staining.

Multicolor QD staining

Depending on the types of QD bioconjugates and the primary antibodies used, multiplexed labeling of cells/tissue specimens can

BOX 1 | Q-IHC - A SOFTWARE TOOL FOR QUANTITATIVE ANALYSIS OF IMMUNOHISTOCHEMICAL DATA

We have developed an integrated image processing and bioinformatics software tool (called Q-IHC) for quantitative analysis of biomarker expression and distribution in immunohistochemical (IHC) images (see **Figure 2**). In comparison to previous image processing software for automated feature extraction and quantitative analysis[50,51], our software system is capable of handling imaging data from both traditional and QD-based IHC. To measure the distribution of labeled antigens, multiple slides of IHC imaging data are acquired to capture selected tissue structures. After image acquisition, an image processing module carries out automatic boundary identification, semi-automatic image segmentation, and color-based tissue classification based on biomarker staining. Then, an image analysis module quantifies the various biomarker features into numerical values. These values become distinct features and are used for comparison with clinical diagnosis. After validation by a physician, the quantitative data and rules describing biomarker features are stored in a database. This semi-automatic image processing and quantification system is designed to provide molecular profiling data that are more objective, more consistent, and more reproducible than completely manual or automated quantification methods. Our software tools process image files from slide scanners in Matlab, which is a collection of various engineering processing tools. We have designed a user-friendly graphical user interface that allows users to give input and feedback to improve the system quality.

The Q-IHC tool is available to academic and nonprofit research institutions from the Emory-Georgia Tech Center of Cancer Nanotechnology Excellence, funded by the National Cancer Institute (NCI), the Georgia Cancer Coalition (GCC), the Georgia Research Alliance (GRA), Emory University, and Georgia Institute of Technology. For further information on software download and deployment, go to: http://www.bio-miblab.org. Correspondence and requests concerning image analysis and biocomputing should be addressed to Dr. May D. Wang, Department of Biomedical Engineering, Georgia Tech and Emory University, 313 Ferst Drive, UA Whitaker Building 4106, Atlanta, Georgia 30332, USA, email address: maywang@bme.gatech.edu.

be achieved by either direct or indirect staining procedures. For direct staining, each primary antibody is conjugated to a QD of a different color, and a mixture of several different QD–Ab conjugates is applied to the tissue specimen in a single step (Step 3B). Although this method is fast and efficient, some primary antibodies may not survive the QD conjugation process and their binding properties are likely altered by covalent modifications at either -NH$_2$ or -COOH sites. Also, QD conjugation to primary antibodies does not work well when the original antibody buffer contains bovine serum albumin (BSA) or other culture medium proteins. Further, the reagents costs could become considerably high because each primary antibody is conjugated to just one type of QD, and none of the QD bioconjugates could

be used as a common reagent for staining of antigen or antibody classes.

These problems can be addressed by indirect QD staining, in which QD–secondary antibody conjugates are used to recognize primary antibodies (unlabeled) (Step 3A). The main advantages of this method are its flexibility, lower costs and the reduced constraint on primary antibodies. A typical multicolor labeling procedure would involve the following steps: blocking → 1st set of primary antibodies (each raised from a different animal species) → 1st QD–secondary antibody conjugates (each against a different animal species) → blocking → 2nd set of primary antibodies → 2nd set of secondary antibodies → so on. Despite these multiple blocking/staining/washing steps, we have achieved excellent results for five-color molecular profiling of cancer cells and tissue specimens (see below). It should be emphasized that careful control studies must be planned and included for data validation and interpretation. For QD–primary antibody conjugates, a negative control experiment is to saturate the antigens with isotype- and species-matched immunoglobulin molecules before QD staining. Additional controls should include the use of free QDs or BSA-QD conjugates to evaluate nonspecific binding and staining. For QD–secondary antibody conjugates, one key control is to determine the level of nonspecific binding when the primary antibody is purposely omitted from the staining protocols. For multiplexing purposes (Step 3C), QD–primary antibody conjugates will be the best choice. However, some antibodies may not be suitable for chemical modification. In these cases, QD–secondary antibody conjugates can be used instead. In the following, we present detailed procedures for both types of conjugates.

Imaging data acquisition, processing, and analysis
In our laboratory, true-color fluorescence images are obtained by using an Olympus IX70 epifluorescence microscope equipped with
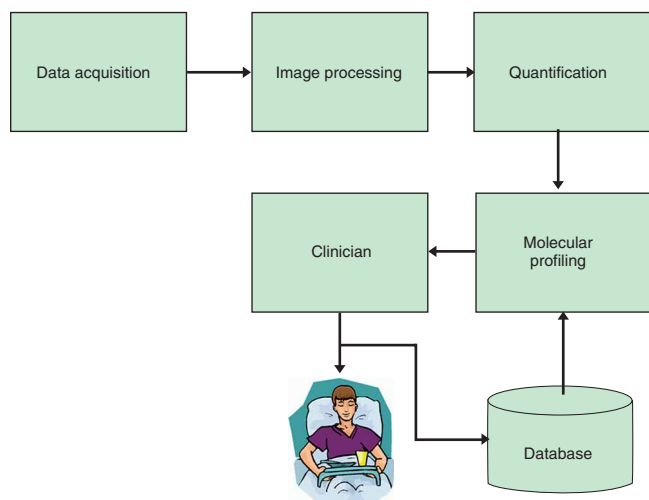

Figure 2 | Block diagram of Q-IHC, an integrated software system for image processing and biomarker quantification of immunohistochemical data.

a long-pass filter, a mercury lamp, and a digital color CCD camera. Fluorescence spectroscopy is carried out by attaching a spectrometer to the microscope side port. By using objectives with different magnifications (zooming in and out), this microspectroscopic system allows one to acquire wavelength-resolved spectra from an individual cell as well as from a cluster of cells. At high magnifications (e.g., 100×), the spectra provide information on individual cells, while at low magnifications (2×, 10×), the spectra provide averaged signals for 10–100 cells. For data calibration, we calculate the average signal intensities (e.g., 40×10^3 arbitrary fluorescence units) for cell lines with over-expressed antigens (e.g., breast cancer cells with over-expressed Her2). Then we set this value as 100% and calculate the signal intensities of other cell lines as a percentage from this maximum. For clinical tissue specimens, we similarly measure the fluorescence intensity from a series of samples with the highest Her2 expression. This intensity is set as 100% and is used for further calculations. To ensure statistical validity, multiple spectra (30–50) of representative regions are taken and are averaged in the analysis.

Image segmentation. For segmentation of cell and tissue images, we have developed level-set algorithms using partial differential equations (PDEs) for identification of cellular regions versus non-cellular regions. The algorithms are independent of the initial conditions, and can automatically select the cell-region boundaries. For identification of special tissue structures, such as a prostate gland, we have developed a semiautomatic method that provides more user control for monitoring segmentation accuracy and sensitivity. Specifically, we developed a custom Graphics User Interface (GUI) based on the intelligent scissor (IS) algorithm[31,32]. This graphics interface allows the user to control the quantification process because the user often has *a priori* knowledge of staining color and biomarker locations (i.e., cell nucleus, cell membrane, cytoplasm, or the extracellular matrix). The user can start the segmentation process by moving the mouse cursor to a "region of interest" (ROI) such as an isolated cancer cell or a prostate gland, and then mark this region with a few "seed" points (user-selected points to delineate cell or gland boundaries). Then, the image processing system interactively computes multiple paths from the user-selected points to other neighboring points in the image, and extracts features such as edges (discontinuity in color or intensity) or areas (regions sharing similar textures). The one path that provides the optimal feature extraction is the solution. As one
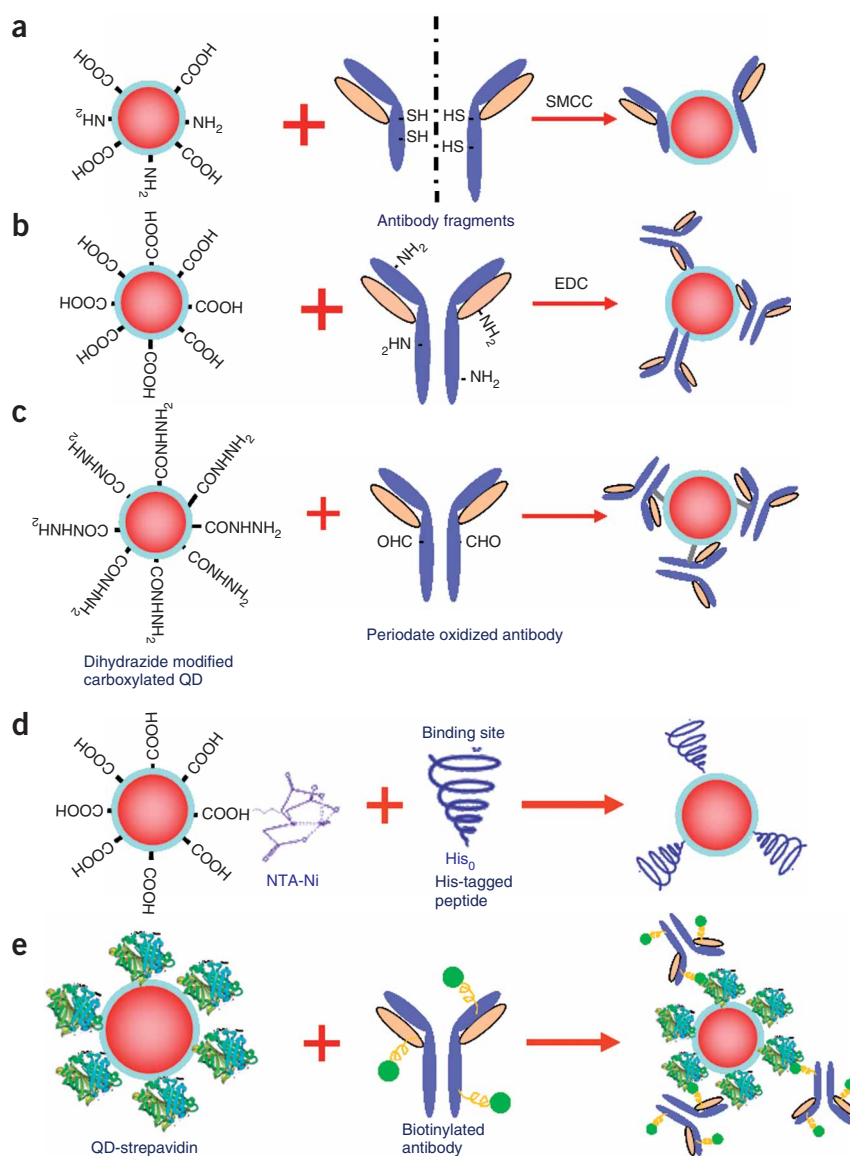

Figure 3 | Schematic diagrams showing various methods for QD-antibody (QD-Ab) bioconjugation. (**a**) QD conjugation to antibody fragments via disulphide reduction and sulfhydryl-amine coupling; (**b**) covalent coupling between carboxylic acid (-COOH) coated QDs and primary amines (-NH₂) on intact antibodies using EDAC as a catalyst; (**c**) site-directed conjugation via oxidized carbohydrate groups on the antibody Fc portion and covalent reactions with hydrazide-modified QDs; (**d**) conjugation of histidine-tagged peptides or antibodies to Ni-NTA modified QDs; and (**e**) noncovalent conjugation of streptavidin-coated QDs to biotinylated antibodies.

example, **Figure 4** shows traditional IHC images of prostate tissue specimens in which features are extracted from the edges separating the pocket-shaped gland structure from other areas. The user can pick a starting "seed" by moving the mouse cursor to the top of one gland. As the mouse is placed by the user along one side of the gland, the image processing system will compute the connection from the "seed" point to all neighboring points. Multiple connecting paths will be generated, with the optimal path being labeled or highlighted in green color. This calculation occurs interactively in real time.

High computing efficiencies are achieved by using the optimal spanning tree based on Dijkstra's graph searching algorithm[33]. This

TABLE 1 | Methods for QD bioconjugation, conjugate chararacteristcs and comparative performance for immunohistochemical staining.

Conjugation method	Sulfhydryl (covalent)	Amide (covalent)	Fc-sugar (covalent)	His-tag (noncovalent)	Biotin–avidin (noncovalent)
Conjugated ligand	Ab fragments	Whole Ab	Whole Ab	ScFv or Peptide	Whole Ab
Site specificity	Yes	No	Yes	Yes	No
Ligand orientation	Fixed	Random	Fixed	Fixed	Random or fixed[a]
Ab/QD ratio[b]	~4	~15	~15	~3–25	<3
Staining specificity	Medium	Low	Medium	High	High
Staining brightness	Low	High	Very high	High	Medium
Background noise	Low	Medium	Low	Low	Low
Special conditions	Protein-free buffer	None	Carbohydrate	None	None
Reagent costs	Medium	Low	Medium	High	High
Overall performance	Fair	Poor	Excellent	Excellent	Good

Notes: the data were derived from the authors' laboratories at Emory University School of Medicine and Georgia Institute of Technology. Probe comparisons were made under identical experimental conditions. Performance evaluations were based on a number of parameters such as level of nonspecific staining, background noise and specific signal brightness. All QD-Ab conjugates are stable for 2–4 weeks at 4 °C.
[a]The orientation can be random or fixed based on the biotinylation method. [b]These are approximate estimates based on the number of functional groups on the QD and the molar ratio of starting materials under the assumption that 50% of the starting antibody molecules are conjugated to QDs. The actual number of antibodies per QD could vary depending on the reaction conditions.

search algorithm treats the image as a weighted graph. Each pixel represents a node with directed and weighted edges that connect with its eight adjacent neighbors. As the mouse cursor moves, the optimal path from the pointer position to the seed point is displayed. This path allows the user to select an optimal contour segment that visually corresponds to a portion of the desired object boundary. As the mouse cursor moves, the optimal path from the pointer position to the "seed" point is calculated. When the mouse pointer comes in proximity to an object edge, a live wire boundary snaps to and wraps around the object of interest[31,32], as highlighted in red contour color in **Figure 4**. If the user finds the contour segment visually corresponds to a portion of the desired object boundary, double clicking the mouse fixes the contour and changes its color to green. This design enables the user to play a part in the process of computer-based contour feature extraction, leading to more reliable and more repeatable results. After the cellular and tissue shapes are identified by image segmentation, further data analysis will only focus on ROIs. The key next step is to classify each pixel to a biomarker or to the background by using K-means clustering[34].

K-means clustering. In addition to determining the staining intensity of biomarkers, it is important to know the location of biomarkers in an ROI, especially for multiplex-QD labeled cell and tissue specimens. We have used the K-means algorithm because it has three distinctive advantages: (a) no requirement for human interaction, (b) ease of implementation, and (c) high performance. K-means is a widely used technique for clustering of multi-spectral data[34], and is based on the sum of least squares criterion. For example, in two-color QD staining of prostate cancer tissues, we can define each color of the biomarker and the background as one cluster. For k-1 biomarker and the background, the first step is to define k centroids (center positions), one for each cluster. These centroids may be initialized by predefined values, or may be placed far away from each other to avoid local minima convergence. The next step is to take each point belonging to a given data set and associate it to the nearest centroid. When this initial grouping is
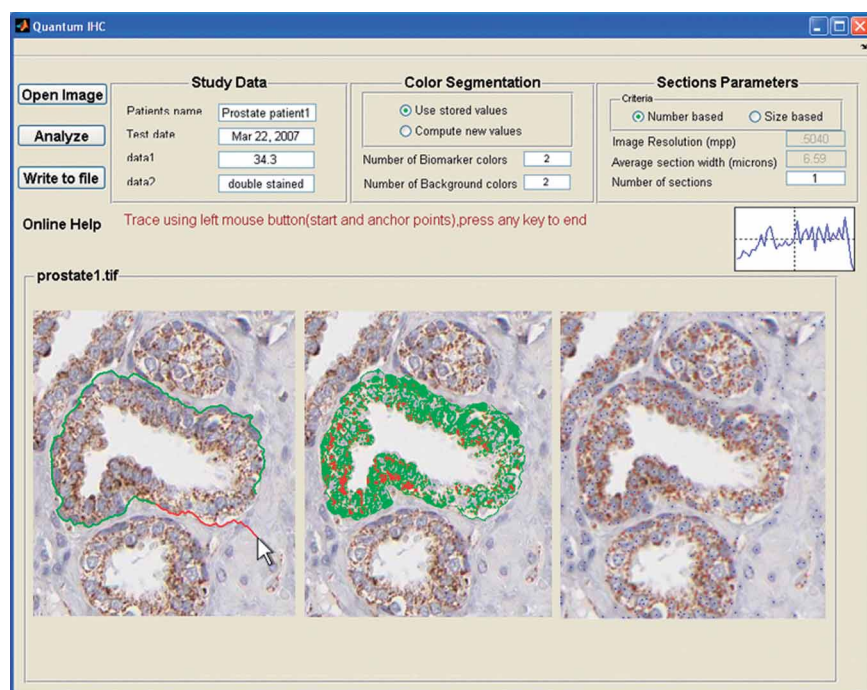

Figure 4 | Computer screen showing prostate tissue specimens stained with traditional IHC and the graphical interface for image analysis and biomarker quantification. Left panel: the user can pick a starting "seed" by moving the mouse to the top of one prostate gland. As the mouse is placed by the user along one side of the gland, the image processing system will compute the connection from this "seed" point to all neighboring points. Multiple possible connecting paths will be generated, and then the optimal path will be labeled (i.e., highlighted in green color edge). This calculation occurs interactively in real time. Middle panel: the use of K-means clustering to segment QD-stained tissue images, with cellular structures being highlighted by light green and light red colors. Right panel: automated counting of brown staining cells (red dots) and blue-staining cells (blue dots). The IHC images openly available from the Human Proteome Organization (HUPO) are used in this analysis, demonstrating the broad utility of our software system. Detailed staining information: antibody CAB002311, protein EnsEMBL ID: ENSP00000304146, netrin receptor DCC precursor in prostate tissue; see http://www.proteinatlas.org.

done, we need to recalculate k new centroids of the clusters resulting from the previous step. After we have these k new centroids, a new binding is established between the same data set points and the nearest new centroids. During this iterative process, the k centroids keep changing their locations step by step until they are stabilized (that is, the k centroid positions no longer move or change). During this iterative process, the algorithm aims to minimize an objective function, in this case a squared error function:

$$J = \sum_{j=1}^{k} \sum_{i=1}^{n} \left\| x_i^{(j)} - c_j \right\|^2$$

where $\left\| x_i^{(j)} - c_j \right\|^2$ is a chosen distance between a data point $x_i^{(j)}$ and the cluster center c_j, and is an indicator of the distance of n data points from their respective cluster centers. This K-means color segmentation can be used for both traditional IHC (**Figure 4**) and QD-IHC (**Figure 5**) to quantify biomarkers and background, and also to count cells.

Figure 5 shows an example of using two-color QD probes to stain two biomarkers (p53 and EGR-1) in prostate cancer tissues, together with the detection of blue fluorescence as the tissue background. The ROIs are identified by using 3-means (k = 3), and are highlighted in red (p53), green (EGR-1), and blue (background). The three clusters are combined together to show the distribution of each biomarker and the background.

A potential problem of the K-means algorithm is that it may converge to a local minimum instead of the optimal global solution. Thus, additional features are added to make the algorithm robust and adaptable to significant variations in staining densities and lighting conditions: (i) to allow the user (if required) to initialize the clustering algorithm by manually marking starting seed points; and (ii) to allow the user to select the specific type of staining and the number of biomarkers. As a result, our K-means algorithm is able to process traditional IHC as well as multiplexed QD stained slides on the same platform. It can also detect different types of staining color themes (e.g., brown-colored staining in standard IHC and orange-colored fluorescence in QD staining).

| p53 655 nm ▮ | EGR-1 565 nm ▮ | Auto fluorescence ▮ |

Figure 5 | Multiplexed QD IHC images of clinical FFPE (formalin fixed, paraffin embedded) prostate tissue specimens, and quantitative analysis of cancer biomarkers and tissue background fluorescence. The fluorescence images were obtained with UV excitation, with the p53 marker stained red with QD655, the EGR-1 marker stained green with QD565, and the tissue background observed as blue. The color maps show the location where a biomarker (or the tissue background) is more pronounced than others. (**a**) Original multicolor image; (**b**) p53 protein (red); (**c**) EGR-1 protein (green); (**d**) tissue background fluorescence (blue); (**e**) combined map of dominant markers and background; and (**f**) automated boundary segmentation using level-set algorithms.

Data quantification. Because the amount of biomarker in the tissue is proportional to the amount of staining, and because the fluorescence intensity (or optical density) is proportional to the amount of staining, it is possible to quantify biomarker expressions by fluorescence intensity or optical density measurements. For this purpose, the biomarkers detected during the image processing are converted into numeric values. Key parameters are extracted such as biomarker staining intensities, background intensities, and the relationship of biomarker to background areas (this relative value is used to alleviate potential biases introduced by absolute numbers). These parameters pertaining to the complete ROI as well as each subsection are stored in a database. Analysis and classification of these parameters can provide information on the molecular anatomy of normal and diseased cells. For clinical outcome studies, the biomarker expression profiles are correlated with datasets that are already validated and stored in a database.

MATERIALS
REAGENTS
- Antibodies: E-cadherin (Santa Cruz Biotechnology, cat. no. sc7870), N-cadherin (Abcam, cat. no. ab12221), vimentin (Santa Cruz Biotechnology, cat. no. sc6360), EF1alpha (Upstate, cat. no. 05-235) and RANKL (Santa Cruz Biotechnology, cat. no. sc-52951)
- Custom-made CdSe/ZnSe/ZnS QDs with fluorescence emission peaks at 530 and 650 nm (provided by Andrew Smith of Georgia Tech and Emory University)
- QD655 primary antibody conjugation kit (Invitrogen, cat. no. Q2202MP)
- QD655 nanocrystals (amino, 4 μM) (included in the primary antibody conjugation kit; Invitrogen, cat. no. Q2202MP) SMCC (4-(maleimido-methyl)-1-cyclohexanecarboxylic acid N-hydroxysuccinimide ester; included in the primary antibody conjugation kit; Invitrogen, cat. no. Q2202MP) QD nanocrystals (carboxylated, 8 μM) (Invitrogen, cat. no. Q21321MP)
- Dithiothreitol (DTT) (included in the primary antibody conjugation kit; Invitrogen, cat. no. Q2202MP)
- Adipic acid dihydrazide (ADH) (Sigma, cat. no. A0638)
- EDC ((N-(3-dimethylaminopropyl)-N′-ethylcarbodiimide hydrochloride; Fluka, cat. no. 03450)
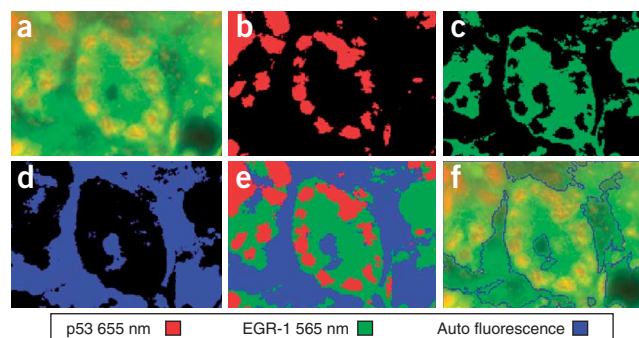
- Dialysis tubing (MWCO: 50 kDa, Spectral Laboratories, cat. no. 132128)
- Sodium periodate (Pierce, cat. no. 20504)
- PBS buffer (10×, pH 7.2) (VWR, cat. no. EM6507)
- NHS (N-hydroxysuccinimide; Pierce, cat. no. 24500)
- Methanol (Sigma, cat. no. 179337)
- QD–streptavidin nanocrystals (1 μM) (Invitrogen, cat. no. Q10121MP)
- Biotin-LC-hydrazide for size-directed biotinylation (Pierce, cat. no. 21340)
- NHS-PEO-biotin for random biotinylation (Pierce, cat. no. 21330).
- Triblock copolymer consisting of a poly-butylacrylate segment, a poly-ethylacrylate segment and a poly-methacrylic acid segment (see details below) (Sigma, MW = 100 kDa)
- Deionized (DI) water (18 MΩ) (Millipore Milli-Q, CDOF01205)
- Normal goat serum (Vector Laboratories, cat. no. S-1000)
- BSA (Sigma, cat. no. A2153)
- DAPI nuclear stain (Sigma, cat. no. D9564)
- Mounting media (Biomeda, gel-mount, cat. no. M-01)
EQUIPMENT
- NAP-5 columns (GE Healthcare, cat. no. 17-0853-01)
- Gel filtration columns (Pierce, cat. no. 29920)
- Superdex 200 media (GE Healthcare, cat. no.17-1043-10)

- Syringe and plastic tubing (included in the Invitrogen primary antibody conjugation kit)
- Stand and racks to hold the columns upright (Fisher, cat. no. 14-809-136 and 03-448-17)
- Centrifuge tubes (1.5 ml; VWR, cat. no. 87003-290)
- Non-stick centrifuge tips (1.5 ml; VWR, cat. no. 20170-650)
- Hydrophobic pen ▲ CRITICAL Not all hydrophobic pens used in IHC would work for QD staining; some of them may contain organic solvents that may "quench" QDs. According to our experience, try to stick with the ImmunoEdge pen from Vector Laboratories.
- Concentrator (MWCO: 50 kDa) (Millipore, cat. no. 42415)
- Pipettors (Corning Lambda, cat. nos. CRSC001, CRSC003, CRSC005 and CRSC006)
- Pipette tips (Fisher Scientific, cat. no. 02-707-136; VWR, cat. nos. 53508-810 and 83007-376)
- Transfer pipette (Fisher Scientific, cat. no. 13-711-7)
- Staining jar (VWR, cat. no. 25460-00)
- Lab-tek chamber slide system (sterile) (VWR, cat. no. 62407-296)
- Coverslips (VWR, cat. no. 48404-454)
- 3-D rotator (Lab-line, cat no. 4630)
- UV/Vis spectrometer (Shimadzu UV-2401 PC)
- Fluorescence spectrometer (Roper Scientific, model SpectraPro 150)
- UV lamp (VWR, UVP/UVL-56)
- Centrifuge machine (VWR, C0175-VWR)
- Pressure cooker and steamer (DAKO, model S2800)
- Epifluorescence microscope (Olympus, model IX70)
- Spectral imaging microscope (CRI Inc., Nuance System with liquid crystal tunable filter tuning between 400 and 720 nm)
- Rotating evaporator (Rotavapor R-3000; Buchi Analytical Inc.)

REAGENT SETUP

Amphiphilic block copolymers A triblock copolymer (consisting of a poly-butylacrylate segment, a poly-ethylacrylate segment and a poly-methacrylic acid segment with a molecular mass of approximately 100,000 Da) was chemically modified for surface encapsulation of custom-made and Crystalplex TriLite (ternary alloyed semiconductor) QDs[6]. For this purpose, the original polymer [poly(*tert*-butyl acrylate-*co*-ethyl acrylate-*co*-methacrylic acid), cat. no. 444790, Sigma-Aldrich] dissolved in dimethylformamide is reacted with *n*-octylamine at a polymer/octylamine molar ratio of 1:40, using ethyl-3-dimethyl amino propylcarbodiimide (EDAC, threefold excess of *n*-octylamine) as a crosslinking reagent (reaction conditions: overnight, RT and normal atmosphere). The product yields are generally greater than 90% owing to the high EDAC coupling efficiency in dimethylformamide (determined by a change of the free octylamine band in thin-layer chromatography (use 1:1 mixed $CHCl_3$:MeOH as the mobile phase, and stain for unreacted amines using ninhydrin stain (300 mg ninhydrin dissolved in 100 ml *n*-butanol and 3 ml acetic acid)). The reaction mixture is dried with a ratovap (Rotavapor R-3000, Buchi Analytical Inc.). The resulting oily liquid is precipitated with water and is rinsed with water five times to remove excess EDAC and other by-products. After vacuum drying, the octylamine-grafted polymer is resuspended in an ethanol/chloroform mixture and stored for use.

QD encapsulation and solubilization Using a 3:1 (v/v) chloroform/ethanol solvent mixture, TOPO-capped QDs are encapsulated by the amphiphilic triblock polymer. A polymer-to-QD ratio of 5:10 is used because molecular geometry calculations indicate that at least four polymer molecules would be required to completely encapsulate one QD. Indeed, stable encapsulation (e.g., no aggregation) is not achieved at polymer/dot ratios less than 4:1. After vacuum drying, the encapsulated dots are suspended in a polar solvent (aqueous buffer or ethanol) and purified by gel filtration.

QD activation with EDC/NHS in methanol To 15 μl QDs (8 μM), add 3 μl EDC (2.2 mM in methanol) and 3 μl NHS (4 mM in methanol), followed by another 9 μl methanol, yielding a total volume of 30 μl. Leave this at RT for 30 min.

Antibody biotinylation Site-directed biotinylation is performed using biotin–hydrazide and periodate-oxidized antibodies (detailed procedures are given below) and random biotinylation is performed using NHS-PEO-biotin through amine groups on the antibody (refer to Pierce website for detailed procedures).

Antibody oxidization with sodium periodate (a) Dissolve antibody in 0.01 M sodium phosphate, 0.15 M NaCl, pH 7.2 (final concentration: 10 mg ml^{-1}). (b) Dissolve sodium periodate in water (final: 0.1 M), protect from light; immediately add 100 μl of sodium periodate to 1 ml of the antibody solution (1.5 mg ml^{-1}); mix to dissolve, protect from light. (c) React in the dark for 30 min at RT. (d) Purify by dialysis overnight against PBS (dialysis tubing, MWCO: 50 kDa).

Antibody sample for Step 1A Before an antibody of interest is reduced, it should be purified and formulated in PBS at a concentration of 1 mg ml^{-1}. The antibody solution must be free of blood/serum, ascites and other proteins such as BSA.

EQUIPMENT SETUP

Spectral imaging Wavelength-resolved spectral imaging is carried out by using a spectral imaging system (CRI Inc.), which consists of a optical head that includes a liquid crystal tunable filter (LCTF, with a bandwidth of 20 nm and a scanning wavelength range of 400–720 nm), an optical coupler and a cooled, scientific-grade monochrome CCD camera, along with image acquisition and analysis software. The tunable filter can be automatically stepped in 10-nm increments from 580 to 700 nm while the camera captures images at each wavelength with constant exposure. Overall acquisition time is about 10 s. The 13 resulting TIFF images are loaded into a single data structure in memory, forming a spectral stack with a spectrum at every pixel. With spectral imaging software, small but meaningful spectral differences can be rapidly detected and analyzed.

Quantitative imaging and spectroscopy An inverted Olympus microscope (IX-70) with a broadband light source (ultraviolet 330–385 nm and blue 460–500 nm) and long-pass interference filters (DM 400 and 510, Chroma Tech), plus a digital color camera (Nikon D1) and a single-stage spectrometer (SpectraPro 150, Roper Scientific) are used for quantitative imaging and spectroscopy.

PROCEDURE

Conjugation

1| Conjugate antibody fragments to QDs using one of the four methods: conjugations using SMCC (option A), conjugation of antibodies to QD nanocrystals via oxidized Fc-carbohydrate groups (option B), direct conjugation of antibodies to QD nanocrystals through amine–carboxylic acid coupling (option C) or indirect conjugation of biotinylated antibodies to streptavidin-coated QDs (option D). In option A, disulfide bonds in the hinge region that hold the two heavy chains together are selectively cleaved to create two antibody fragments, each containing free sulfhydryls and an antigen-binding site.

Many immunoglobulin molecules are glycoproteins that can be periodate-oxidized to reactive aldehyde residues (option B). Polyclonal IgG molecules contain carbohydrate in the Fc portion of the molecule. This is sufficiently removed from the antigen-binding sites to allow conjugation to take place through the sugar chains without compromising binding specificity or affinity[35]. Periodate-oxidized antibodies can then be conjugated to hydrazide groups[36]. Carboxylated QDs can be modified with ADH to generate hydrazides on the QD surface[36], which are then conjugated to oxidized antibodies through aldehyde-hydrazide covalent chemistry.

Antibody molecules possess a number of functional groups that are suitable for QD conjugation. Crosslinking reagents can be used to target lysine primary amine and N-terminal amine groups (option C). However, the distribution of these functional groups within the three-dimensional structure of an immunoglobulin molecule is nearly uniform throughout the surface

topology. For this reason, conjugation procedures using these groups often result in random orientation of the antibody in the QD bioconjugates, blocking some antigen-binding sites. In comparison with site-directed conjugation, the random coupling procedures do not place any special requirements on the antibody.

■ PAUSE POINT Once prepared, the QD–Ab conjugates can be stored for about 4–6 weeks. Beyond this storage period, staining still works but the quality is fairly poor. The problem is that most antibodies need to be stored at −20 °C while QD samples at 4 °C. If the QD–Ab conjugates are stored at 4 °C for too long, the antibodies lose binding affinity and specificity.

(A) Conjugation of primary antibody fragments to QDs ● TIMING 2–4 h
  (i) Mix QD with SMCC for 1 h at RT. A 125 µl portion of stock QD solution (4 µM) is mixed with 13.8 mM SMCC, leading to a final concentration of 1 mM SMCC.
  (ii) Remove SMCC via size-exclusion column: remove both the caps of the NAP-5 column to allow as-supplied liquid to elute through; equilibrate gel with 10 ml exchange buffer; cap the bottom of the column while there is still liquid above the gel bed; add the reaction sample to the column; elute the exchange buffer and collect colored elute.
  (iii) Antibody reduction: antibody is reduced with DTT to expose free sulfhydryl groups. Add 6.1 µl DTT to 300 µl antibody (1 mg ml^{-1}) and allow the reaction to proceed for 30 min at RT.
  (iv) Remove DTT via size-exclusion column: add 20 µl of dye-labeled marker (included in the QD655 primary antibody conjugation kit (Invitrogen, cat. no. Q2202MP)) to the reduced solution; pass the solution through NAP-5 column; and collect colored elute.
  (v) Mix activated QD from Step 1A(ii) and reduced antibody from Step 1A(iv) and incubate the reaction for 1 h at RT (20–25 °C).
  (vi) Prepare 10 mM of β-mercaptoethanol stock immediately before use (working concentration should be 100 µM, which corresponds to 10.1 µl of 10 mM β-mercaptoethanol solution for a 1.0 ml reaction solution).
  (vii) Quench the reaction (Step 1A(v)) with β-mercaptoethanol for 30 min at RT.
  (viii) Concentrate down to 20 µl or less with spin filters (MWCO 50 kDa).
  (ix) Separate the QD–Ab conjugates from free antibodies using gel filtration filled with Superdex 200 media. Collect only the first ten drops of the eluted solution once color appears (use UV lamp to help visualize the color) in the column's 'dead space'.
  (x) QD–Ab conjugates are now ready for cell/tissue staining purposes.
      ? TROUBLESHOOTING

(B) Conjugation of antibodies to QD nanocrystals via oxidized Fc-carbohydrate groups ● TIMING 4–6 h, 2 days if dialysis is chosen for purification
  (i) For 1 ml reaction solution, add 12.5 µl QD nanocrystal stock (carboxylated, 8 µM, and yielding a final concentration of 100 nM), 4 µl of 5 mM EDC stock (final concentration is 20 µM) and 5.1 µl ADH solution (dissolved in PBS, 3.2 µg µl^{-1}) (16.4 µg total).
  (ii) Mix well and react for 4 h at RT.
  (iii) Remove excess ADH and EDC by dialysis overnight against 2 liters of PBS (dialysis tubing, MWCO: 50 kDa). (The selection of dialysis over size-exclusion column is a personal preference and is based on available supplies in the laboratory, not for a scientific reason. It is however important to minimize the loss of QDs and antibodies as both reagents are expensive.)
  (iv) Dissolve antibody in 0.01 M sodium phosphate, 0.15 M NaCl, pH 7.2 (final: 10 mg ml^{-1}).
  (v) Dissolve sodium periodate in water (final: 0.1 M) and protect from light by wrapping the reaction tube with aluminum foil or keep the tube in a dark room.
  (vi) Immediately add 100 µl of sodium periodate to 1 ml of the antibody solution (1.5 mg ml^{-1}); mix to dissolve, protect from light as above.
  (vii) React in the dark for 30 min at RT.
  (viii) Purify by dialysis overnight against PBS (dialysis tubing, MWCO: 50 kDa).
  (ix) Mix QD–hydrazide and periodate-oxidized antibody at a QD:antibody molar ratio of 1:30 and react for 2 h at RT.
  (x) Concentrate the reaction solution to 20 µl or less for the next step.
  (xi) Separate the QD–Ab conjugates from free antibodies by gel filtration using Superdex 200 as the media. Collect the first ten drops of colored elute (if QD concentration is too low to be visible, use a UV lamp to illuminate).
      ? TROUBLESHOOTING

(C) Direct conjugation of antibodies to QD nanocrystals through amine–carboxylic acid coupling ● TIMING ~6 h
  (i) Mix activated QDs with antibody (1 mg ml^{-1} in PBS) and react for 4 h at RT; keep the amount of methanol below 4–5% of total reaction volume; QD:antibody molar ratio is ~1:30; final concentration of QD in the reaction should be around 50 nM.
  (ii) Separate QD–Ab conjugates from excess free antibodies via gel filtration using Superdex 200 columns.
  (iii) Measure collected elutes via UV–visible absorption and fluorescence spectroscopy.
      ? TROUBLESHOOTING

(D) Indirect conjugation of biotinylated antibodies to streptavidin-coated QDs ● TIMING 3–4 h
  (i) Mix biotin-LC-hydrazide with oxidized antibody (biotin/antibody molar ratio is 4:1, and the final biotin-hydrazide concentration is 5 mM) and react at RT for 2 h.

(ii) Purify three times using spin filters (MWCO: 50 kDa) (spin at 5,000 r.p.m. and dilute 1:10 with PBS, each time).

(iii) Mix biotinylated antibody with QD–streptavidin (volume ratio: 1:1) and react at RT for 1 h.

(iv) Separate QD–Ab conjugates from free antibodies using gel filtration (Superdex 200). The resulting QD–Ab conjugates are now ready for staining purposes.

2| Prepare cells for staining by following the steps in options A–C for fresh cells from cultures, frozen cells and FFPE tissues, respectively.

(A) Fresh cells from cultures ● TIMING 1–2 h

(i) Culture cells in multiwell chamber slides overnight or 2 days till they reach about 50–80% confluency.

(ii) Aspirate off media with transfer pippets.

! CAUTION Avoid using motorized pipettors as this will cause cell wash-off owing to the high shear stress.

(iii) Wash with PBS briefly.

(iv) Fix and permeabilize with 3.7% formaldehyde/0.1% Triton X-100/PBS for 20 min at RT.

(v) Wash with PBS three times, each for 5 min.

(vi) (Optional, for nuclear staining only) Incubate with proteinase K (30 μg ml^{-1} in SDS) for 45 min to 1 h at 37 °C.

! CAUTION We note that the use of proteinase K can cause problems because this enzyme nonspecifically cuts all proteins (including the antigens of interest). This problem can be alleviated by controlling the proteinase concentration and the time of incubation. For nuclear antigens, we have not experienced major problems. It is likely that proteinase K degrades intracellular matrix proteins and opens up the nuclear envelope, but does not cause significant damage to antigens in the nuclei if the incubation time is relatively short (45 min to 1 h). However, adequate controls for the presence of antigen epitopes (e.g., by extraction immunoblotting before and after proteinase K treatment) are still necessary. This is especially true for archival FFPF tissues, which may present a range of different fixation conditions and may be differentially susceptible to proteinase digestion.

(B) Frozen cells ● TIMING 0.5–1 h

(i) Remove cell chamber slides from −80 °C freezer (frozen cells can be prepared by fixing the cells in ice-cold acetone for 20 min at −20 °C before transferring to −80 °C freezer).

(ii) Thaw (leave the cell chamber at RT and wait till it warms up).

(iii) Wash with PBS 2–3 times.

(C) FFPE tissues ● TIMING 1–2 h

(i) Deparaffinize by immersing the slides in xylene for 5 min (repeat three times).

(ii) Dehydrate in 100% ethanol for 2 min (repeat twice), 2 min in 95% ethanol (repeat twice) and 2 min in 75% ethanol (repeat twice).

(iii) Rinse with DI water for 2 min.

(iv) Perform an antigen retrieval step (by heat). Some antigens may require other methods such as proteinase K treatment. Pressure-cook (DAKO) or steam for 40 min; use citrate buffer (pH 6.0) for antigens with high abundance; use EDTA buffer (pH 8.0) for low-abundance antigens.

! CAUTION When using EDTA buffer, make sure tissue sections are on superfrost or positively charged slides; otherwise, tissue will float off slide during antigen retrieval.

(v) Cool for 20 min.

(vi) Wash with PBS three times, 5 min each.

3| Stain the cells using antibody conjugates. The procedure will depend on whether you are using QD–secondary antibody conjugates (option A), QD–primary antibody conjugates (option B) or multiplexed QD staining on FFPE samples (option C).

(A) Using QD–secondary antibody conjugates ● TIMING 4–6 h for one set of biomarkers (a "set" is defined as containing antibodies from different animal species)

(i) Block with 2% BSA/5% goat (or rabbit) serum/PBS for 30 min at RT.

▲ CRITICAL STEP Blocking serum needs to be of the same animal origin as the secondary IgG.

(ii) Incubate the first set of primary antibodies (2–10 μg ml^{-1} in blocking buffer) for 1 h at RT.

(iii) Wash with PBS three times, 5 min each. Incubate the first set of QD–secondary antibodies (20 nM in 2% BSA/PBS solution) for 2 h at RT or overnight at 4 °C.

(iv) Wash with PBS vigorously three times, 5 min each.

(v) Repeat Steps (i)–(iii) for additional sets of biomarkers.

(vi) Wash with PBS three times, 5 min each.

(vii) Counterstain cell nuclei with DAPI (100 ng ml^{-1} in water) for 5 min, then wash with DI water for 5 min.

(viii) Mount and coverslip. Store in dark at 4 °C before microscopic viewing.

> **! CAUTION** If cross-contamination is a problem during successive rounds of antibody staining, this problem can be alleviated by incubating the samples with unlabeled secondary IgGs to saturate the unbound binding sites before incubation with the subsequent set of primary antibodies.
>
> **? TROUBLESHOOTING**

(B) Using QD–primary antibody conjugates ● TIMING 3–5 h

(i) Block with 10% horse serum for 30 min at RT.

(ii) Incubate with QD–primary antibody conjugates: (a) membrane antigen: 20–30 nM, 2 h at RT; (b) nuclear antigen: 40–60 nM, 4 h at RT. Pause for thoughts: one potential limitation is that the nuclear antigens might not be accessible to staining by large QD probes. In our hands, we did not see significant differences among 655, 605 and 565 nm QDs for nuclear staining. Theoretically, one would prefer smaller QDs for nuclear staining, but practically we have not found much difference. The reason is perhaps that our tissue specimens are cut and that the nuclear antigens are exposed for antibody binding. For deeper QD tissue penetration, we have used detergents to good effect.

(iii) Wash with PBS three times, 5 min each.

(iv) Nuclear counterstaining: (a) cell nuclei can be stained with DAPI (100 ng ml^{-1} in water) for 5 min; (b) wash with DI water for 5 min.

(v) Mount and coverslip. Store in dark at 4 °C before microscopic viewing.

> **? TROUBLESHOOTING**

(C) Multiplexed QD staining on FFPE samples ● TIMING overnight

(i) Draw a circle around the tissue section with a hydrophobic pen; this is to minimize the amount of reagents in the following steps.

(ii) Block with 2% BSA/5% goat serum/PBS for 30 min at RT.

(iii) Incubate primary antibodies for 1 h at RT or overnight at 4 °C, depending on the affinity of the antibody.

(iv) Wash with PBS three times, 5 min each.

(v) Incubate QD–secondary antibody conjugates overnight at 4 °C.

> **▲ CRITICAL STEP** Overnight at 4 °C always works, 2 h at RT may also work for some antigens; but 1 h at RT is usually not sufficient. We note that the antibody quality (i.e., binding affinity and specificity) plays a major role in determining QD staining success or failure. For example, the antibodies from US Biological should be incubated for at least 30 min at RT for nuclear antigen staining even in traditional IHC. When conjugated to QDs, we see nuclear staining after 1 h at RT, but more "gentle" and complete antigen binding is achieved after overnight incubation at 4 °C.

(vi) Wash with PBS vigorously for three times, 5 min each.

(vii) Counterstain with DAPI (100 ng ml^{-1}) for 5 min at RT.

(viii) Wash with DI water at RT for 5 min.

(ix) Mount with gel-mount (aqueous media) and coverslip.

(x) Place slides in the slide-holder and store at 4 °C.

> **? TROUBLESHOOTING**

? TROUBLESHOOTING

Step 1A
Unsuccessful conjugation is often due to the presence of other disulfide-containing molecules in the antibody medium or buffer. QD conjugation should be confirmed by running agarose or PAGE gels showing size differences between conjugated and unconjugated antibodies and QDs.

Step 1B
Aggregate formation: EDC/ADH concentration too high; unsuccessful conjugation: antibody does not contain sugar group (e.g., some monoclonal antibodies). Successful conjugation should be confirmed by running agarose or PAGE gels showing size changes.

Step 1C
Aggregate formation: QD concentration too high or too much EDC. Successful conjugation should be confirmed by running agarose or PAGE gels.

Steps 3A–C
First, check the quality of QD–Ab conjugates by spreading a small drop on a coverslip and examining it under a fluorescence microscope. Some conjugates may contain aggregates owing to inappropriate handling or storage. It should be noted, however, that even new samples of QD–IgG conjugates from commercial sources could contain lots of aggregates. Check the slides under a microscope after each QD staining step; if there is too much staining, reduce the amount of primary antibody or QD–secondary antibody; if no staining or staining is too weak, increase the antibody concentrations or incubation time.
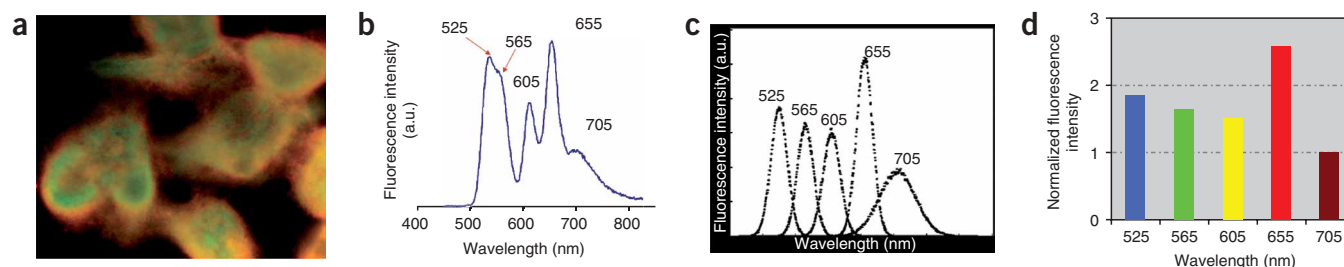
Figure 6 | Multicolor QD staining of human prostate cancer cells, and biomarker normalization using a housekeeping gene product as the internal reference. (**a**) Color fluorescence image of prostate cancer cells stained with five different QDs: QD525 staining vimentin; QD565 staining N-cadherin; QD605 staining RANKL; QD655 staining E-cadherin; and QD705 staining the housekeeping gene product (elongation factor-1α). (**b**) Raw wavelength-resolved QD data from a QD-stained cell specimen. (**c**) Deconvolved data showing the individual QD spectra. (**d**) Quantitative protein biomarker data as normalized by the internal reference (based on the area under each deconvolved QD spectrum). The images are raw data from a color CCD camera.

Step 3C
Additionally, the lack of staining or weak signal could be caused by a wrong hydrophobic barrier pen used or a wrong antigen retrieval method.

Unsuccessful QD–antibody conjugation
Aggregate formation: too many QDs present in buffer, too much of a reagent, e.g., EDC, wrong reaction buffer (e.g., buffer at an incorrect pH or using a free-amine containing buffer in EDC coupling reactions).
Presence of competitive proteins in the antibody solution.

Problems relating to QD staining of cell and clinical tissue specimens
No staining: unsuccessful conjugation, QDs disrupted during conjugation, antibody lost affinity during conjugation, concentration too low, incubation time too short, antigen retrieval not correct.
Too much staining: concentration too high, antigen retrieval condition too harsh.

ANTICIPATED RESULTS
Quantitative biomarker information can be obtained by using a spectrometer attached to the fluorescence microscope. It is however very important to use a common protein such as β-actin or GAPDH as an 'internal control'. That is, one of the QD–Ab conjugates should be designed to measure the product of a housekeeping gene that is expressed at relatively constant levels in all cells. As shown in **Figure 6**, this common protein can be used to normalize the biomarker data. The use of an internal control holds great promise for overcoming a number of major problems in biomarker quantification, such as differences in the probe brightness, variations in probe binding efficiency, uneven light illumination and detector responses (see **Box 2**).

The majority of available tumor specimens are archived, FFPE tissues that might be several decades old. As the clinical outcomes of these tissues are already known, these specimens are well suited for examining the relationship between molecular

---

BOX 2 | SIZE TUNABLE VS COMPOSITION TUNABLE QDS

Size-tunable properties are a hallmark of semiconductor QDs and related nanostructures. The fluorescence emission spectra of ZnS-capped CdSe QDs are tuned from blue to red by changing the core particle diameter from 1.5 to 6.0 nm. Such large size changes could, however, cause problems in many applications such as multicolor cellular imaging and immunohistochemical staining, because these particles have significantly different volumes, masses and surface areas. Moreover, size-tunable CdSe QDs show considerable variations in signal brightness (measured by the absorption coefficient and fluorescence quantum yield on a particle-to-particle basis) at different emission colors. In fact, the integrated signal intensity of green QDs (525 nm emission) is 17 times lower than that of red QDs (655 nm emission) and is almost 32 times lower than that of near-infrared dots (705 nm emission) under identical experimental conditions. It is thus not surprising that many QD users have observed that the red dots are considerably brighter than the green dots. When these dots are used to quantify biomarker expressions in the same cells or tissue specimens, the results will be misleading. To overcome this problem, recent research has shown that the QD emission spectrum can also be tuned by changing the composition of the core material while keeping the size constant[52–55]. In particular, alloyed semiconductor QDs (cadmium selenium telluride or CdSeTe) with both homogeneous and gradient internal structures have been prepared to achieve continuous tuning of the optical properties without changing the particle size[52]. Remarkably, the alloyed QDs exhibit similar fluorescence quantum yields (QE = 30–60%) and spectral widths (full-width at half-maximum or FWHM = 35 nm) as the traditional core-shell dots (FWHM = 30–35 nm). This type of QD is potentially advantageous for multiplexed cell/tissue labeling because their absorption coefficients (roughly proportional to the particle volume) are similar for all different colored dots. As a result, the brightness variability between dots with different emissions can be minimized, giving a more accurate representation of the actual profiles of biomarkers in cellular and tissue samples.
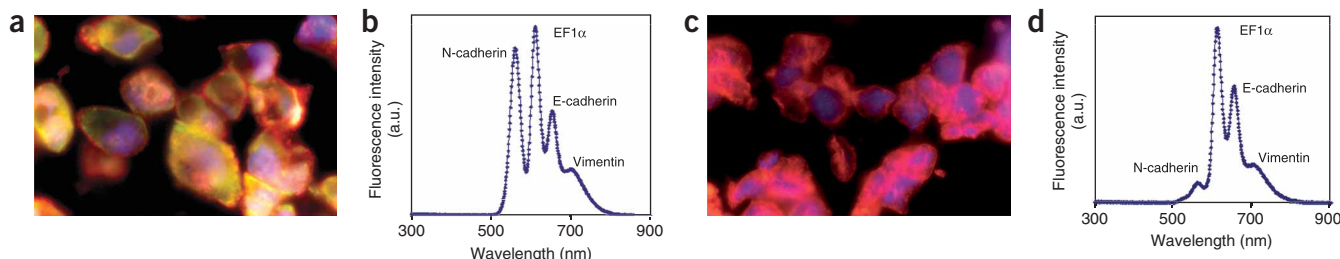
Figure 7 | Multiplexed QD profiling of four tumor biomarkers using two FFPE prostate cancer cell lines with distinct bone-metastasis behaviors. The four markers, all associated with EMT, are N-cadherin, EF (elongation factor)-1α, E-cadherin and vimentin, and their corresponding QD colors are 565, 605, 655 and 705 nm. The cell nuclei were counterstained blue by DAPI, and the QD data were captured under blue excitation. (**a**) Color fluorescence image of highly metastatic prostate cancer cells (clone ARCaPm); (**b**) single-cell QD data obtained from image **a**; (**c**) color fluorescence image of benign prostate cancer cells (clone ARCaPe); (**d**) single-cell QD data obtained from image **c**. The relative abundance of these markers is consistent with western blotting data (not shown). Note that individual cancer cells have heterogeneous expression patterns; the single-cell data in **b** and **d** are representative of a heterogeneous cell population. The images are raw data from a color CCD camera.

profile and clinical outcome in retrospective studies. One example is to study the epithelial–mesenchymal transition (EMT) process in the progression and metastasis of prostate cancer to the bone. EMT is a normal biological mechanism first reported in embryonic development and later found in cancer metastasis[37]. During EMT, cancer cells undergo phenotypic and behavioral changes and become more invasive, characterized by changes in the profiles of cellular adhesion molecules such as an increase of N-cadherin and a loss of E-cadherin. Other important markers for EMT include vimentin, cytokeratin 18 and RANKL. As a model system for staining optimization, we have used QD-conjugated secondary antibodies for molecular profiling of EMT using two FFPE slides from an androgen-repressed prostate cancer (ARCaP) model[38]. In this model, ARCaP$_E$ is more epithelial-like and less invasive, whereas the ARCaP$_M$ has more mesenchymal characteristics and is more invasive. The transition between ARCaP$_E$ and ARCaP$_M$ can be promoted by growth factors and by the interactions between prostate cancer cells and bone. Thus, this cell model represents a stepwise progression of human prostate cancer. As illustrated in **Figure 7**, we have achieved simultaneous staining of four different biomarkers with expression profiles consistent with western blot data. Moreover, QD staining provides spatial localization information (both inter- and intracellular), which is not possible with western blot or molecular biology techniques. A note of practical importance is that staining of FFPE cells requires longer incubation time (overnight at 4 °C versus 1 h at RT) and a higher QD–secondary antibody concentration than that required for freshly fixed cells.

For molecular profiling of clinical FFPE prostate specimens, we have also obtained interesting results by using four tumor antigens (mdm-2, p53, EGR-1 and p21), as shown in **Figure 8**. These markers are known to be important in prostate cancer diagnosis and are correlated with tumor behavior[39,40]. We are able to detect all four markers in the tissue specimens, but the autofluorescence is higher than that observed in FFPE cells. Compared with FFPE cells, clinical tissue specimens may require harsher antigen retrieval conditions (EDTA buffer vs citrate buffer) and generally have stronger autofluorescence. On the other hand, autofluorescence can be desirable by serving as a counterstain for tissue morphology. Autofluorescence can be separated from the QD signal by intentionally illuminating the sample to bleach it out while leaving the QDs bright enough for imaging and spectral analysis. Of course, spectral unmixing algorithms can be used to separate the background fluorescence from the real QD signals[41,42]. These early results demonstrate the feasibility of using QDs as fluorescent labels for molecular profiling of
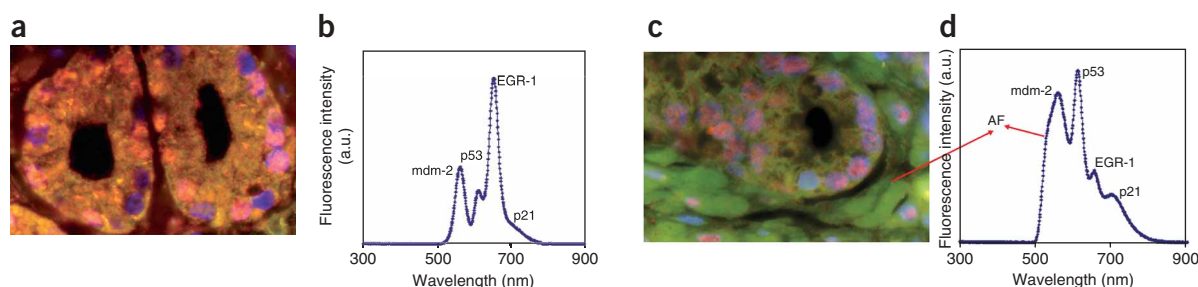

Figure 8 | Multiplexed QD staining of archived FFPE clinical specimen from human prostate cancer patients, and comparison between two different glands on the same tissue specimen. Four tumor biomarkers (mdm-2, p53, EGR-1 and p21) were labeled with four colors of QDs emitting at 565, 605, 655 and 705 nm, respectively. (**a**) Color fluorescence image of QD-stained tissue specimens showing just one gland; (**b**) representative fluorescence spectrum obtained from single cells in the gland (image **a**); (**c**) color fluorescence image of the same QD-stained tissue specimens but showing a different gland; (**d**) representative fluorescence spectrum obtained from single cells in the second gland (image **c**). Note that the biomarker profile is remarkably different for different glands. This ability to measure cellular heterogeneity on the same tumor specimen will be crucial for clinical applications. AF stands for autofluorescence. The images are raw data from a color CCD camera.

BOX 3 | NANOTYPING—THE USE OF MULTIPLEXED QD PROBES FOR CANCER MOLECULAR PROFILING

Significant opportunities exist at the interface between QD nanotechnology and signature biomarkers for cancer diagnosis and individualized therapy. In particular, QD nanoparticle probes can be used to quantify a panel of biomarkers on intact cancer cells and tissue specimens, allowing a correlation of traditional histopathology and molecular signatures for the same material[12–14]. A single nanoparticle is large enough for conjugation to multiple ligands, leading to enhanced binding affinity and exquisite specificity through a 'multivalency' effect. These features are especially important for the analysis of cancer biomarkers that are present at low concentrations or in small numbers of cells. Biomolecular markers are broadly defined as altered or mutant genes, RNA, proteins, lipids, carbohydrates, small metabolite molecules and altered expression of those that are correlated with a biological behavior or a clinical outcome. Most cancer biomarkers are discovered by molecular profiling studies, based on an association or correlation between a molecular signature and cancer behavior. In the cases of both breast and prostate cancer, a major progression step is the appearance of so-called 'lethal phenotypes' (causing patient death) such as bone metastatic, hormone independent, and radiation- and chemotherapy-resistant. It has been hypothesized that each of these aggressive behaviors or phenotypes could be understood and predicted by a defining set of biomarkers. By critically defining the interrelationships between these biomarkers, it could be possible to diagnose and determine the prognosis of a cancer based on a patient's molecular profile, leading to personalized and predictive medicine.

FFPE clinical specimens. With continuous efforts in optimizing the experimental conditions, we believe that QD probes hold great promise in multiplexed molecular profiling of clinical tissue specimens and correlation of biomarkers with disease behavior (see **Box 3**).

It is critically important to validate the QD staining data with other available techniques. For this purpose, we have obtained QD molecular profiling data from standard human breast cell specimens, and have compared the corresponding biomarker data with traditional IHC and fluorescence *in situ* hybridization techniques. Briefly, slides from formaldehyde-fixed paraffin cell blocks were stained in accordance with standard pathological protocols for three breast cancer biomarkers—ER (estrogen receptor), PR (prostesterone receptor) and HER2. This panel of protein biomarkers was selected because of its clinical significance in human breast cancer diagnosis and treatment[43–46]. The traditional IHC results were analyzed by two independent observers and scored with a standard scale from 0 (no visible staining in the nucleus or membrane) to 3+ (strong and complete membrane or nuclear staining in more than 10% of malignant stained cells). For a comparative analysis of QD profiling with traditional IHC, it is necessary to normalize the absolute fluorescence intensities of QD–Ab signals so that relative percentage values are calculated from the maximum signal strength.

The results reveal that a 3+ score for ER, PR or HER2 by traditional IHC corresponds to 85–100% relative expression of the antigen by QD–Ab measurement, and that 1+ or 2+ scores by traditional IHC correspond to 11–48% expression as determined by QD quantification. We note that classification of antigens expressed at low levels (1+ or 2+) is subjective, requiring experience and often resulting in considerable interobserver variations. In contrast, quantitative QD measurements allow accurate determination of tumor antigens at low levels. For example, PR expression in MCF-7 cells and ER expression in BT-474 cells are both classified as 1+ by traditional IHC, but quantitative QD measurements indicate major differences in PR expression (16.8%) and ER expression (47.7%) in these two cell lines. This indicates that the quantitative nature of QD-based molecular profiling could simplify and standardize categorization of antigens that are expressed at low levels. This is of fundamental importance in the management of breast cancer, as the likely benefit of hormonal therapies and trastuzumab depends directly on not just the presence but also the quantity of hormone or HER2 receptors[47–49].

1. Bruchez, M. Jr., Moronne, M., Gin, P., Weiss, S. & Alivisatos, A.P. Semiconductor nanocrystals as fluorescent biological labels. *Science* **281**, 2013–2015 (1998).
2. Chan, W.C.W. & Nie, S.M. Quantum dot bioconjugates for ultrasensitive nonisotopic detection. *Science* **281**, 2016–2018 (1998).
3. Alivisatos, P. The use of nanocrystals in biological detection. *Nat. Biotechnol.* **22**, 47–52 (2004).
4. Pinaud, F. *et al.* Advances in fluorescence imaging with quantum dot bio-probes. *Biomaterials* **27**, 1679–1687 (2006).
5. Michalet, X. *et al.* Quantum dots for live cells, *in vivo* imaging, and diagnostics. *Science* **307**, 538–544 (2005).
6. Gao, X.H., Cui, Y.Y., Levenson, R.M., Chung, L.W.K. & Nie, S.M. *In vivo* cancer targeting and imaging with semiconductor quantum dots. *Nat. Biotechnol.* **22**, 969–976 (2004).
7. Smith, A.M., Gao, X.H. & Nie, S.M. Quantum dot nanocrystals for *in vivo* molecular and cellular imaging. *Photochem. Photobiol.* **80**, 377–385 (2004).
8. Chan, W.C.W. *et al.* Luminescent quantum dots for multiplexed biological detection and imaging. *Curr. Opin. Biotechnol.* **13**, 40–46 (2002).

9. Klostranec, J.M. & Chan, W.C.W. Quantum dots in biological and biomedical research: recent progress and present challenges. *Adv. Mater.* **18**, 1953–1964 (2006).

10. Medintz, I.L., Tetsuo-Uyeda, H., Goldman, E.R. & Mattoussi, H. Quantum dot bioconjugates for imaging, labelling and sensing. *Nat. Mater.* **4**, 435–446 (2005).

11. Chattopadhyay, P.K. *et al.* Quantum dot semiconductor nanocrystals for immunophenotyping by polychromatic flow cytometry. *Nat. Med.* **12**, 972–977 (2006).

12. Yezhelyev, M. *et al.* Emerging use of nanoparticles in diagnosis and treatment of breast cancer. *Lancet Oncol.* **7**, 657–767 (2006).

13. Xing, Y., Smith, A.M., Agrawal, A., Ruan, G. & Nie, S.M. Profiling single cancer cells and clinical tissue specimens with semiconductor quantum dots. *Int. J. Nanomed.* **1**, 473–481 (2006).

14. Gao, X.H. *et al.* In-vivo molecular and cellular imaging with quantum dots. *Curr. Opin. Biotechnol.* **16**, 63–72 (2005).

15. Wu, X.Y. *et al.* Immunofluorescent labeling of cancer marker Her2 and other cellular targets with semiconductor quantum dots. *Nat. Biotechnol.* **21**, 41–46 (2003).

16. Matsuno, A. *et al.* Three-dimensional imaging of the intracellular localization of growth hormone and prolactin and their mRNA using nanocrystal (quantum dot) and confocal laser scanning microscopy techniques. *J. Histochem. Cytochem.* **53**, 833–838 (2005).

17. Giepmans, B.N.G. *et al.* Correlated light and electron microscopic imaging of multiple endogenous proteins using quantum dots. *Nat. Methods* **2**, 743–749 (2005).

18. Ness, J.M. *et al.* Combined tyramide signal amplification and quantum dots for sensitive and photostable immunofluorescence detection. *J. Histochem. Cytochem.* **51**, 981–987 (2003).

19. Nisman, R. *et al.* Application of quantum dots as probes for correlative fluorescence, conventional, and energy-filtered transmission electron microscopy. *J Histochem. Cytochem.* **52**, 13–18 (2004).

20. Tokumasu, F. & Dvorak, J. Development and application of quantum dots for immunocytochemistry of human erythrocytes. *J. Microsc. Oxford* **211**, 256–261 (2003).

21. Ghazani, A.A. *et al.* High throughput quantification of protein expression of cancer antigens in tissue microarray using quantum dot nanocrystals. *Nano Lett.* **6**, 2881–2886 (2006).

22. Taylor, C.R. & Levenson, R.M. Quantification of immunohistochemistry—issues concerning methods, utility and semiquantitative assessment II. *Histopathology* **49**, 411–424 (2006).

23. Guarner, J. & Zaki, S.R. Histopathology and immunohistochemistry in the diagnosis of bioterrorism agents. *J. Histochem. Cytochem.* **54**, 3–11 (2006).

24. So, M.-K., Loening, A.M., Gambhir, S.S. & Rao, J.H. Creating self-illuminating quantum dot conjugates. *Nat. Protoc.* **1**, 1160–1164 (2006).

25. Clapp, A.R., Goldman, E.R & Mattoussi, H. Capping of CdSe–ZnS quantum dots with DHLA and subsequent conjugation with proteins. *Nat. Protocols* **1**, 1258–1266 (2006).

26. Bannai, H. *et al.* Imaging the lateral diffusion of membrane molecules with quantum dots. *Nat. Protoc.* **1**, 2628–2634 (2007).

27. Goldman, E.R. *et al.* Conjugation of luminescent quantum dots with antibodies using an engineered adaptor protein to provide new reagents for fluoroimmunoassays. *Anal. Chem.* **74**, 841–847 (2002).

28. Paborsky, L.R., Dunn, K.E., Gibbs, C.S. & Dougherty, J.P. A nickel chelate microtiter plate assay for six histidine-containing proteins. *Anal. Biochem.* **234**, 60–65 (1996).

29. Jin, L. *et al.* Use of alpha-*N,N*-bis[carboxymethyl]lysine-modified peroxidase in immunoassays. *Anal. Biochem.* **229**, 54–60 (1995).

30. Shi, S.R., Cote, R.J. & Taylor, C.R. Antigen retrieval immunohistochemistry: past, present, and future. *J. Histochem. Cytochem.* **45**, 327–343 (1997).

31. Mortensen, E.N. & Barrett, W.A. Intelligent scissors for image composition. *Proceedings of the 22nd Annual Conference on Computer Graphics and Interactive Techniques* 191–198 (1995).

32. Hong, J.Y. & Wang, M.D. High speed processing of biomedical images using programmable GPU. *Proc. IEEE Int. Conf. Image Processing (ICIP), Singapore* 1133–1137 (2004).

33. Cormen, T.H., Leiserson, C.E., Rivest, R.L. & Stein, C. *Introduction to Algorithms* (MIT Press, Cambridge, MA, USA, 2001).

34. Weeks, A.R. & Hague, G.E. Color segmentation in the HSI color space using the K-means algorithm. *Proc. SPIE—Nonlinear Image Processing VIII* 143–154 (ACM Press, New York, USA, 1997).

35. Hermanson, G.T. *Bioconjugate Techniques* 475–478 (Academic, San Diego, CA, USA, 1996).

36. Hermanson, G.T. *Bioconjugate Techniques,* 123–124 (Academic, San Diego, CA, USA, 1996).

37. Huber, M.A., Kraut, N. & Beug, H. Molecular requirements for epithelial–mesenchymal transition during tumor progression. *Curr. Opin. Cell Biol.* **17**, 548–558 (2005).

38. Zhau, H.Y., Chang, S.M., Chen, B.Q., Wang, Y. & Zhang, H. Androgen-repressed phenotype in human prostate cancer. *Proc. Natl. Acad. Sci. USA* **93**, 15152–15157 (1996).

39. Hernandez, I. *et al.* Prostate-specific expression of p53 (R172L) differentially regulates p21, Bax, and mdm2 to inhibit prostate cancer progression and prolong survival. *Mol. Cancer Res.* **1**, 1036–1047 (2003).

40. Mora, G.R., Olivier, K.R., Mitchell, R.F., Jenkins, R.B. & Tindall, D.J. Regulation of expression of the early growth response gene-1 (EGR-1) in malignant and benign cells of the prostate. *Prostate* **63**, 198–207 (2005).

41. Mansfield, J.R., Gossage, K.W., Hoyt, C.C. & Levenson, R.M. Autofluorescence removal, multiplexing, and automated analysis methods for *in-vivo* fluorescence imaging. *J. Biomed. Opt.* **10**, 41207 (2005).

42. Levenson, R.M. Spectral imaging and pathology: seeing more. *Lab. Med.* **35**, 244–252 (2004).

43. Umemura, S. & Osamura, R.Y. Utility of immunohistochemistry in breast cancer practice. *Breast Cancer* **11**, 334–338 (2004).

44. Thomson, A. *et al.* HER-2/neu in breast cancer: interobserver variability and performance of immunohistochemistry with 4 antibodies compared with fluorescent in situ hybridization. *Mod. Pathol.* **14**, 1079–1086 (2001).

45. Vogel, C.L. *et al.* Efficacy and safety of trastuzumab as a single agent in first-line treatment of HER2-overexpressing metastatic breast cancer. *J. Clin. Oncol.* **20**, 719–726 (2002).

46. Elledge, R.M. *et al.* Estrogen receptor (ER) and progesterone receptor (PR), by ligand-binding assay compared with ER, PR and pS2, by immunohistochemistry in predicting response to tamoxifen in metastatic breast cancer: a Southwest Oncology Group Study. *Int. J. Cancer* **89**, 111–117 (2000).

47. Marquez, D.C. & Pietras, R.J. Membrane-associated binding sites for estrogen contribute to growth regulation of human breast cancer cells. *Oncogene* **20**, 5420–5430 (2001).

48. Hicks, D.G. & Tubbs, R.R. Assessment of the HER2 status in breast cancer by fluorescence *in situ* hybridization: a technical review with interpretive guidelines. *Hum. Pathol.* **36**, 250–261 (2005).

49. Konecny, G. *et al.* Quantitative association between HER-2/neu and steroid hormone receptors in hormone receptor-positive primary breast cancer. *J. Natl. Cancer Inst.* **95**, 142–153 (2003).

50. Matkowskyj, K.A., Schonfeld, D. & Benya, R.V. Quantitative immunohistochemistry by measuring cumulative signal strength using commercially available software Photoshop and Matlab. *J. Histochem. Cytochem.* **48**, 303–311 (2000).

51. Matkowskyj, K.A., Schonfeld, D. & Benya, R.V. Quantitative immunohistochemistry by measuring cumulative signal strength accurately measures receptor number. *J. Histochem. Cytochem.* **51**, 205–214 (2003).

52. Bailey, R.E. & Nie, S.M. Alloyed semiconductor QDs: tuning the optical properties without changing the particle size. *J. Am. Chem. Soc.* **125**, 7100–7106 (2003).

53. Jiang, W., Singhal, A., Zheng, J.N., Wang, C. & Chan, W.C.W. Optimizing the synthesis of red- to near-IR-emitting CdS-capped CdTexSe1-x alloyed quantum dots for biomedical imaging. *Chem. Mater.* **18**, 4845–4854 (2006).

54. Zhong, X.H., Han, M.Y., Dong, Z.L., White, T.J. & Knoll, W. Composition-tunable ZnxCd1-xSe nanocrystals with high luminescence and stability. *J. Am. Chem. Soc.* **125**, 8589–8594 (2003).

55. Zhong, X.H., Feng, Y.Y., Knoll, W. & Han, M.Y. Alloyed ZnxCd1-xS nanocrystals with highly narrow luminescence spectral width. *J. Am. Chem. Soc.* **125**, 13559–13563 (2003).